Use of Chitosan-Fe for Phosphorus Recovery and Promoted Methane Production from Anaerobic Digestion of Waste Activated Sludge

January 2021

Boaiqi ZHANG

Use of Chitosan-Fe for Phosphorus Recovery and Promoted Methane Production from Anaerobic Digestion of Waste Activated Sludge

A Dissertation Submitted to

the Graduate School of Life and Environmental Sciences,

the University of Tsukuba

in Partial Fulfillment of the Requirements

for the Degree of Doctor of Philosophy in Environmental Studies

(Doctoral Program in Sustainable Environmental Studies)

Boaiqi ZHANG

Abstract

The increasing generation amount of waste activated sludge (WAS) from wastewater treatment plants (WWTPs) is becoming a major problem for the sustainable management of WWTPs. Anaerobic digestion (AD) has been successfully applied for WAS treatment in WWTPs, owing to its capability of simultaneous bioenergy production and resources recovery. However, low methane yield and sludge reduction rate to some extent limit the application of AD in WAS treatment. Besides, the post treatment of liquid digestate containing high level of phosphate is also one of the main problems for AD systems, due to the massive phosphorus (P) released during AD process. Therefore, it is highly demanded to develop new methods for simultaneous P recovery and enhanced methane production from AD of WAS.

Previous studies indicate that conductive carbon-based materials or Fe (III) might improve AD of WAS through the direct interspecies electron transfer (DIET). Chitosan-Fe (III) complex (CTS-Fe) as an inexpensive and environmentally friendly carbon-based material possesses excellent P adsorption capacity and has been successfully employed to adsorb phosphate. Therefore, it is speculated that CTS-Fe has great potential for methane production and P recovery from AD of WAS. This study for the first time attempted to simultaneously recover P and enhance methane production from WAS with the supplementation of CTS-Fe.

This study attempted for the first time to simultaneously recover P and enhance methane production from WAS by adding CTS-Fe. The potential mechanisms of P removal/recovery and methane production improvement from WAS by CTS-Fe addition were also revealed. The results showed that:

(1) CTS-Fe had an excellent adsorption capacity in a wide pH range. The maximum phosphate adsorption capacity for CTS-Fe was estimated to be 15.7 mg-P/g. Under acidic conditions, the route of the adsorption process was the reaction between phosphate and functional groups by electrostatic attraction and iron hydrolysates by ligand exchange, respectively. Owing to the increase of challenging OH^- ions, the electrostatic attraction weakened and ligand exchange was the dominant mechanism for phosphate adsorption under alkaline conditions.

(2) CTS-Fe addition could significantly improve the AD of WAS. The cumulative methane yields at CTS-Fe dosage of 5.0, 10.0 and 20 g/L of were detected to be 209.9, 236.6 and 247.9 mL/g-VS, respectively, about 12% - 32% higher than the control (187.5 mL/g-VS). Moreover, the VS reductions in the CTS-Fe reactors were increased by about 1.04 - 1.22 times compared to the control (27.4%). Microbial community analysis confirmed that iron reducing bacteria

(IRB) and acetoclastic methanogens were enriched in the CTS-Fe added reactors, most probably due to that CTS-Fe facilitated dissimilatory iron reduction (DIR) and DIET during AD process.

(3) P fractionation results indicate that 2.4 times higher non-apatite inorganic phosphorus (NAIP) reduction occurred in the solid phase of sludge at 20 g/L of CTS-Fe (6.72 mg/g-SS) when compared to the control (no CTS-Fe addition, 2.77 mg/g-SS). 57.8 mg of P was efficiently recovered from the liquid and solid phases in CTS-Fe (20 g/L) added AD reactor. Notably, under the test conditions, P adsorption capacity of CST-Fe was about 36.15 - 91.43 mg/g at dosage of 5 - 20 g/L, much higher than its use for synthetic phosphate-containing wastewater treatment (15.70 mg/g, as mentioned above). This observation is mainly due to the more complex composition of the liquid digestate involving more pathways to remove P. Characterization analysis demonstrated that partial Fe (III) on the CTS-Fe was reduced and effectively combined with P to form vivianite crystals on the CTS-Fe surface during AD process, with the mechanisms for P recovery dominated by ligand exchange and chemical precipitation.

Results from this work are useful for P removal/recovery from wastewater and WAS with enhanced AD process, which will help to provide a new approach for simultaneous P removal/recovery and enhanced methane production from AD of WAS.

Keywords**:** Chitosan-Fe (III) complex; Waste activated sludge; Anaerobic digestion; Methane production; Phosphorus recovery; Mechanism

Contents

List of tables

List of figures

Chapter 1 Introduction

1.1 Production and disposal of waste activated sludge

Tremendous amounts of waste activated sludge (WAS) are generated in wastewater treatment plants (WWTPs) as a main byproduct every year, which is an arduous task for the solid waste management industry (Huang & Tang, 2015; Wang et al., 2018a). In Japan, around 166.94 million tons of WAS were generated in 2018, accounting for about 44.4% of the total industrial waste (MOE, 2020). According to some reports, due to the high operation cost (occupy about half of the total operating costs of a WWTP) and challenging technology of sludge treatment, only 35% of the WAS are well managed (Luo et al., 2018; Zhao et al., 2017a). In Japan the reutilization ratio of sewage sludge reached 75% (dry solid basis) in 2019, but only 34% were utilized as biomass (energy 24% and land application 10%) (MLIT, 2019). Inappropriate disposal of WAS may bring about secondary pollution problems like greenhouse gases (GHGs) emission and groundwater pollution (Giusti, 2009). Conventionally, Incineration, landfill and reutilization as soil conditioner are the main disposal methods for WAS. With the recent stringent solid waste disposal criteria, much more sludge is now beneficially reused, both in agriculture and via a variety of thermal technologies (Tyagi & Lo, 2013).

1.2 Significance of P resource and energy recovery from waste activated sludge

WAS with a huge production volume contains high levels of nutrients in addition to high water content. WAS is consisted 59% - 88% (w/v) of organic matter, about 50% - 55% carbon, 25% - 30% oxygen, 10% - 15% nitrogen, 6% - 10% hydrogen, 1% - 3% phosphorus and 0.5% - 1.5% sulfur contained (Orhon & Artan, 1994). The ash from waste sludge contains mainly minerals and some heavy metals (Fonts et al., 2009). The two components in WAS that are technically and economically feasible to recycle are nutrients (primarily phosphorus) and energy (carbon) (Campbell, 2000).

1.2.1 P resource

Phosphorus (P) is an essential element for the metabolism of all living organisms, which occurs naturally in a variety of chemical forms. However, as a limited and non-renewable resource, P is predicted to be exhausted in the next century (Cordell et al., 2009). The efficient P recovery is thereby extremely urgent and significant. It has been reported that around 4% - 12% P can be concentrated in WAS when enhanced biological phosphorus removal (EBPR) and chemical phosphorus removal (CPR) techniques are applied in WWTPs (He et al., 2016; Xu et al., 2015). Thus, WAS has been increasingly recognized as a potential and promising source for P recovery.

1.2.2 Energy

Biogas produced during the anaerobic digestion (AD) of the WAS contains 60% - 70% methane, 30% - 40% carbon dioxide, and trace amounts of nitrogen, hydrogen and hydrogen sulfide (Tyagi & Lo, 2013). Methane is the main resource for energy recovery in WAS, as well as the primary energy source for WWTPs. Usually, the recovered methane is used to drive the gas engine, generate electricity and thermal energy for the treatment plant, which can reduce the production of carbon dioxide related to the energy (fossil fuels) used in WWTPs. Moreover, the electricity cost of the WWTP accounts for about 80% of the total operating cost, and the energy recovered through methane can make up for half of this cost (Deublein & Steinhauser, 2011). Therefore, WAS is an ideal source for renewable energy recovery.

1.3 Techniques and limitations for P resource and energy recovery

1.3.1 Energy recovery

There are several techniques available for energy recovery from sludge, such as AD, incineration, gasification, pyrolysis, supercritical water oxidation. Table 1-1 shows some information about these technologies, including cost, environmental benefits, improvement requirement, development stage and comments on each technology (Rulkens & Bien, 2004). AD has been successfully applied at full scale as the most attractive method for WAS treatment, due to its capacity for simultaneous bioenergy production and resources recovery (volatile fatty acids (VFAs) or methane) (Cao et al., 2019; Li et al., 2018).

Although AD has been deemed to be an efficient and promising method to dispose WAS, it is still limited for practical applications by the long retention time, low biodegradation efficiency, and low biogas production rate. AD is generally proceeded in the following sequential three steps, namely hydrolysis, acidogenesis and methanogenesis. Among the above three steps, hydrolysis is regarded as the rate-limiting step of AD of WAS because microbial cell walls in sludge are resistant to decompose (Peng et al., 2018). Moreover, the slow electron exchange rate among anaerobes might be the main reason for the low efficiency of methanogenesis stage during AD (Yang et al., 2017). To solve the above problems, various studies have found that additional materials had great potentials in enhancing methane production efficiently and economically during AD process. Previous studies indicated that carbon-based materials, such as graphene, granular activated carbon (GAC), biochar (BC), carbon cloth (CC), can serve as an electron donor to stimulate direct interspecies electron transfer (DIET) in different substrates during AD process (Lin et al., 2017a; Yang et al., 2017; Wang et al., 2018b; Zhao et al., 2017c). Moreover, various studies have shown that adding iron also promoted methane production from AD system by enhancing degradation of substrate and

DIET (Zhang et al., 2014; Zhao et al., 2018b; Peng et al., 2018). An overview of additional materials enhanced methane production in AD system is summarized in Table 1-2.

On the other hand, the AD process can result in a large amount of phosphate release into the liquid digestate (Cheng et al., 2017) which should be paid much attention when taking the efficient subsequent treatment and resources recovery into consideration. That is, additional treatment process for the liquid digestate is required before being processed, which is also one of the major issues for the sustainable management of AD systems.

1.3.2 P resource recovery

P resource recovery from WAS is usually carried out in the liquid digestate. Several methods have been developed for P recovery, including EBPR (Wong et al., 2013), membrane separation technology (Blöcher et al., 2012), ion exchange (Bottini & Rizzo, 2012), source separation technology (Kemacheevakul et al., 2011), crystallization (Rahaman et al., 2014) and adsorption (Kizito et al., 2017). Notably, these technologies mainly use different processes to dissolve and concentrate P to obtain a P-rich supernatant, and the final recovery method is mainly crystallization.

Up to now, a lot of research efforts have been focused on the P recovery from WAS by crystallization (see Table 1-3). Through coupling hydrothermal pretreatment with crystallization of magnesium ammonium phosphate (MAP, or struvite), Rahaman et al. (2014) simulated the removal and recovery of P from the liquid digestate via struvite crystallization in a fluidized bed reactor. On the other hand, recently P recovery from WAS as vivianite has gained more attention due to its higher P recovery efficiency and economic value (Wilfert et al., 2018; Wu et al., 2019). For instance, (Cao et al., 2019) obtained about 82.60% of total P (TP) recovered as vivianite during AD of WAS under optimal $FeCl_3$ dosage and pH condition. Although these techniques are valid, they have limited practical applications mainly owing to the following disadvantages: (1) complex operating conditions; (2) low P recovery efficiency from liquid digestate while with high residual P in the solid sludge; (3) high operating costs due to chemical reagents addition; and (4) difficulty in direct separation and purification of phosphate precipitate from the treated WAS (Egle et al., 2016; Hao et al., 2013; Li et al., 2019a; Wang et al., 2019; Wilfert et al., 2018; Wu et al., 2019).

Consequently, it is highly demanded to develop more efficient and environment-friendly methods for simultaneous P recovery with enhanced methane production is of vast significance for AD of WAS.

1.4 Chitosan-Fe as a novel adsorbent for P recovery/removal in wastewater treatment

Chitosan, a product of chitin N-deacetylation, is a typical nitrogen-containing basic polysaccharide in nature, which has usually been used to remove cation and anion species (Zhang et al., 2015). The previous studies pointed out that chitosan had the ability to coordinate with many transition metal ions through a chelation mechanism due to the liberal modifiable functional groups (–OH and $–NH_2$) on the surface of chitosan (Fagundes et al., 2001). Consequently, removing phosphate by single metal or multi-metal oxides loading chitosan adsorbents have been increasingly reported, such as chitosan-stabilized nano Zero-valent Iron (CS-nZVI) (Xie et al., 2016), chitosan/Al_2O_3/Fe_3O_4 composite nanofibrous (Bozorgpour et al., 2016), Zr^{4+}- CSBent, Fe^{3+}- CSBent and Ca^{2+}- CSBent biocomposite (Kumar & Viswanathan, 2017). Among these synthetic adsorbents, because of the strong buffering ability of trivalent iron, Fe loading was the most widely used method for modification. It has been previously demonstrated that the adsorption of phosphate on chitosan-Fe (III)-crosslinked in an experiment of solid-phase extraction was high efficiently (Fagundes et al., 2001), and phosphate adsorption capacity of iron (III) chitosan complex was much higher than iron (II) chitosan complex (Jing & Yamaguchi, 2006).

1.5 Why does Chitosan-Fe offer as a resource recovery approach from WAS?

As an environmentally friendly carbon based material, granular chitosan-Fe (III) complex (CTS-Fe) with excellent P adsorption capacity has been successfully developed and employed to adsorb phosphate. Notably, previous studies have found that Fe (III) could be reduced as Fe (II) by dissimilatory metal-reducing bacteria (DMRB) under anaerobic condition (O'Loughlin et al., 2013; Rothe et al., 2016), which may further combine with phosphate to form vivianite. Thus, Fe on the surface of the CTS-Fe composite may have the ability to improve P recovery from AD of WAS. Furthermore, results from previous studies indicate that conductive carbon based materials or Fe (III) can accelerate DIET and enhance hydrolysis during AD of WAS, resulting in improved methane production (Hao et al., 2017; Peng et al., 2018; Yang et al., 2017; Zhao et al., 2018b). Therefore, it is speculated that CTS-Fe has great potential for recovering nutrients and energy from WAS.

1.6 Research objectives and thesis structure

As mentioned above, P is a non-renewable resource with limited reserves, and its rapid consumption accelerates the exhaustion of P in nature (Pastor et al., 2010). Therefore, to achieve the sustainable development of P resources, P recovery is of great significance. WAS produced from WWTPs is considered as a potential and promising source for P recovery. Moreover, AD is a most attractive sustainable technology for energy and nutrients recovery from WAS, due to its low-cost, mature and stable. Although gaining growing attention, AD has some limitations in practical applications, for example, low methane yield and sludge reduction rate. Besides, the extra treatment for P rich digestate is also one of the main problems in the sustainable management of AD. The major objective of this study was to investigate the effect of CTS-Fe composites on methane production and P recovery from WAS during AD.

The structure of the thesis is demonstrated by the experimental framework as in Figure 1-1. The contents of this thesis are divided into the following three parts.

Chapter 2 focused on the differences between the structure of raw and crosslinked CTS-Fe composites, and the mechanism of P adsorption from aqueous solutions at different pH conditions.

Chapter 3 attempted to simultaneously promote AD of WAS and recover P by CTS-Fe supplementation. Firstly, the feasibility of CTS-Fe for P recovery as vivianite from WAS via AD was identified by XRD and SEM-EDS analysis. Secondly, the fractionation and distribution of P species during AD of WAS in the presence of CTS-Fe were revealed. Finally, the effect of CTS-Fe on methane production from WAS was evaluated.

Chapter 4 investigated the potential mechanisms involved in the improvement of AD process by CTS-Fe supplementation and systematically explore any synergistic mechanisms.

Table 1-1 Techniques for energy recovery (Rulkens & Bien, 2004).

Techniques	Operation cost	Environmental benefits	Advancement requirement	Development stage	Comments
Anaerobic digestion	Low/ moderate	Energy (biogas) generation, resources recovery	Sludge pre-hydrolysis required to enhance biogas generation	Successfully applied at full scale	Release of phosphate and ammonia during digestion process
Incineration	High	Energy generation, minimization of biosolids quantity	Mechanical dewatering, drying, use of waste heat	Full scale	Phosphate can be recovered from ash
Pyrolysis and gasification	High	Valuable products recovery, minimization of biosolids quantity	Mechanical dewatering, drying, use of waste heat	In development stage	Complex process, marketing of products needs attention
Supercritical water oxidation	High	Energy generation, minimization of biosolids quantity	Reactor concept, process performance	In development stage	Complex process, Corrosion and scaling problems of the reactors walls

Table 1-2 Techniques for additional materials enhanced methane production in AD system.

Materials (Loading/SSA)	**Inoculum/Substrates**	**Temp. (°C)**	**Mode**	**Increase in CH_4 yield/production rate (%)**	**Reference**
Graphene (0.5-2 g/L)	Anaerobic sludge/Ethanol	35	Batch	20[b]	Lin et al. (2017)
GAC (0.5-5 g/L)	Anaerobic sludge/WAS	37	Batch	17.4[a]	Yang et al. (2017)
Biochar (15 g/L)	Anaerobic sludge/Food waste & sewage sludge	35	Batch	40.3[b]	Wang et al. (2018b)
Carbon cloth (500 cm^2/L)	Anaerobic sludge/Butanol	37	Semi-Continuous	59[b]	Zhao et al. (2017c)
Rusty scrap iron (10 g/L)	Anaerobic sludge/WAS	35	Batch	29.5[a]	Zhang et al. (2014)
ZVI (10 g/L)	Anaerobic sludge/WAS	37	Batch	21.3[a]	Zhao et al. (2018b)
Magnetite (27 g/L)	Anaerobic sludge/WAS	37	Batch	7.3[a]	Peng et al. (2018)

[a] CH_4 yield

[b] CH_4 production rate

Table 1-3 Status of research on P recovery from sludge by crystallization.

Metal sources	**Source of P**	**pH**	**Crystal products**	**P recovery rate (%)**	**Reference**
$MgCl_2$	Chemically enhanced primary sedimentation (CEPS) sludge	11	MAP	90	Chen et al. (2019)
$MgCl_2$	Excess sewage sludge	9	MAP	91.6	Yu et al. (2017)
$MgCl_2$	WAS	10	Struvite	98	Li et al. (2019b)
Ferrihydrite-Fe (III)	WAS	7.5	Not observed	53	Cheng et al. (2015)
Fe (II)/Fe (III)	Excess sewage sludge	7.5	Vivianite	70-90	Wilfert et al. (2018)
$FeCl_3$	WAS	7	Vivianite	82.6	Cao et al. (2019)
$FeCl_3$	CEPS sludge	8	Vivianite	23-31	Lin et al. (2017b)

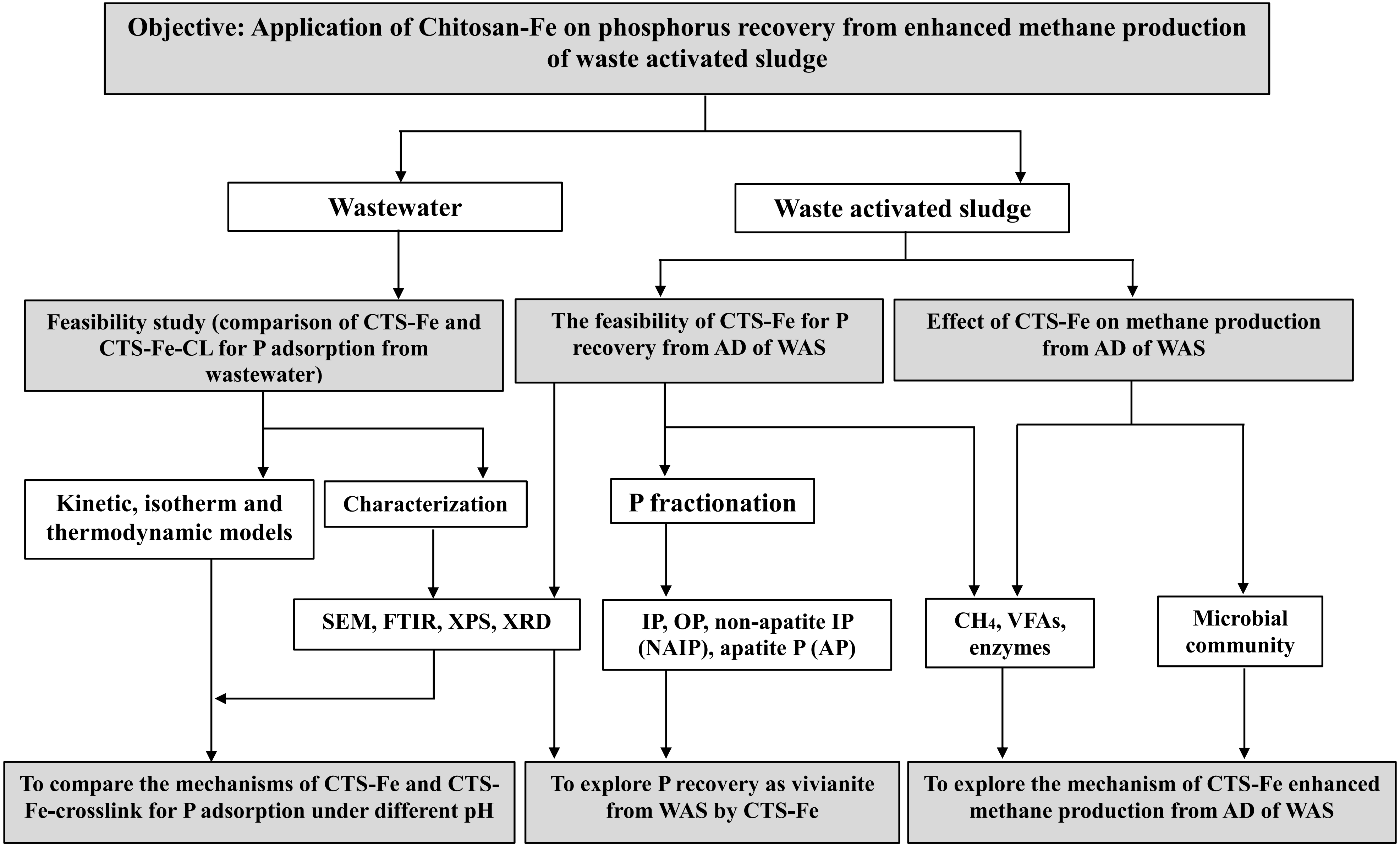

Fig. 1-1 The structure of this study.

Chapter 2 Phosphate adsorption by crosslinked/ non-crosslinked-Chitosan-Fe (III) complex sorbents: characteristic and mechanism

2.1 Introduction

Adsorption is considered to be the most attractive method for phosphate recovery due to its ease of operation, flexibility of design and cost efficiency (Shen et al., 2011). To date, a lot of natural minerals and organic polymers have been evaluated to be adsorbents for removing phosphate from water, including activated carbon (Liu et al., 2010), zeolite (Hamdi & Srasra, 2012), iron-based compounds (Tofik et al., 2016), PVA (Hui et al., 2014), Chitosan (Liu & Zhang, 2015). Among them, chitosan has been widely concerned in removing pollutants from wastewater because of its excellent properties such as rich source, nontoxic, environmental protection and biocompatibility. However, chitosan dissolves in wastewater at a low pH and loses its absorptive capacity because of its relatively weak base (pKa~6.2) (Kumar & Viswanathan, 2017). To overcome this shortcoming, many studies have been focused on the modification process to improve the stability of chitosan such as surface protonation (Filipkowska et al., 2014), mixed metal oxides (Shen et al., 2011) and polymer combinations (Rajeswari et al., 2015). Due to the abundant amino and hydroxyl functional groups, chitosan can be modified extensively by the cross-linking process to form variable morphology materials. The surface area and pore structure of chitosan were changed due to the insertion of new functional groups on chitosan after cross-linking process, which exhibited a higher performance on adsorption capacity (Mahaninia & Wilson, 2015). It has been previously demonstrated that chitosan-Fe and crosslinked chitosan-Fe complex (CTS-Fe-CL) have been successfully used to phosphate adsorption from aqueous solutions. However, the information on the mechanism of phosphate adsorption by Fe modified chitosan composite was limited.

In this chapter, the physico-chemical characterization on CTS-Fe/ CTS-Fe-CL composites were explored during the adsorption process. Specifically, this study aims to investigate the changes in functional groups on the adsorbent surface and the differences between the structure of raw and crosslinked CTS-Fe composites. Moreover, the mechanism of phosphate transportation at different pH conditions and the role of Fe in the process of phosphate adsorption were revealed in this study.

2.2 Materials and methods

2.2.1 Materials

Chitosan with a degree of deacetylation of 80.0% to 95.0% was purchased from Sinopharm Chemical Reagent Co., Ltd, Shanghai, China. $FeCl_3 \cdot 6H_2O$ was obtained from Tianjin Fuchen

Chemical Regents factory, Tianjin, China. All chemical reagents used in this study were of analytical grade, which were purchased from Sinopharm Chemical Reagent Co., Ltd, Shanghai, China. Moreover, all stock solutions were prepared with distilled water. A stock solution of phosphate (50 mg L^{-1}) was prepared by adding KH_2PO_4 (0.2197 g, dried at 373 K for 2 h) to a volumetric flask (1L), and then diluted with deionized water.

2.2.2 Synthesis of CTS-Fe and CTS-Fe-CL composites

Chitosan powder (16 g) was dissolved in 800 mL of 2% (v/v) acetic acid solution, stirred for 1 h at room temperature. Then, $FeCl_3 \cdot 6H_2O$ (0.05 M) was addedto the obtained transparent viscous solution. It was kept stirring for another 3 h to ensure that the chitosan was mixed entirely with ferric iron. The mixed solution was added dropwise into the ammonia solution (12.5% v/v) using a syringe. After stabilization for1 h, the wet beads were fully washed with deionized water to obtain a neutral pH value. Then the wet beads were divided into two equal parts, one part of them was preparation to the CTS-Fe composite, which dried at 323 K for 8 h. Another part of wet beadswas crosslinked with 15% glutaraldehyde solution for 24 h. After that, the crosslinked beads were thoroughly washed to remove residual crosslinking agents on the surface. The obtained granular chitosan-Fe (III) composites were stored in acentrifuge tube for batch study.

2.2.3 Batch experiments

To investigate the phosphate adsorption performance on the CTS-Fe and CTS-Fe-CL composites, batch studies were conducted by mixing 1 g dry adsorbent with 100 mL of phosphate solution (50 mg L^{-1}) in 250 mL conical flasks. The conical flasks were placed in a thermostatic shaker (HZC-280, Bing, China) and shaken at 150 rpm and 303 K for 48 h.To investigate the effect of pH, the initial pH was adjusted in the range from 3 to 12 using 0.1 M HCl or NaOH solution, and the pH was measured after 48 h at equilibration time. Furthermore, the effects of coexisting anions (HCO_3^-, NO_3^-, SO_4^{2-} and Cl^-) with the concentration of 50 and 200 mg L^{-1} were conducted at an initial phosphate concentration of 50 mg L^{-1}. All aqueous samples were filtered through cellulose filter before analysis.

2.2.4 Kinetic, isotherm and thermodynamic studies

The studies of kinetic, isotherm and thermodynamic were carried out at an adsorbent dosage of 10 g L^{-1}. For the kinetic study, phosphate solutions were shaken with an adsorbent at 303 K and 150 rpm for predetermined intervals of time (1, 2, 4, 8, 12, 16, 24, 36 and 48 h). Isotherm studies were performed at different initial phosphate concentration (10, 20, 50, 100, 150 and 200 mg L^{-1}) at different temperatures for 48 h. For the thermodynamic study, batch experiments were conducted at an initial phosphate concentration of 100 mg L^{-1} under different temperatures (293, 303 and 313 K).

2.2.5 Analytical models

(1) Kinetic equations

The potential rate-controlling steps of adsorption was investigated by the pseudo-first-order and pseudo-second-order models, which were given as Eqs. (2-1)-(2-2) (Ding et al., 2013):

$$q_t = q_e\left[1 - exp\left(-k_1 t\right)\right] \tag{2-1}$$

$$q_t = \frac{q_e{}^2 k_2 t}{1 + q_e k_2 t} \tag{2-2}$$

where q_t and q_e represent the adsorbed amounts of phosphate at a given time and equilibrium time, respectively (mg g^{-1}); k_1 (h^{-1}) and k_2 (g mg^{-1} h^{-1}) represent the rate constants for the pseudo-first-order and pseudo-second-order models; t (h) is the contact time.

The Elovich model is one of the most useful models for describing chemical adsorption process, which is given by (Wu et al., 2009)

$$\left(\frac{dq_t}{dt}\right) = \alpha\, exp\left(-\beta q_t\right) \tag{2-3}$$

where α is regarded as the initial rate (mg g^{-1} h^{-1}) since d_q / d_t = α as $q_t = 0$; the β is adsorption constant (g mg^{-1}). Eq. (2-3) was usually presented in the integrated form of the equation. Given that $q_t = 0$ at t = 0, the integrated form of Eq. (2-4) (Manap et al., 2018) is:

$$q_t = \left(\frac{1}{\beta}\right) ln\left(1 + \alpha\beta t\right) \tag{2-4}$$

The rate of Elovich equation depended on equilibrium factor of the Elovich equation (R_e), which was defined as (Wu et al., 2009):

$$R_e = 1/\left(q_{ref}\beta\right) \tag{2-5}$$

where the q_{ref} (mg g^{-1}) is the amount of adsorption at the longest operating time in the adsorption process.

The model of intra-particle diffusion can reveal the rate controlling steps, which is expressed by the Weber-Morris model (Weber & Morris, 1964):

$$q_t = k_{id} t^{1/2} \tag{2-6}$$

where the k_{id} is intra-particular diffusion rate constant (mg g^{-1} h$^{-1/2}$); i represents the stage of the adsorption process.

(2) Isotherm equations

The Langmuir and Freundlich isotherm models can provide valuable information to understand the phosphate adsorption mechanism. Their non-linear form of equations can be expressed as follows (Demarchi et al., 2013; dos Santos et al., 2011):

$$q_e = \frac{q_m K_L C_e}{1 + K_L C_e} \tag{2-7}$$

$$q_e = K_F C_e^{1/n} \tag{2-8}$$

where q_e and q_m (mg g^{-1}) represent the equilibrium phosphate concentration on the adsorbent and its maximal adsorption capacity, respectively; C_e (mg L^{-1}) is the equilibrium phosphate concentration; K_L (L mg^{-1}) and K_F (mg g^{-1}) are the constants of Langmuir and Freundlich, respectively; n is an empirical parameter related to adsorption intensity, and it changes with the heterogeneity of the material. In addition, the prime characteristic of the Langmuir isotherm is expressed by a dimensionless constant separation factor (R_L) as follows (Chatterjee & Woo, 2009):

$$R_L = \frac{1}{1 + K_L C_0} \tag{2-9}$$

where C_0 (mg L^{-1}) is the initial concentration of phosphate.

(3) Thermodynamic equations

The Gibbs free energy $\Delta G°$ (kJ mol^{-1}) is given as follow (Deng et al., 2016):

$$\Delta G^{\circ} = -RT\, ln\, K_c \tag{2-10}$$

where R (8.314 J mol^{-1} K^{-1}) is the constant of gas, T (K) is the absolute temperature, K_c (mL g^{-1}) is the constant of thermodynamic equilibrium which is defined as follow (Jain et al., 2010):

$$K_c = \frac{q_e}{C_e} \tag{2-11}$$

where q_e (mg g^{-1}) and C_e (mg L^{-1}) are the adsorption capacity of adsorbent and equilibrium concentration in solution, respectively; The variations of $\Delta S°$ (J mol^{-1} K^{-1}) and $\Delta H°$ (kJ mol^{-1}) during the reaction were expressed by the Van't Hoff equation, which is shown as follow (Deng et al., 2016):

$$ln\, K_c = \frac{\Delta S^{\circ}}{R} - \frac{\Delta H^{\circ}}{RT} \tag{2-12}$$

where the value of $\Delta H°$ and $\Delta S°$ are calculated by the slope and interceptofthe plots of lnK_c versus 1/T.

2.2.6 Analytical and characterization methods

The concentration of phosphate was measured by molybdenum blue method using an ultraviolet-visible spectrophotometer (DR 6000, HACH, USA). The characterization of adsorbents before and after adsorption, including surface morphology, pore size, crystal structure and micro-hardness was analyzed by using the scanning electron microscope (Nanta et al.)(SSX–550, Shimadzu, Japan), Brunauer-Emmett-Teller (BET) (JW-BK132F, JWGB, China), X-ray diffraction (XRD) (D8 Focus, Bruker, Germany) and Vickers Hardness (HV) (HMV-1T, China), respectively. Functional groups and electron binding energies of adsorbents were determined by using a Fourier transform infrared spectrometer (FTIR) (Vertex 70V, Bruker, Germany) and X-ray photoelectron spectroscopy (XPS) (ESCALAB250Xi, Thermo Fisher, USA).

2.3 Results and discussion

2.3.1 Characterization

The SEM images of chitosan-Fe (III)-crosslinked/non-crosslinked complex before and after phosphate adsorption were illustrated in Figs. 2-1(a-h). It was obvious that the non-crosslinked complex had tightly inhomogeneous folds in surface and tight core with extremely few pores. By contrast, the structure of crosslinked chitosan-Fe particles can be divided into three layers: brain striatum surface, mesoporous transitional layer, and the honeycomb inner core. The pleated surfaces on both adsorbents could be attributed to the uneven volatilization of ammonia and water molecule on the chitosan-Fe (III) complex hydrogel beads surface during desiccation. While the structural difference between the two adsorbents depended on the rate of evaporation of water molecules inside the particle. Furthermore, different degrees of damage could be observed on the surface of CTS-Fe after phosphate adsorption, and some amorphous colloids appeared on the surface and inside the adsorbent (Fig. 2-1e and g). As for CTS-Fe-CL, there was no significant damage on the surface, while the amorphous colloids appeared in the adsorbent surface and inside the pore walls (Fig. 2-1f and h). The difference of SEM images showed that the two adsorbents (CTS-Fe and CTS-Fe-CL) may have different adsorption mechanism, which might be related to the variance of the structures, surface morphologies and functional groups. BET parameters further revealed the pore structure of the two adsorbents (Table 2-1). The BJH surface area, total pore volume and the mean pore size of CTS-Fe were 1.18 m^2 g^{-1}, 0.01 cm^3 g^{-1} and 6.62 nm respectively, while the CTS-Fe-CL beads (85.66 m^2 g^{-1}, 0.34 cm^3 g^{-1} and 14.69 nm) were significantly higher than those of raw chitosan-Fe. It was suggested that CTS-Fe-CL had better pore development than the CTS-Fe. According to the International Union of Pure and Applied Chemistry (IUPAC), both the adsorbents exhibited the properties of mesoporous structures (2-50 nm) (Lyu et al., 2017).

However, the crystalline peak of the two adsorbents before and after adsorption was not observed by XRD analysis. It probably suggested that the iron was coordinated with various functional groups on chitosan, inhibiting the formation of crystalline iron (III) oxides (Hu et al., 2015; Liu et al., 2010).

2.3.2 Vickers hardness

Considering the significance of the engineering application, the hardness of the two adsorbents was detected using a micro Vickers hardness. The data of Vickers hardness were investigated by a Gaussian distribution (Fig. 2-2). The value of Vickers hardness was measured by the function of the actual contact area S between the indenter and the material (Ben Ghorbal et al., 2017; Schneider et al., 1999):

$$HV = \frac{P}{S} = \frac{2P\sin\theta}{d^2} = 1.8544\frac{P}{d^2} \tag{2-13}$$

where P (k_gf) is the applied load and S (mm^2) represents the indentation area; d (mm) is the average size of the measured diagonals of the indentation impression; θ is the semi-apex angle of the indenter equal to 68°.

As shown in Fig. 2-2, the probability distribution function (PDF) of the Vickers hardness of the CTS-Fe ($R^2 = 0.998$) and CTS-Fe-CL ($R^2 = 0.920$) was in accordance with the Gaussian distribution, and the average of HV in CTS-Fe and CTS-Fe-CL were 38.82 and 15.98 $k_gf\ mm^{-2}$, respectively. These results suggested that CTS-Fe had better durability and mechanical hardness than CTS-Fe-CL.

2.3.3 Effect of pH

The process of phosphate adsorption was critically dependent upon pH value because the dissociation equilibrium of phosphate was highly controlled by the pH value. Phosphate can exist in different species in solution, such as monovalent $H_2PO_4^-$ (pK > 2.16), divalent HPO_4^{2-} (7.20 < pK < 12.35), and trivalent PO_4^{3-} ions (pK > 12.35) (Chitrakar et al., 2006). As shown in Fig. 2-3, the high adsorption capacity was obtained at acidic conditions (pH from 3.0 to 7.0) for both of the two adsorbents. The equilibrium pH (pH_f) was higher than the initial pH (pH_i), which could be attributed to the decreased H^+ by protonation of the free amine groups in chitosan, and increased OH^- by ligand exchange between phosphate ions and groups of Fe–OH on sorbents. By contrast, the adsorption capacity of CTS-Fe decreased slowly from 4.39 to 3.29 mg-P g^{-1} and CTS-Fe-CL decreased sharply from 3.98 to 1.16 mg-P g^{-1} in the pH range of 7.0 to 12.0. The challenging OH^- ions occupied the adsorption sites and changed the surface charge on the adsorbent surface, which was the reason for the significant reduction of the adsorption capacity and the value of equilibrium pH at alkaline conditions (Dantas et al., 2001; Liu et al., 2008). Moreover, Fe (III) played a crucial role in the process of adsorption because it might affect the pH change in the solutions. A large quantities of hydrogen ions produced by the Fe (III) hydrolysis reaction could enhance the protonation process at acidic condition. The process of hydrolysis reaction can be expressed as follows (Liu et al., 2016):

$$Fe^{3+} + H_2O \rightarrow FeOH^{2+} + H^+ \quad (2\text{-}14)$$

$$FeOH^{2+} + H_2O \rightarrow Fe(OH)_2^+ + H^+ \quad (2\text{-}15)$$

$$Fe(OH)_2^+ + H_2O \rightarrow Fe(OH)_3 + H^+ \quad (2\text{-}16)$$

Meanwhile, there were previous reports indicated that the monovalent $H_2PO_4^-$ was more easily combined with metal (hydr) oxide surfaces than other ionic species (Fagundes et al., 2001; Lai et al., 2016; Tofik et al., 2016). This results revealed low pH was beneficial for the phosphate adsorption on the chitosan-Fe complex. Moreover, the surface of cross-linked chitosan microbeads with different kinds of medicaments improved the chemical stability and mechanical resistance of chitosan in a wide pH range (Mahaninia & Wilson, 2017). However, the present study indicated that raw uncross linked Fe-modified chitosan had a better phosphate adsorption capacity than that of crosslinking in a wide pH range, suggesting the uncross-linked CTS-Fe complex was more practical.

2.3.4 Effect of coexisting ions

The coexisting anions species might exert a negative influence on adsorption process, which could eventually deteriorate the efficiencyforphosphate adsorption. Therefore, to evaluate the selectivity of CTS-Fe and CTS-Fe-CL complex for phosphate removal, several anions including SO_4^{2-}, NO_3^-, HCO_3^- and Cl^- were investigated on phosphate adsorption. As shown in Fig. 2-4, all the coexisting anions could affect phosphate adsorption for both of the adsorbents. It is possible that coexisting anions occupied adsorption sites and increased electrostatic repulsion between adsorbent and phosphate. Moreover, the previous study reported that multivalent anions were adsorbed more easily than monovalent anions (Wan et al., 2012), while the negative influence of bicarbonate for phosphate removal was the most significant in the present study. The increase in the concentration of hydroxyl ions in the solution led to a decrease in the capacity of adsorption phosphate since the bicarbonate-containing solution was weakly alkaline. This result further indicated the process of phosphate adsorption was unfavorable under alkaline conditions. In addition, the experiment evaluated the performance of Fe-loaded chitosan composites on phosphate removal from the secondary effluent (Table 2-2, Qinghe Wastewater Treatment Plant). When the dosage was 5 and 10 g L^{-1}, both of the removal efficiencies of phosphate were higher than 96%, indicating that the Fe-loaded chitosan complex had a good ability to remove phosphate from the real effluents.

2.3.5 Kinetics, isotherms and thermodynamic

(1) Adsorption kinetics

To investigate the potential rate-controlling steps of phosphate adsorption onto CTS-Fe and CTS-Fe-CL composites, the pseudo-first-order and pseudo-second-order models were fitted with the kinetic data. It was evident that the pseudo-first-order and the pseudo-first-order kinetic models were fitted well with the experimental data (Fig. 2-5A), regarding correlation coefficient both in the two adsorbents (data were shown in Table 2-3). Also, the pseudo-second-order kinetic showed better linear correlation coefficients (R^2) than the pseudo-first-order kinetic, and the calculated equilibrium adsorption capacity (pseudo-second-order model) also agreed well with the experimental data. The results indicated that the chemisorption was the primary control step in the phosphate adsorption process (Magdy & Altaher, 2018).

The Elovich model is one of the most useful models for describing chemical adsorption process and previous studies reported that adsorption based on the Elovich equation rose rapidly with a shorter time, and rose slightly with a longer time (Wu et al., 2009). The rate of Elovich equation depended on equilibrium factor of the Elovich equation (R_e), which were classified as four zones: rises slowly ($R_e > 0.3$, zone I), rises mildly ($0.1 < R_e < 0.3$, zone II), rises rapidly ($0.02 < R_e < 0.1$, zone III) and instantly approaches equilibrium ($R_e < 0.02$, zone IV) (Wu et al., 2009). The R_e values of phosphate adsorption for CTS-Fe (0.102) and CTS-Fe-CL (0.124) in Table 2-3 demonstrated that they all fall in zone II with "mildly rising" of Elovich equation. Moreover, the correlation coefficients (R^2) of Elovich model for the two adsorbents were higher than the other two models. Consequently, the Elovich equation was suitable for this experiment, suggesting the phosphate adsorption was a process with slow chemisorption.

The model of intra-particle diffusion can reveal the rate controlling steps. The fitting results indicated that there were two steps in the whole adsorption process (Fig. 2-5B). The first stage was attributed to the reaction of adsorption occurred on the external surface of adsorbent or the boundary layer, and the second stage of the internal diffusion adsorption process is rate limiting. However, the step of equilibrium and stabilization process was not appeared in this study, which further demonstrated that the adsorption of phosphate was a slow process.

The parameter of k_{1d} in the intra-particle diffusion model was more significant than k_{2d} for both of the two adsorbents (shown in Table 2-3). Also, R^2 of the initial stage of adsorption process was better than the R^2 of the second stage. It indicated that the intra-particle diffusion was the rate controlling step at the initial time of the adsorption process (Liu & Zhang, 2015).

Moreover, the four segments of the straight line did not pass through the origin, implying intra-particle diffusion was not the only rate controlling step during the process of phosphate adsorption for both of the two adsorbents.

(2) Adsorption isotherms

Adsorption isotherm models can express the relationship between the equilibrium concentration of adsorbate and the amount of adsorbate uptake. The Langmuir and Freundlich isotherm models can provide valuable information to understand the phosphate adsorption mechanism (Fig. 2-6). The fitting parameters of the different models were shown in Table 3. It was observed that the correlation coefficients (R^2) described by the Freundlich isotherm ($R^2 >$ 0.980) were higher than the Langmuir isotherm ($R^2 <$ 0.950) for both of the two adsorbents under different temperatures. It suggested that these two adsorbents had multilayer heterogeneous adsorbent surface with varying sites of adsorption.

Previous studies demonstrated that the surface heterogeneity parameter ($1/n$) with the range of $0.1 < 1/n < 1$ and the dimensionless constant R_L in the range of $0 < R_L < 1$ represented favorable (shown in Table 3) (Nanta et al., 2018; Vázquez et al., 2007). It was obvious that the calculated $1/n$ and R_L values for CTS-Fe and CTS-Fe-CL in this study were all within the above scope, indicating that the process of phosphate adsorption was favorable. In addition, the R_L constants decreased with the increase of temperature, confirming that high temperature would facilitate phosphate adsorption process.

The maximum phosphate sorption capacity for CTS-Fe and CTS-Fe-CL were estimated to be 15.7 and 10.2 mg-P g^{-1} at 303 K, respectively, which was higher than that of some reported adsorbents, such as the chitosan modified zeolite (CMZFA) (4.05 mg-P g^{-1}) (Xie et al., 2013), magnetic iron oxide nanoparticles (5.03 mg-P g^{-1}) (Yoon et al., 2014), (PVA) hydrogel beads with aluminum ion (11.5 mg-P g^{-1}) (Hui et al., 2014) and Fe-Mn binary oxide (11.7 mg-P g^{-1}) (Zhang et al., 2009a).

(3) Thermodynamic study

To further analyze the influence of temperature on the overall adsorption reaction, the thermodynamic of the phosphate adsorption experiment was investigated at different temperatures of 293, 303 and 313 K (Fig. 2-7). The variations including free energy change ($\Delta G°$), enthalpy ($\Delta H°$) and entropy ($\Delta S°$) for the adsorption processwere determined in this study. It can be seen from Table 4, negative values of $\Delta G°$ and positive $\Delta H°$ at all temperatures revealed that the phosphate adsorption process for both of the two adsorbents was spontaneous and endothermic (Amer & Awwad, 2018). Furthermore, the free energy ($\Delta G°$) decreased with the increase of temperature for CTS-Fe (from -13.81 to -15.35 kJ mol^{-1}) and CTS-Fe-CL (from

-12.89 to -14.04 kJ mol^{-1}), suggesting that a higher driving force and more spontaneous adsorption at high temperature (Ren et al., 2008). The positive value of entropy ($\Delta S°$) for CTS-Fe (77.29 J mol^{-1} K^{-1}) and CTS-Fe-CL (51.76 J mol^{-1} K^{-1}) indicated that the randomness at the solid/liquid interface was increased during the phosphate adsorption process (Joshi & Manocha, 2017).

2.3.6 Mechanisms for phosphate adsorption on CTS-Fe and CTS-Fe-CL

(1) FTIR

To investigate the mechanism of phosphate adsorption processes, the FTIR spectra of CTS-Fe and CTS-Fe-CL before and after adsorption was analyzed and exhibited in Fig. 2-8. The strong broadband in the region of 3500-3300 cm^{-1} was attributed to the overlap between O–H and N–H stretching vibration, and intermolecular hydrogen bonds in the spectrum of Fe-CTS complex demonstrated that coordination of the Fe to CTS occurred. The bands of 2923 and 2858 cm^{-1} were assigned to C–H stretch vibrations of methylene and methyl groups, respectively. The peak at 1657 cm^{-1}could be attributed to the acetylated amino groupon CTS, while the IR bands near 1380 cm^{-1} corresponded to –CH symmetric bending vibrations –CHOH. The characteristic band at 1070 cm^{-1}and the broadband at 500-800 cm^{-1} were related to C–O and metal-oxygen (Fe–O) bonds in the coordinated complexes, respectively (Zhang et al., 2015). The FTIR spectrum of CTS-Fe was shown in Fig. 2-8a, the characteristic peak of main nitrogenous functions (–NH$_2$) in chitosan at 1600 cm^{-1} was almost disappeared after adsorption, suggesting that –NH$_2$ was involved in phosphate adsorption. By contrast, the band of –NH$_2$ on CTS-Fe-CL (Fig. 2-8b) was not observed neither before nor after adsorption, due to the crosslinking reaction between the amine groups in chitosan and the aldehyde groups of glutaraldehyde (Spinelli et al., 2004). Furthermore, a moderately active band was observed at 1716 cm^{-1} in FTIR spectrum of CTS-Fe-CL, which mightcorrespond to pendant aldehyde groups (Mahaninia & Wilson, 2015; Sowmya & Meenakshi, 2014) and it disappeared after adsorption.

(2) XPS

XPS was an essential index to determine the functional groups on the surface of adsorbents. To further verify the results from FTIR analysis, the XPS spectra of the CTS-Fe and CTS-Fe-CL microspheres before and after adsorption was also conducted to explain the mechanism in this work. Wide scan XPS spectra of the CTS-Fe indicated the presence of Fe, O, C, N and P elements (Fig. 2-9A). A new peak at the binding energy (BE) around 130.0 eV~135.0 eV appeared after adsorption under pH 4.0 and pH 10.0 (Fig. 2-9A.a), which might be attributed to the P 2p orbital (He et al., 2017). This result demonstrated the successful loading of phosphate on the surface of chitosan-Fe sorbents. Furthermore, all spectra showed a central peak centered at ~725.0 eV (Fe $2p_{2/3}$) and a shakeup satellite peak at ~711.0 eV (Fe $2p_{1/2}$) (Fig. 2-9A.b), indicating that the Fe doped on chitosan was in the form of hydrated ferric oxide (Zhou et al., 2018). After the phosphate adsorption under pH 4.0 and pH 10.0, a slight shift of the Fe $2p_{2/3}$ peaks binding energy was observed, proving the interaction between Fe (III) and phosphate. Moreover, a similar result was also found for the CTS-Fe-CL composite (Fig. 2-9B).

The O 1s spectra of CTS-Fe before and after phosphate adsorption was displayed in Fig. 2-10A. Three individual component peaks were well fitted at 530.12, 531.5 and 532.8 eV, which could be ascribed to oxygen bonded to the metal (M–O), hydroxyl bonded to the metal (M–OH), and bonded water (H_2O), respectively (Zhou et al., 2018). The detailed fitting parameters were presented in Table 2-6. After the adsorption, the area ratio for the peak at 531.5 eV was related to M–OH, which was decreased from 35.1% to 31.5% in pH 4.0, while the relative areas for the peak of M–O was increased from 2.4% to 5.9%. Moreover, the area ratio of bond water remained almost unchanged. By contrast, the reduction of M–OH area ratio at pH 10.0 was less than pH 4.0, confirming that the M–OH played a crucial role in the phosphate adsorption process under acidic conditions.

Similar results were also observed in O 1s spectra of CTS-Fe-CL (Fig. 2-10B), the percentage of M–OH was noted to drop from 27.3% to 19.2% and 22.6% under pH4.0 and pH10.0. While the rate of M–O increased from 3.2% to 6.3% and 4.0%, respectively. Furthermore, the binding energy of 531.5 eV (M–OH) was apparently shifted to lower energy level of 531.1 eV after adsorption both at pH 4.0 and pH 10.0. The changes of area ratio and binding energy at M–OH suggested that hydrolysates of iron on the adsorbent surface participated in the phosphate adsorption process.

The N 1s spectrum of the two samples before and after adsorption was also investigated. The N 1s spectrum of the initial CTS-Fe (Fig. 2-10C) was deconvoluted at binding energies of 399.5 ($–NH_2$), 400.7 (–NH–) and 401.9 eV ($–NH_3^+$), respectively (Feng et al., 2017). After phosphate adsorption at pH 4.0, the characteristic peak for $–NH_2$ groups showed apparent shifts of 0.3 eV. Moreover, the percentage of $–NH_2$ groups dropped from 68.5% to 59.4%, while the protonated species ($–NH_3^+$) decreased from 16.9% to 10.1% (Table 2-6). These decreases suggested that protonated amine in CTS-Fe facilitated the electrostatic attraction with phosphate for the efficient adsorption. After adsorption at pH 10.0, the percentage of $–NH_3^+$ decreased from 16.9% to 12.6%, indicating that $–NH_3^+$ participated in the adsorption reaction under alkaline conditions. While the reduced proportion of $–NH_2$ group was attributed to the presence of a large number of hydroxide ions in solution, which was consistent with the result of pH.

Comparing with CTS-Fe, the amount of $–NH_2$ on CTS-Fe-CL dropped to 22.3% (Fig. 2-10D), which was due to the crosslinking reaction between aldehyde groups of glutaraldehyde and amine groups in chitosan. The area ratio for the peak of $–NH_2$ groups decreased by 8.2%, which may be ascribed to the protonation of $–NH_2$ groups. The similar results were observed in CTS-Fe-CL after adsorption at pH 4.0. The relative areas for the peak of protonated amine on CTS-Fe-CL decreased from 31.9% to 29.9%, and the binding energy shifted from 401.7 to 401.9 eV, which might be attributed to the electrostatic interaction between protonated amine and phosphate. After adsorption under pH 10.0, the area ratio for the peak at 399.2 related to $–NH_2$ decreased from 22.3% to 11.5%, while the area ratio of $–NH_3^+$ increased from 31.9% to 40.4%. The increasing percentage of $–NH_3^+$ should be ascribed to the protonation of $–NH_2$. Thus, it can be speculated that the groups of N on CTS-Fe-CL did not participate in the adsorption reaction with phosphate under alkaline conditions.

2.3.7 Mechanisms analysis

Adsorption kinetics, isotherms and thermodynamic analysis showed that the adsorption of phosphate on the two adsorbents were slow and endothermic adsorption process and were dominated by chemisorption process. In addition, the analysis of FTIR, XPS and results of pH further revealed the mechanisms of phosphate adsorption for both of the two adsorbents:

(1) During the adsorption process at pH 4.0, the adsorbent would form a positively charged surface and enhanced its electrostatic attraction to negatively charged phosphate, which caused by the protonation of NH_2 groups. Meanwhile, the reduction of area ratio for M-OH suggested that trivalent iron hydrolysates on adsorbent did participate in the adsorption reaction with phosphate. Thus, it can be speculated that the electrostatic interaction (Rajeswari et al., 2015) and ligand exchange (Zhou et al., 2018) processes might be the dominant mechanism for phosphate adsorption on CTS-Fe and CTS-Fe-CL under acidic conditions. Furthermore, the adsorption capacity of CTS-Fe-CL was lower than CTS-Fe, which was caused by a high level of consumption of amine groups for CTS-Fe-CL during the crosslinking reaction.

(2) During the adsorption process at pH 10.0, the increased OH^- content resulted in the negatively charged adsorbent surface, and thereby weakened the electrostatic attraction between the surface of adsorbent and phosphate. The mechanism of phosphate adsorption on CTS-Fe and CTS-Fe-CL at a high value of pH were mainly depended on ligand exchange process. However, the XPS spectra of CTS-Fe proved the slight reduction percentage of $–NH_3^+$

groups, indicating that a weak electrostatic attraction occurred at pH 10.0.

In addition, the monovalent $H_2PO_4^-$ was more easily combined with metal (hydr) oxide surfaces than other ionic species. Consequently, both of the two adsorbents exhibited a reduced ability for phosphate adsorption at alkaline conditions, which could be also ascribed to the predominant ionic species HPO_4^{2-} and PO_4^{3-} at a higher pH. The possible mechanisms of adsorption process were shown in Fig. 2-11.

2.3.8 Regeneration studies

For regeneration, the most important aspect is to return the polymeric material to its original state without altering its indented properties in order to reuse the same material which makes the process cost effective. The saturated adsorbents of CTS-Fe and CTS-Fe-CL were treated with 0.5 M NaOH solution for the time of 60 min. Then, the CTS-Fe and CTS-Fe-CL composites were washed with deionized water and dried at room temperature, which were used again for the adsorption of phosphate under predetermined conditions. The regeneration studies were carried out up to five cycles (Fig. 2-12). The first three regeneration cycles showed that the removal efficiency of phosphate by CTS-Fe and CTS-Fe-CL was maintained at more than 80%. The electrostatic interaction between the phosphate anions and the protonation of NH_2 groups weakened in a highly basic medium and the OH^- ions replaced the phosphate anions. It was evident that the phosphate removal capacity of the adsorbent was decreased from the fourth regeneration cycle. In addition, after the 5th regeneration cycle, the phosphate removal efficiency and the adsorption capacity of the crosslinked adsorbent decreased to be 42% and 2.1 mg-P g^{-1}, respectively. In contrast, phosphate removal efficiency in raw CTS-Fe was maintained at 60% or more. It can be seen that the raw CTS-Fe had better regenerative capacity than the crosslinked CTS-Fe. As the number of regeneration cycles increases, the loss of positive sites on the adsorbent may be responsible for the reduced regeneration efficiency of the Fe-loaded chitosan composite. The study of regeneration showed that the adsorption capacity of Fe-loaded chitosan complex decreased after multiple regeneration cycles. However, chitosan has been widely used in agricultural fields as a soil conditioner due to its antibacterial property and metal chelation ability (Hataf et al., 2018). Therefore, the CTS-Fe composites after initial adsorption of phosphate has the potential as a soil conditioner and can reduce the use of phosphate fertilizer and regenerant.

2.4 Summary

In this part, the CTS-Fe and CTS-Fe-CL were successfully synthesized and conducted to remove phosphate from aqueous solutions. Moreover, the adsorption mechanism of the two adsorbents and the pathway of phosphate transition were also revealed. The following results can be obtained:

(1) Based on the results of SEM and BET analysis, the CTS-Fe had a compact structure with tightly inhomogeneous folds and extremely few pores (average pore width 6.6 nm), while the CTS-Fe-CL exhibited a three layer of structure: brain striatum surface, mesoporous transitional layer (average pore width 14.7 nm), and honeycomb inner core. The Vickers hardness test revealed that the CTS-Fe had a stronger hardness than the CTS-Fe-CL.

(2) Kinetic, isotherm and thermodynamic studies demonstrated that the phosphate adsorption process was spontaneous and endothermic for both of the two adsorbents, and chemisorption dominated the control step. The maximum phosphate sorption capacity for CTS-Fe and CTS-Fe-CL were estimated to be 15.7 and 10.2 mg-P g^{-1} at 303K, respectively.

(3) FTIR and XPS analysis indicated that the phosphate adsorption strongly depended on the pH, and the primary mechanism of adsorption was ligand exchange and electrostatic attraction processes. The high adsorption capacity of the two adsorbents in acidic conditions (pH 3.0-7.0) was due to the strong electrostatic interaction between their adsorption sites and phosphate. Monovalent ion of $H_2PO_4^-$ combined with metal (hydr) oxide by ligand exchange process. Additionally, the study of coexisting ions also proved that an acidic condition was more conducive for phosphate adsorption.

Table 2-1 Surface areas and porosities of CTS-Fe and CTS-Fe-CL.

Adsorbent	**S_{BJH} (m^2 g^{-1})**	**V_{total} (cm^3 g^{-1})**	**D_p (nm)**
CTS-Fe	1.18	0.01	6.62
CTS-Fe-CL	85.66	0.34	14.69

S_{BJH}: BJH surface area, V_{total}: total pore volume, D_p: The mean pore size.

Table 2-2 The component of secondary effluent (pH: 8.4) from Qinghe wastewater treatment plant.

Index	**Concentration (mg L^{-1})**
TOC	8
Nitrate	12
Ammonia	2.6
Bicarbonate	16.5
Sulfate	79.6
Phosphate	5.9

Table 2-3 Kinetic model parameters for phosphate adsorption by CTS-Fe and CTS-Fe-CL.

Model	**Adsorbent**	
	CTS	**CTS-CL**
Pseudo-first-order		
k_1 (h^{-1})	0.847	0.624
q_e (mg g^{-1})	4.286	3.784
R^2	0.944	0.940
Pseudo-second-order		
k_2 (g mg^{-1} h^{-1})	0.296	0.231
q_e (mg g^{-1})	4.545	4.058
R^2	0.986	0.986
Elovich		
α (mg g^{-1} h^{-1})	202.481	44.010
β (g mg^{-1})	2.073	1.955
R^2	0.999	0.995
R_e	0.102	0.124
Intra-particle diffusion		
k_{1d} (mg g^{-1} $h^{-1/2}$)	0.590	0.680
R_1^2	0.991	0.991
k_{2d} (mg g^{-1} $h^{-1/2}$)	0.174	0.156
R_2^2	0.977	0.958

Table 2-4 Isotherm models parameters for phosphate adsorption by CTS-Fe and CTS-Fe-CL.

Parameters	**CTS-Fe**			**CTS-Fe-CL**		
	293 K	**303 K**	**313 K**	**293 K**	**303 K**	**313 K**
Langmuir						
q_{max} (mg g^{-1})	15.576	15.725	15.839	9.199	10.223	10.189
K_{L} (L mg^{-1})	0.046	0.055	0.065	0.136	0.115	0.146
R^2	0.941	0.942	0.924	0.897	0.882	0.874
R_{L}	0.098-0.685	0.083-0.645	0.071-0.606	0.036-0.424	0.042-0.465	0.033-0.407
Freundlich						
K_{F} (mg g^{-1})	2.024	2.144	2.384	2.529	2.585	2.609
$1/n$	0.423	0.426	0.416	0.280	0.298	0.305
R^2	0.993	0.995	0.992	0.998	0.992	0.985

Table 2-5 Thermodynamic parameters for phosphate adsorption by CTS-Fe and CTS-Fe-CL.

	T (K)	**K_c (mL g^{-1})**	**$\Delta G°$ (kJ mol^{-1})**	**$\Delta S°$ (J mol^{-1} K^{-1})**	**$\Delta H°$ (kJ mol^{-1})**
CTS-Fe	293	289.48	-13.81	77.29	8.83
	303	329.01	-14.60		
	313	364.88	-15.35		
CTS-Fe-CL	293	198.23	-12.89	51.76	2.29
	303	212.33	-13.49		
	313	219.90	-14.04		

Table 2-6 The fitting parameters of O 1s and N 1s peak of CTS-Fe and CTS-Fe-CL before and after adsorption in different conditions of pHs.

Adsorbent		**Peak**	**B.E. (eV)**			**Percent (%)**		
			Initial	**pH 4**	**pH 10**	**Initial**	**pH 4**	**pH 10**
CTS-Fe	O 1s	-C-O-/H_2O	532.86	532.86	532.86	62.6	62.6	62.8
		M-OH	531.5	531.5	531.5	2.4	5.9	3.4
		M-O	530.12	530.12	530.12	35.1	31.5	33.8
	N 1s	$-NH_2$	399.5	399.2	399.5	68.5	59.4	60.7
		-NH-	400.7	400.5	400.5	14.7	30.5	26.7
		$-NH_3^+$	401.9	401.7	401.9	16.9	10.1	12.6
CTS-Fe-CL	O 1s	-C-O-/H_2O	532.4	532.4	532.4	69.5	74.5	71.4
		M-OH	531.5	531.1	531.1	3.2	6.3	4.0
		M-O	530.12	530.12	530.12	27.3	19.2	22.6
	N 1s	$-NH_2$	399.2	399.3	399.2	22.3	14.1	11.5
		-NH-	400.2	400.2	400.2	45.8	56.0	48.1
		$-NH_3^+$	401.7	401.9	401.7	31.9	29.9	40.4

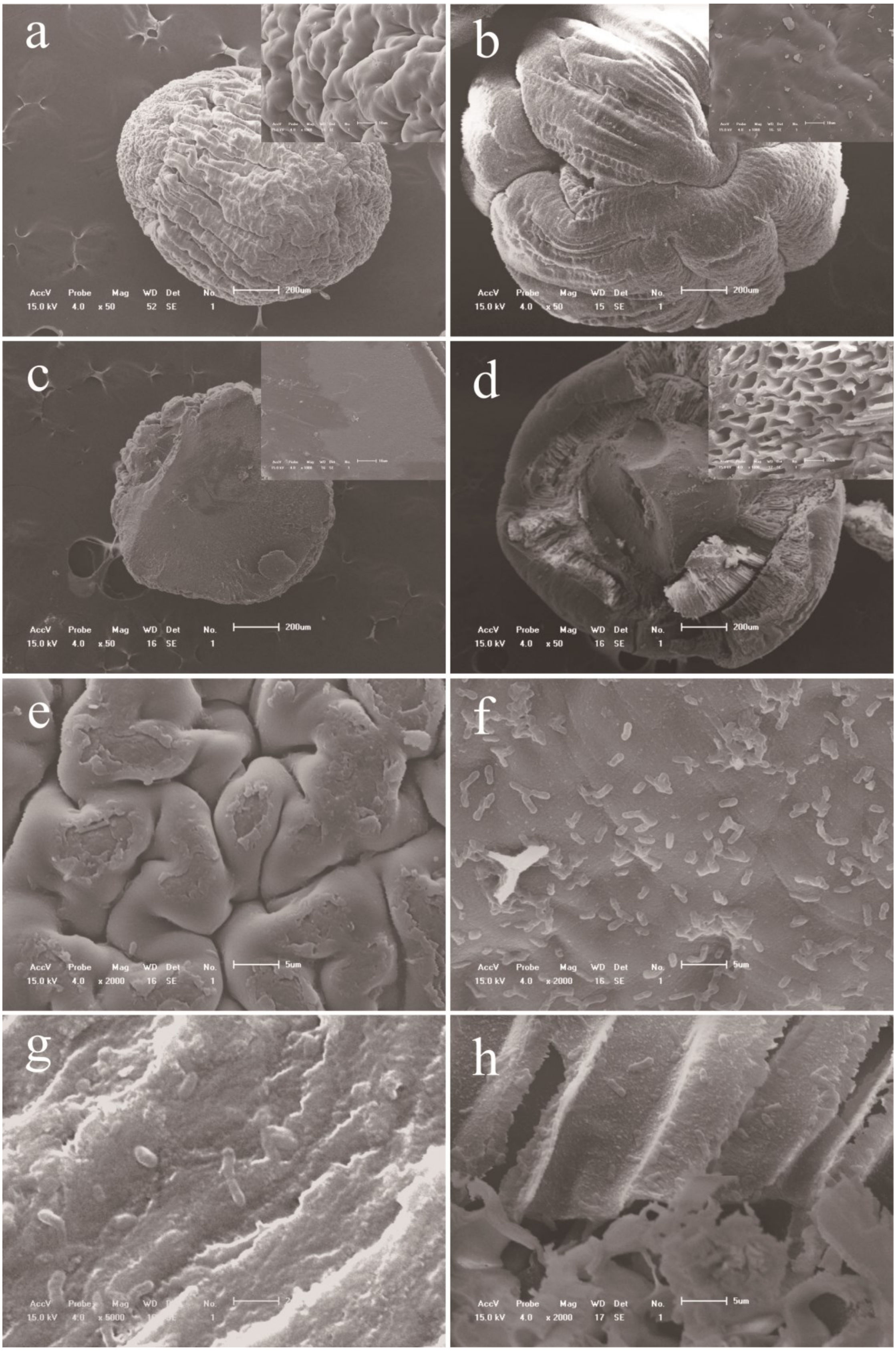

Fig. 2-1 SEM images of CTS-Fe surface before (a) after (e) and inside before (c) after (g) phosphate adsorption; CTS-Fe-CL surface before (b) after (f) and inside before (d) after (h) phosphate adsorption.

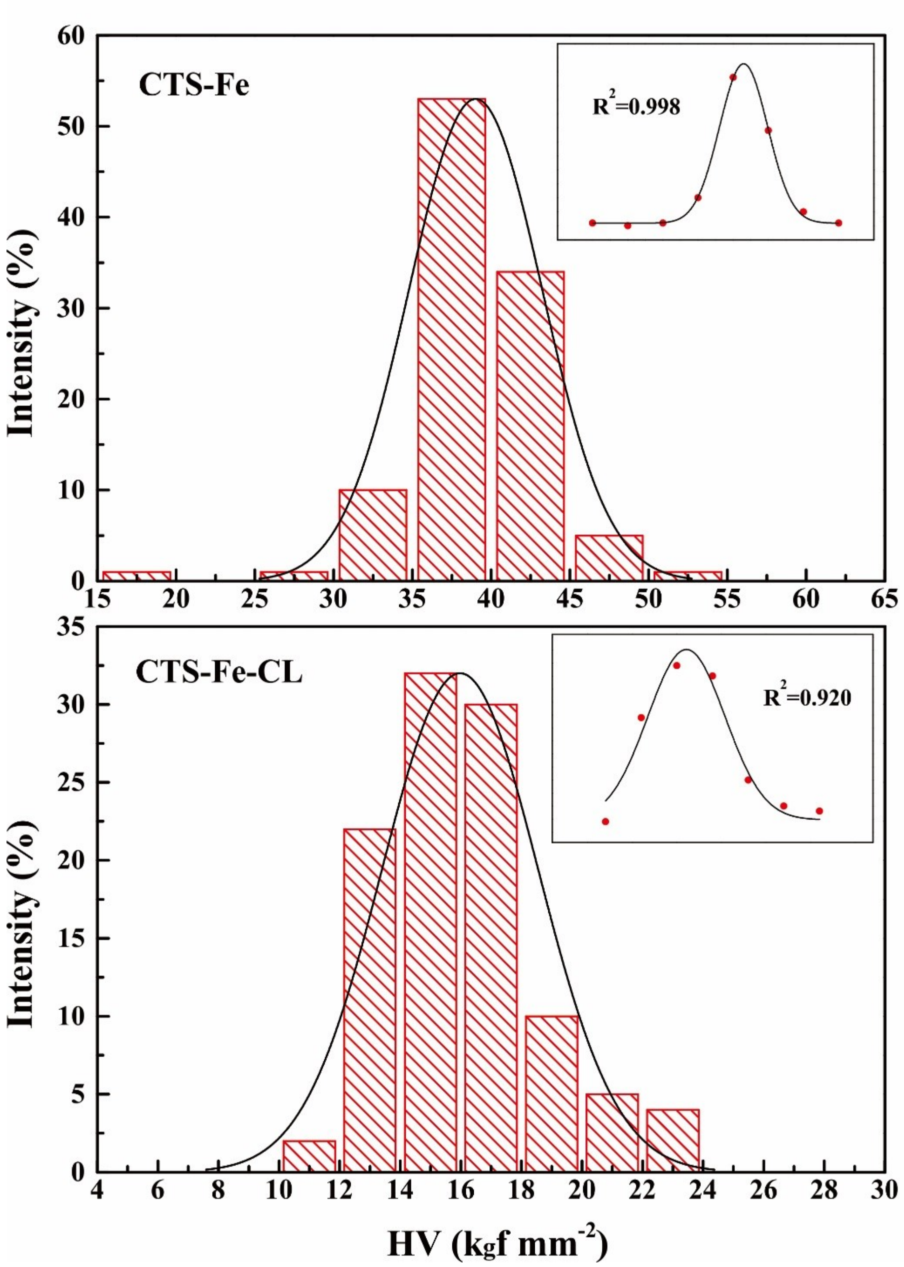

Fig. 2-2 Vickers hardness distribution of CTS-Fe and CTS-Fe-CL.

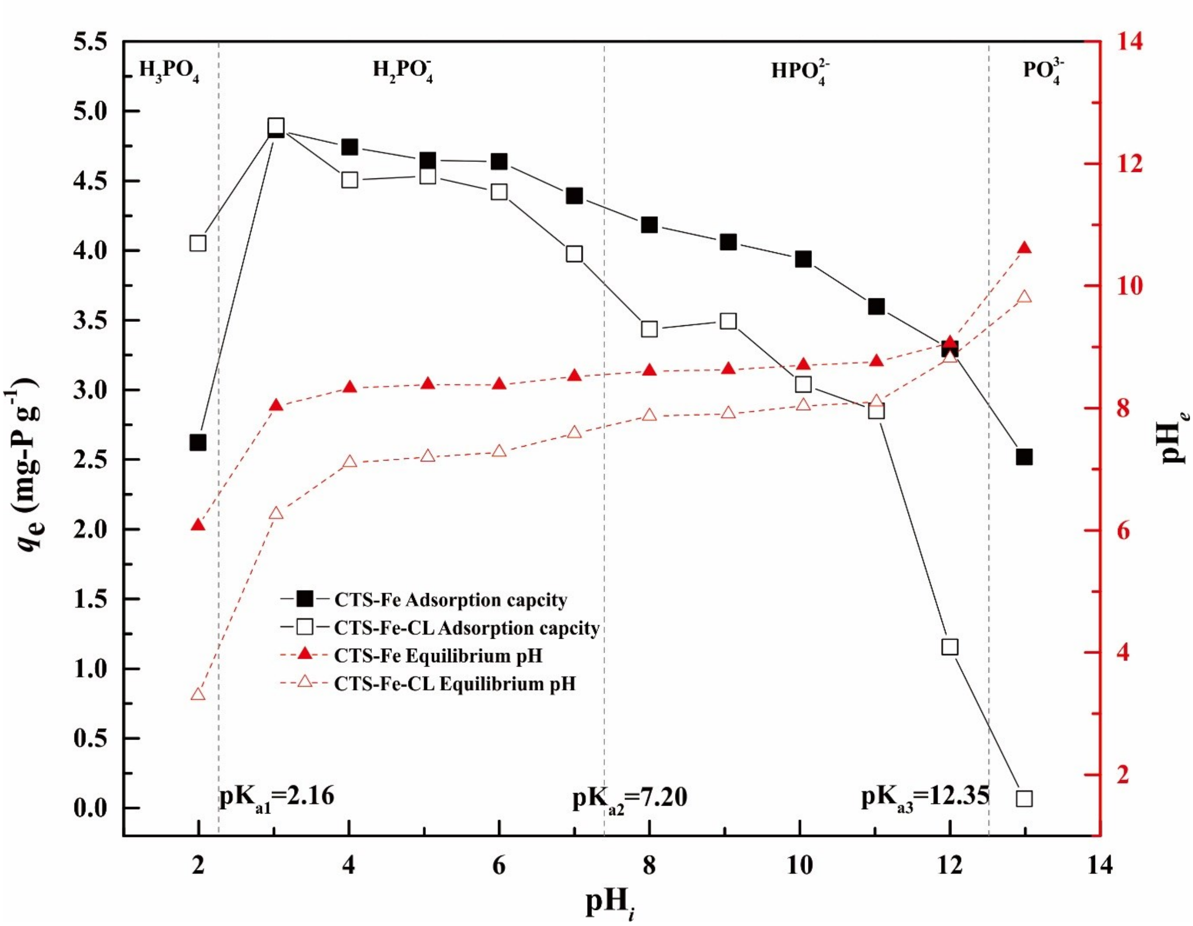

Fig. 2-3 Effect of pH on phosphate removal (adsorbent dosage 10 g L^{-1}, initial concentration 50 mg-P L^{-1}, contact time 48 h, temperature 303 K).

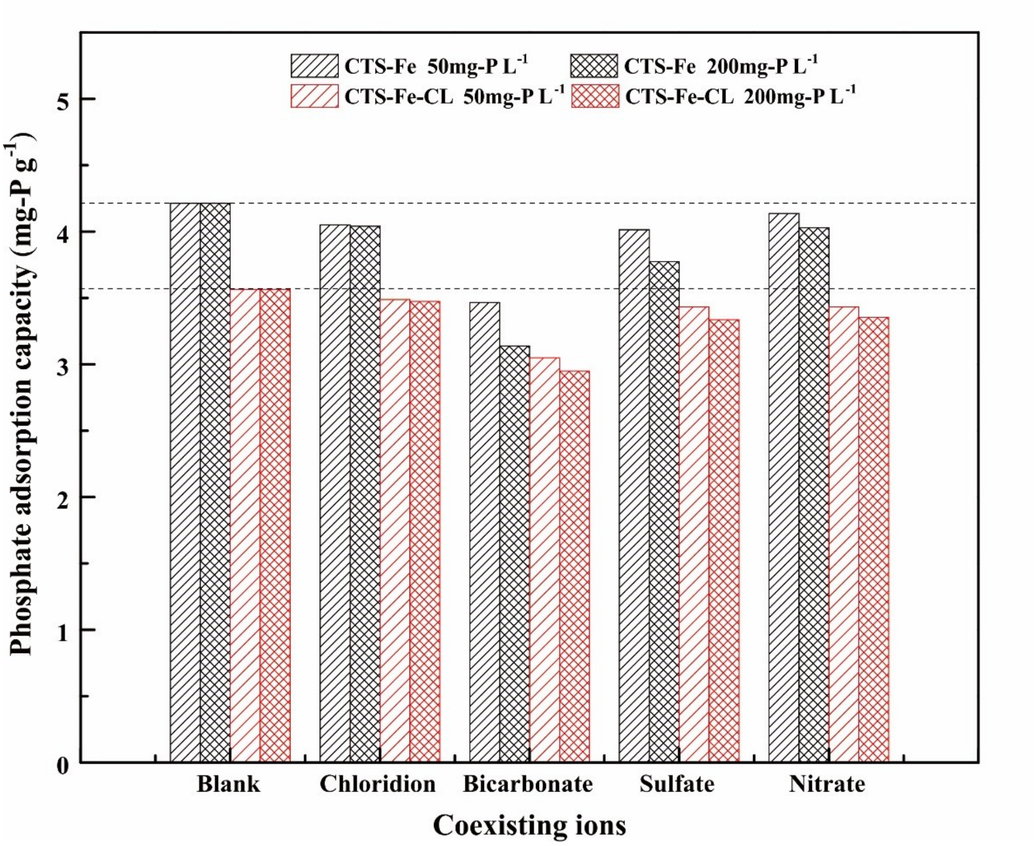

Fig. 2-4 Effect of coexisting ions on phosphate adsorption (adsorbent dosage 10 g L^{-1}, initial concentration 50 mg-P L^{-1}, contact time 48 h, temperature 303 K).

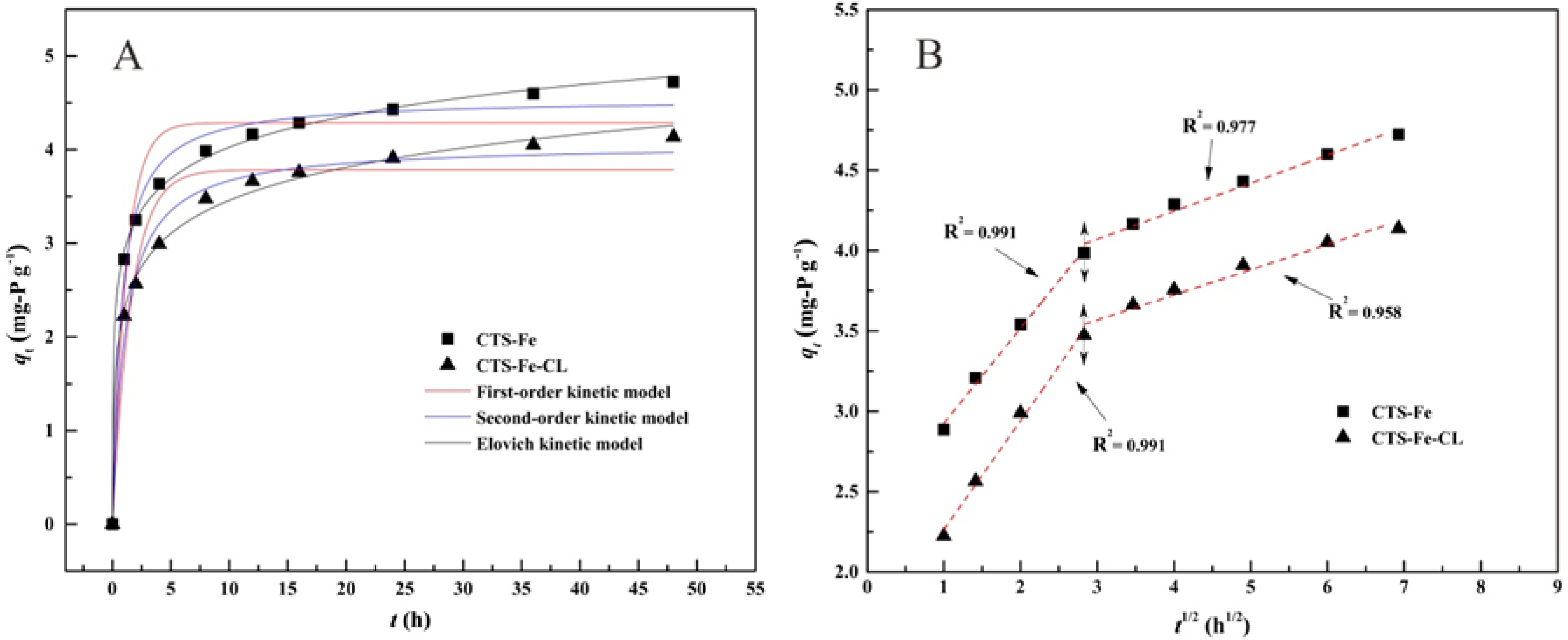

Fig. 2-5 Kinetic studies of phosphate removal by CTS-Fe and CTS-Fe-CL with an initial concentration of 50 mg-P L^{-1}: (A) pseudo-first-order, pseudo-second-order, and Elovich kinetic models, (B)Intra-particle diffusion model for adsorption of phosphate removal by CTS-Fe and CTS-Fe-CL.

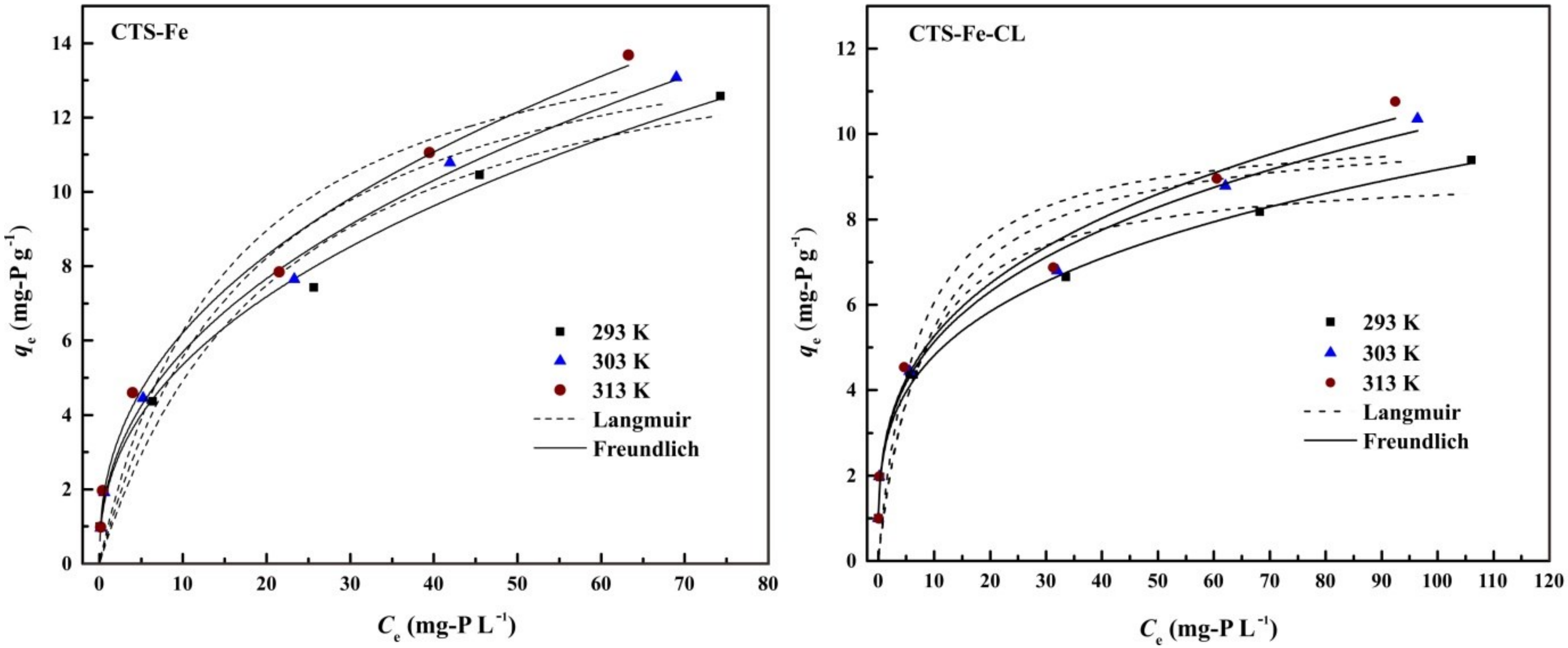

Fig. 2-6 Adsorption isotherm for phosphate removal by CTS-Fe and CTS-Fe-CL: Langmuir and Freundlich isotherm models.

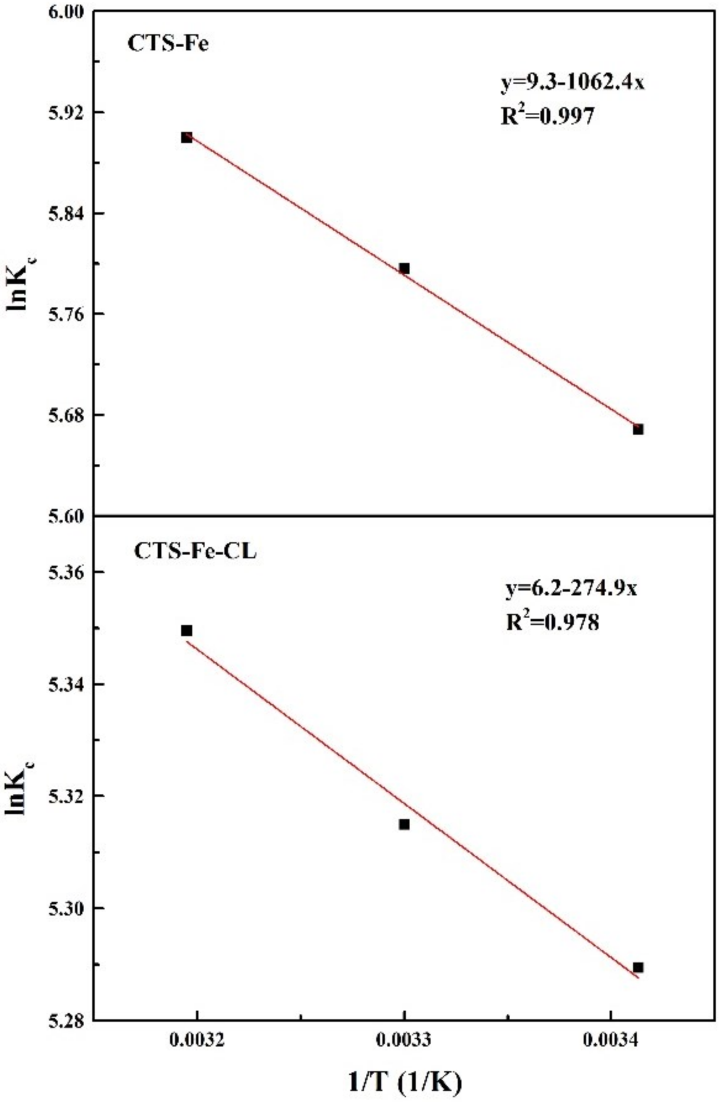

Fig. 2-7 The plot of lnK_c versus 1/T for phosphate adsorption by CTS-Fe and CTS-Fe-CL (initial concentration 100 mg-P L^{-1}).

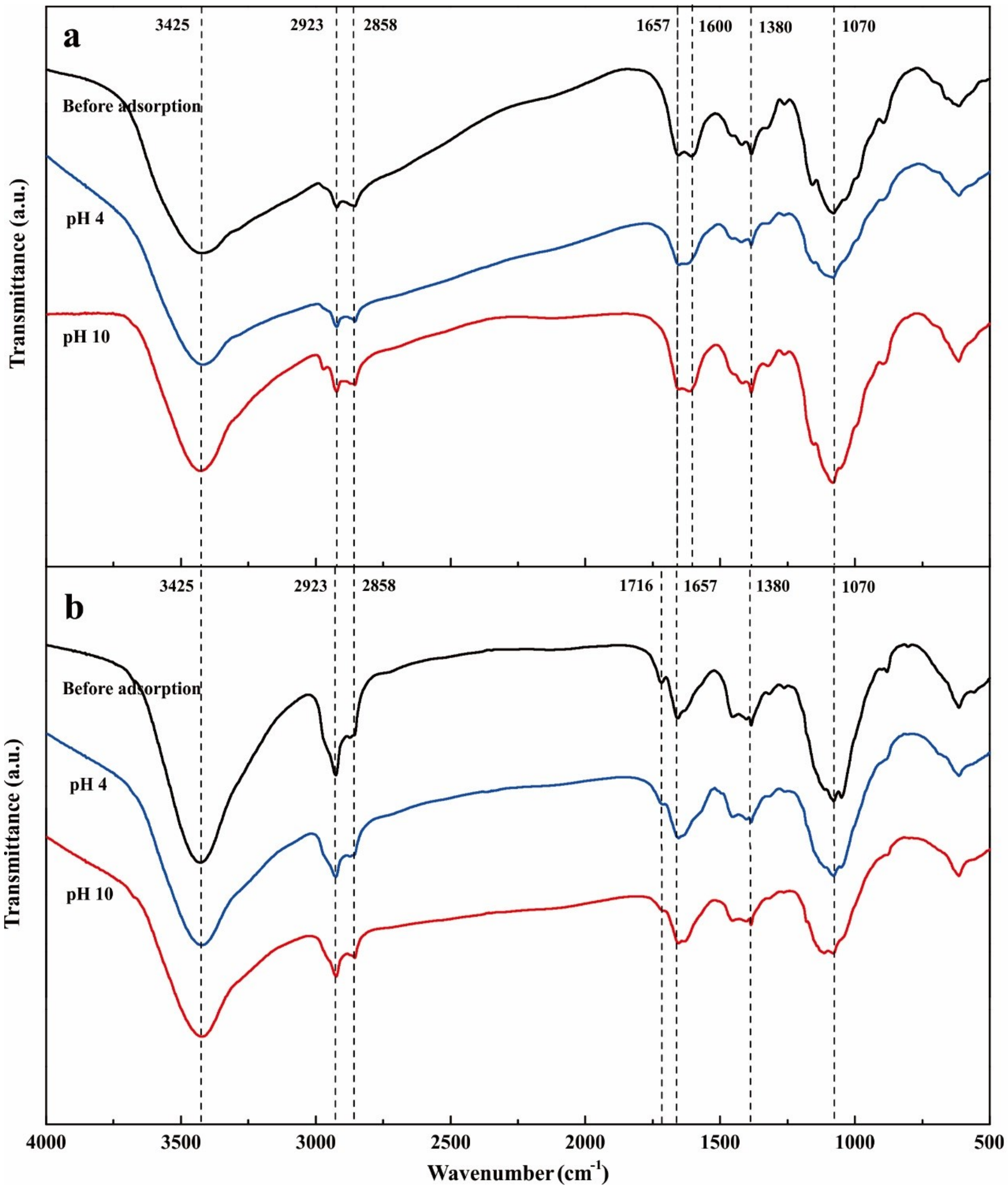

Fig. 2-8 FTIR spectra of the (a) CTS-Fe and (b) CTS-Fe-CL before and after phosphate adsorption in different conditions of pHs.

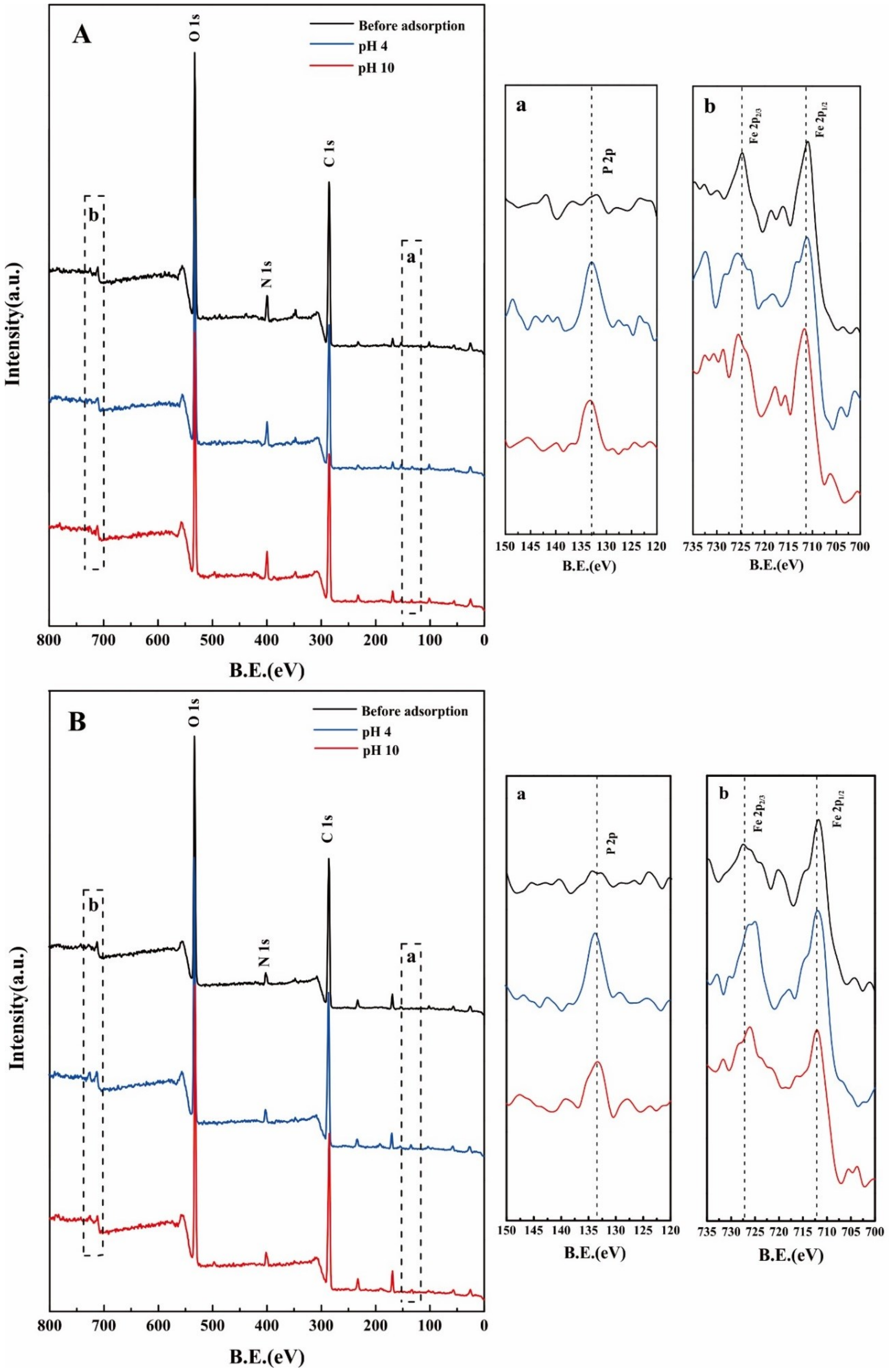

Fig. 2-9 XPS wide scan spectra of (A) CTS-Fe and (B) CTS-Fe-CL before and after phosphate adsorption in different conditions of pH; (a) P 2p and (b) Fe 2p spectra before and after phosphate adsorption.

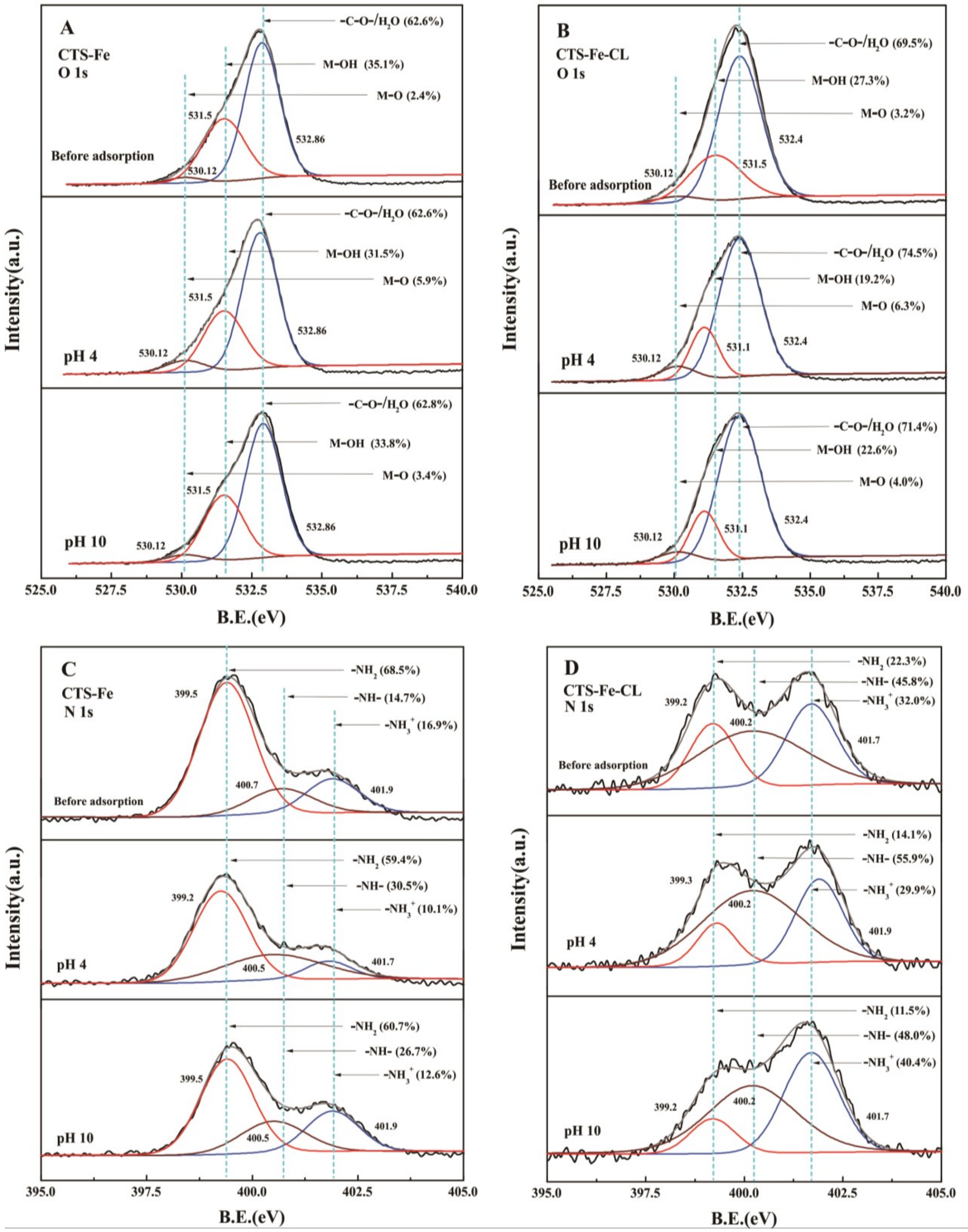

Fig. 2-10 O 1s and N 1s spectra of the (A, C) CTS-Fe and (B, D) CTS-Fe-CL before and after adsorption in different conditions of pHs.

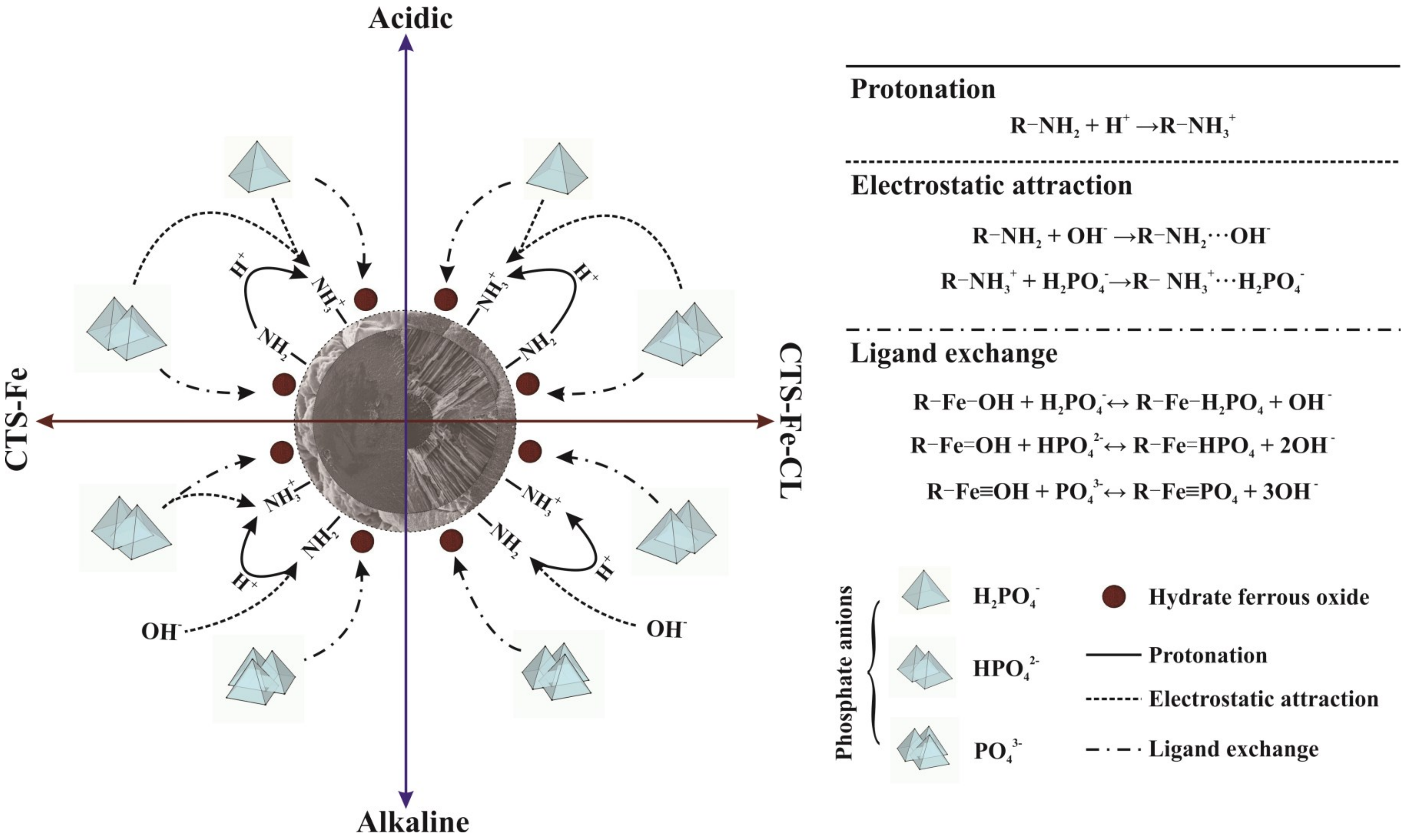

Fig. 2-11 Scheme for the mechanisms of phosphate removal by CTS-Fe and CTS-Fe-CL.

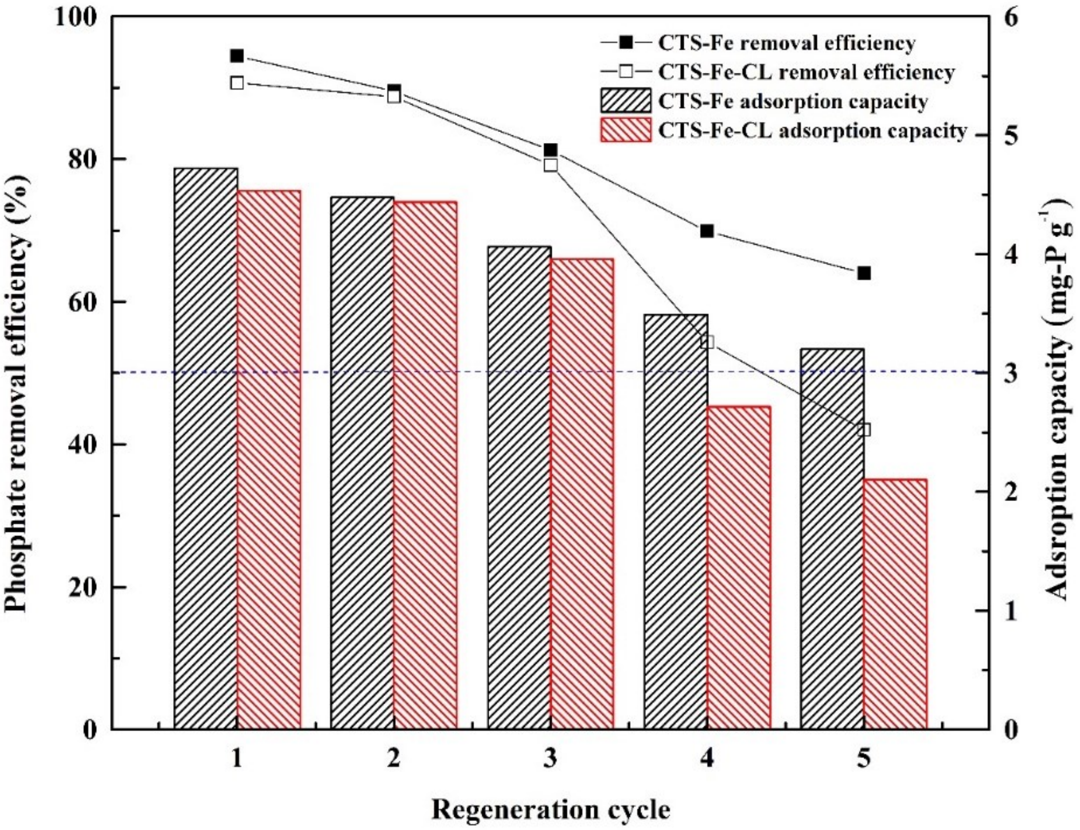

Fig. 2-12 Reusability of CTS-Fe and CTS-Fe-CL for phosphate adsorption.

Chapter 3 Insight into efficient P removal/ recovery from enhanced methane production of WAS with Chitosan-Fe supplementation

3.1 Introduction

AD is currently considered as one of the main methods for WAS disposal, which could achieve resource recovery and reduce environmental risks simultaneously (Luo et al., 2018). However, a large amount of P would be released into the supernatant during AD. Given the phenomenon, an additional treatment process is required before being processed to avoid its negative influence on subsequent application. On the other hand, low methane yield and sludge reduction rate to some extent limit the application of AD in WAS treatment (Zhang et al., 2014). Therefore, the development of new technology for simultaneous P recovery with enhanced AD process from WAS is extensively important.

As demonstrated in Chapter 2, granular chitosan-Fe (III) complex (CTS-Fe) with higher P adsorption capacity (15.7 mg-P/g) than other existing adsorbents has been effectively employed to adsorb phosphate from wastewater. It is worthwhile to note that the Fe on the surface of the CTS-Fe composite may have the ability to recover P as vivianite from WAS during AD process (as mentioned in Chapter 1). Besides, Zhao et al. demonstrated that Fe (III) oxide could enhance WAS digestion through the dissimilatory iron reduction (DIR) process and DIET (Zhao et al., 2018b). Up to now, however, little information is available on the effect of CTS-Fe composites on methane production and P recovery from WAS during AD.

This chapter attempted for the first time to simultaneously recover P and enhance methane production from WAS by adding the Fe-loaded chitosan complex (CTS-Fe). Specifically, the objectives of this study were to: (1) investigate the feasibility of CTS-Fe for P recovery as vivianite from WAS via AD; (2) evaluate the efficacy of CTS-Fe addition on methane production from WAS; and (3) reveal the mechanisms involved in P transformation and pathways during AD of WAS in the presence of CTS-Fe.

3.2 Materials and methods

3.2.1 Material synthesis and preparation

CTS powder (27 g) was first dissolved in 900 mL of 2% (v/v) acetic acid and then $FeCl_3·6H_2O$ (0.1 M) was added to the solution. The solution was continuously stirred for 4 h, and then the mixed solution was added dropwise into an ammonia solution (6.25%, v/v) with a syringe. After standing for 1 h, the obtained gel beads were thoroughly washed with deionized water and dried at 50 °C for 24 h.

In this study, WAS and digested sludge, which represent the substrate and inoculum, respectively, were collected from a domestic WWTPs in Ibaraki Prefecture (Japan) and stored at 4°C before use. The main characteristics of the WAS and digested sludge are shown in Table 3-1.

3.2.2 Batch AD experiments

An 80-mL mixture, which contained WAS (substrate) and digested sludge (inoculum) at a ratio of 8:2 (v/v), was incubated in a 100-mL digestion bottle. To investigate the effects of different CTS-Fe dosage on the AD of WAS, four test groups containing 0, 5, 10 and 20 g/L CTS-Fe (with initial sludge VS/TS=0.77) were operated in parallel and marked as Rc, R1, R2 and R3, respectively. Before digestion, the initial pH was adjusted to 7.2 using 0.1 M HCl or NaOH. Next, the bottles were sealed with rubber stoppers and flushed with nitrogen gas for 3 min and then incubated at 38 ± 2°C for 30 days. At the end of batch AD experiments, the granular CTS-Fe composites were completely separated from the sludge through an 32-mesh sieve (~ 0.5 mm). The obtained granular CTS-Fe composite was washed with deionized water and dried at 50°C for 24 h, and then stored in enclosed plastic bags for subsequent analysis.

3.2.3 Analytical methods

(1) General indices

Total solids (TS) and volatile solids (VS) contents in the sludge samples were determined according to the standard methods (APHA, 2012). Biogas was collected using a gas-tight 60 mL syringe every two days, and the methane content in biogas was analyzed by gas chromatography (GC-8A, Shimadzu, Japan). Volatile fatty acids (VFAs) were quantified by another gas chromatography (GC-14B, Shimadzu, Japan). pH was determined with a pH meter (FE20, Mettler Toledo, Switzerland).

(2) Characterization methods

In this study, the CTS-Fe samples used for characterization were obtained from R2 (10 g/L CTS-Fe) before and after AD. The morphology and elemental composition of the CTS-Fe and the crystals on CTS-Fe surface were analyzed by the scanning electron microscopy (Nanta et al.) coupled with energy dispersion spectroscopy (SEM-EDS; SSX–550, Shimadzu, Japan), while the crystallized phase of the CTS-Fe after AD was analyzed by X-ray diffraction (XRD; D8 Focus, Bruker, Germany). Fourier transform infrared spectrometery (FTIR; Vertex 70V, Bruker, Germany) and X-ray photoelectron spectroscopy (XPS; ESCALAB250Xi, Thermo Fisher, USA) were used to determine the functional groups and their binding states in CTS-Fe. The detailed operation conditions for SEM-EDS, XRD, FTIR, and XPS are described in the Supplementary Data (Table 3-2).

(3) P fractionation in solid sludge by SMT protocol

In this study, the standards, measurements and testing (SMT) extraction protocol was applied to analyze P fractions (García-Albacete et al., 2012). The detailed procedure is presented in the Fig. 3-1. P in the solid phase of sludge can sequentially be determined in five categories: total phosphorus (TP), inorganic P (IP), organic P (OP), non-apatite inorganic P (NAIP; associated with Fe, Al and Mn) and apatite P (AP; Ca-bound). The NAIP and OP are generally deemed as bioavailable P as they can be potentially utilized by microorganisms. The extracted P and phosphate in the liquid phase were measured using the molybdenum blue method (APHA, 2012) with a UV-visible spectrophotometer (UV-1800, Shimadzu, Japan).

3.2.4 Kinetics analysis

To quantitatively analyze the effect of CTS-Fe addition on methane production during AD of WAS, the experimental data from the batch test was fitted by the modified Gompertz equation (Lay et al., 1999):

$$P = P_{max}\, exp\left\{ - exp\left[\frac{R_{max} e}{P_{max}} (\lambda - t) + 1 \right] \right\} \tag{3-1}$$

where P is the observed cumulative methane yield (mL/g-VS); P_{max} is the methane production potential (mL/g-VS); R_{max} is the maximum methane production rate (mL/g-VS·d); λ is the lag phase time (d); t is the duration (d); and e is Euler's number (2.718281).

3.2.5 Statistical analysis

All experiments were conducted in triplicate. The data presented in the results and discussion are average values. For data analysis, one-way analysis of variance (ANOVA) was applied to analyze statistical difference in the experimental data using Microsoft Office Excel 2016. The XPS and XRD results were analyzed by XPSPEAK 4.1 and MDI/JADE 9.0, respectively. Origin 9.0 was used to fit the kinetic model.

3.3 Results and discussion

3.3.1 Effect on methane production

The effects of CTS-Fe addition on cumulative methane yield and daily methane production from WAS are illustrated in Figs. 3-2A and B, respectively. As shown in Fig. 3-2A, methane production was significantly increased under CTS-Fe addition condition. The cumulative methane yields at CTS-Fe dosage of 5.0, 10.0 and 20 g/L of were detected to be 209.9, 236.6 and 247.9 mL/g-VS, respectively, about 12%, 26% and 32% higher than the control (187.5 mL/g-VS).

Much higher daily methane production peak (44.1 mL/g-VS·d) was detected on day 12 in R3 (20 g/L CTS-Fe), compared with that in Rc (31.2 mL/g-VS·d) on day 20 (Fig. 3-2B). In order to make clear the effect of CTS-Fe on methane production from WAS of AD, the relevant parameters obtained by fitting the experimental data to the modified Gompertz model are shown in Table 3-3. The correlation coefficients ($R^2 = 0.994 - 0.998$) suggest the goodness of the Gompertz models fitting to the experimental data, and the predicted results were almost consistent with the experimental results. Compared to the control (Rc), the reactors with CTS-Fe addition (R1, R2 and R3) showed relatively higher methane production. The methane production potential (P_{max}) and the maximum methane production rate (R_{max}) increased with the increase in CTS-Fe dosage, with the maximum increase in P_{max} (24%) observed at 20 g/L of CTS-Fe addition. The R_{max} was increased by 13 - 33% under the addition of CTS-Fe. In addition, the lag time for methane production was shortened by 40% when 20 g/L of CTS-Fe was supplemented. These results indicate that CTS-Fe addition could significantly enhance the methane production from AD of WAS. The enhanced methane production was probably ascribed to the promoted anaerobic hydrolysis–acidification of complex matters in WAS by Fe (III) on the surface of CTS-Fe, beneficial for methanogenesis and organics mineralization (Zhang et al., 2014). Besides, CTS-Fe as the carbon-based material may be able to stimulate DIET to boost electron transfer between the substrates and microbes (Lin et al., 2017).

3.3.2 Effect on VFAs evolution

The variation of VFAs during the AD process is shown in Fig. 3-3A. Acetic and propionic acids are the two main constituents, accounting for 31.5% and 19.5% of the total VFAs (468.9 mg-COD/L), respectively, in the raw WAS. In the reactors with CTS-Fe addition, the maximum VFAs concentrations of 2239.8 mg-COD/L (5 g/L), 2328.5 mg-COD/L (10 g/L), and 2494.2 mg-COD/L (20 g/L) were respectively detected in R1-R3 on day 3. In contrast, a lower maximum VFAs concentration in the control (2144.1 mg-COD/L) was noticed on day 6. The concentrations of VFAs, however, declined rapidly thereafter in all the reactors, attributable to the consumption by methanogens. This observation is in accordance with the methane production trend. Moreover, as shown in Table 3-4, the VS reductions in the CTS-Fe reactors were increased by about 1.04 - 1.22 times that in the control (27.4%). Meng et al. (2013) demonstrated that the enhancement of organic matter reduction was related to the improved activity of hydrolytic enzymes under the addition of Fe^0. The observation in this study suggests that CTS-Fe may promote the hydrolysis of WAS with improved VS reduction and VFAs production during the AD process.

Moreover, the concentrations of propionic acid in the CTS-Fe reactors were detected to decrease faster than in the control, indicating that CTS-Fe may promote the decomposition of propionate. This result is consistent with (Zhang et al., 2014) who observed that the rusty scrap improved the conversion of propionate in AD of WAS.

3.3.3 Changes in P fractionation during AD

In order to investigate the distribution and migration of P in WAS during the AD process, this study used the SMT protocol to extract P fractions in the solid phase and determined the proportions of P in the solid and liquid phases.

As shown in Table 3-5, most of the P (66.3%) in the raw WAS were distributed in the solid phase, in which OP occupied < 4.0% of TP and maintained at 1.83 ± 0.03 mg/g-SS (Fig. 3-4B) during the whole AD process. From the analysis of P mass balance, the P concentration in the liquid phase of WAS in Rc increased by 39.5% at the end of digestion with a corresponding P reduction in the solid phase. It has previously been reported that this decrease may be brought about by the decomposition of extracellular polymeric substances (EPS) that release P-containing organic matter, which can be then hydrolyzed into ortho-P (Chen et al., 2019; Monea et al., 2020). Compared with Rc, the increase in P concentration in the liquid phase of WAS was not detected in the CTS-Fe added reactors (Fig. 3-4A and Table 3-5), in which the TP in the liquid digestate decreased from 371.81 to 17.58 mg-P/L at the end of experiment under the addition of 20 g/L of CTS-Fe (R3). This confirms that CTS-Fe could effectively adsorb phosphate from the liquid digestate of WAS. It was noteworthy that the content of OP (solid phase of the sludge) slightly increased when the CTS-Fe dosage was increased from 5 g/L (R1) to 10 g/L (R2), possibly due to the increased number of microorganisms, such as acidogenic bacteria and sulfate-reducing bacteria (SRB) (Yang et al., 2019), which needs further investigation.

On the other hand, IP (in solid) dominated the raw WAS (94.2% of TP in the solid of sludge) with NAIP and AP amounting to 73.5% and 26.5% of the IP, respectively (Fig. 3-4B). During the AD process, the NAIP and AP contents in the solid phase in the CTS-Fe added reactors decreased with the increase in CTS-Fe dosage, which notably decreased from 21.54 to 14.82 mg/g-SS and 7.76 to 3.68 mg/g-SS at 20 g/L of CTS-Fe, respectively. In contrast, the NAIP and AP contents in the sludge slightly decreased by 2.77 and 1.50 mg/g-SS in Rc, respectively. Previous studies have shown that iron addition can increase the NAIP content in sludge during AD process. (Li et al., 2019b) claimed that the NAIP in sludge with iron addition increased by 14% compared to the raw sludge. However, in this work, the NAIP and AP contents in sludge in R3 (20 g/L of CTS-Fe addition) decreased by 31.2% and 52.6% after 30 days' AD, respectively. This observation implies that the added CTS-Fe may stimulate the transformation of IP in the solid phase of sludge and then release $Fe^{2+/3+}$-like ions into the liquid phase, and the latter can further enhance the removal and recovery of phosphate from the liquid digestate during the AD process.

Moreover, NAIP and OP, which are generally regarded as potentially bioavailable P, accounted for 75.3% of TP in the raw sludge. Results show that the bioavailable P was increased to 79.9% (5 g/L), 81.8% (10 g/L) and 82.0% (20 g/L) in the three CTS-Fe added reactors on day 30, respectively, most probably attributable to the decreased TP content in the sludge with the increase of CTS-Fe dosage.

Under the test conditions, P adsorption capacity of CST-Fe decreased from 91.43 mg/g (R1) to 59.98 mg/g (R2), and 36.15 mg/g (R3), much higher than its use for the treatment of synthetic phosphate-containing wastewater (15.70 mg/g, 30°C) (as mentioned in Chapter 2). This observation is mainly due to much higher initial phosphate concentration (~ 370 mg/L) and more complex composition of the liquid digestate involving more pathways to remove P in this study.

3.3.4 Characterization of CTS-Fe

(1) FTIR

To investigate the mechanisms of P removal and recovery, the FTIR spectra of CTS-Fe before and after AD process were analyzed (Fig. 3-5). The bands at 1657 and 1594 cm^{-1} can be assigned to acetylated amino group (–NH_2) on CTS. The characteristic peak at 1594 cm^{-1} almost disappeared after AD, meaning that amino might be partially substituted. Furthermore, a new peak appeared at 1325 cm^{-1} (C-N stretching of amide III) after AD (Ntohogian et al., 2018). The absorption bands at 1157 and 1028 cm^{-1} correspond to asymmetric stretching of C-O-C bridge and hydroxyl group (CH_2-OH) stretching, which was weakened after AD (Barbosa et al., 2019).

The absorption bands at 896, 661 and 419 cm^{-1} are related to metal-oxygen (Fe–O) bonds in the complexes (Cornell & Schwertmann, 2003; Deng et al., 2016; Tofik et al., 2016). It is obviously seen that the adsorption bands shifted from 661 to 562 cm^{-1} and weakened at 896 and 419 cm^{-1} after AD. Moreover, the band at 1070 cm^{-1}, associated with the asymmetry vibration of sorbed PO_4^{3-} (Li et al., 2014; Tofik et al., 2016), increased in intensity after AD. All the above results suggest that the stretching bands of Fe-O were involved in P adsorption on the surface of CST-Fe.

(2) XPS

XPS is a useful tool to determine the material's surface functional groups. To further explain the mechanisms involved in this work, the XPS spectra of the CTS-Fe composites were analyzed. The XPS spectra of O, N, Fe and P for the samples before and after AD are shown in Fig. 3-6, and the detailed fitting parameters are presented in Table 3-6. The wide scan XPS spectra of CTS-Fe indicated the presence of O, N, Fe and P elements (Fig. 3-6A). A new peak at the binding energy around 130.0 eV assigning to P 2p was clearly observed on CTS-Fe after AD, suggesting that phosphates were successfully adsorbed onto CTS-Fe.

The spectrum of O 1s can be deconvoluted into three individual component peaks (Fig. 3-6B). The peaks well fit at 530.1, 531.5 and 532.8 eV, probably attributable to the oxygen bonded to metal (M–O), the hydroxyl bonded to metal (M–OH) and the bonded water (H_2O), respectively. After the AD process, the binding energies of the three peaks of O 1s shifted to 530.8, 531.7 and 532.9, respectively. The area ratio of the M–OH peak decreased from 15.4% to 10.0%, while the relative area of the M–O peak increased significantly from 9.8% to 19.1%. The variations of the binding energy and area ratio at M–OH suggest that the iron hydrolysate on the surface of CST-Fe participated in AD during the phosphate adsorption process by ligand exchange. As previously reported, CTS can interact with many transition metal ions through a chelation mechanism (Qu et al., 2011). Therefore, the change in the M-O peak might be associated with the combination of added metal and material itself during the AD process.

The N 1s spectrum of the pristine CTS-Fe (Fig. 3-6C) well fits with the two peaks at 399.5 and 401.3 eV. The first peak exhibits a greater intensity, which is associated with the presence of non-protonated ($–NH_2$ or –NH–) amino groups while the peak at 401.3 eV can be assigned to the presence of protonated amino groups ($–NH_3^+$) (de Godoi et al., 2013). A noticeable shift of 0.3 eV was observed in the characteristic peak for protonated species ($–NH_3^+$) after the AD process. The percentage of protonated species increased from 3.3% to 18.1%, while the non-protonated amino group species decreased by 14.8%. This phenomenon can be ascribed to the protonation of amino groups on the surface of CST-Fe, which may attract hydrogen ions in the solution (de Godoi et al., 2013). Additionally, this observation also suggests that electrostatic attraction is not the dominant interaction for P recovery from WAS during the AD process.

To confirm that P was recovered after AD, the P 2p spectra of the CTS-Fe were analyzed. One sharp peak was noticed in the P 2p spectrum after the AD process (Fig. 3-6D). This was decomposed into two main peaks located at 132.9 eV and 133.7 eV, which can be ascribed to PO_4^{3-} and HPO_4^{2-}, respectively (Cui et al., 2016). This result reflects that P was effectively combined with the CTS-Fe complex during AD process with P-containing $M_x(PO_4^{3-})_y$ and $M_x(HPO_4^{2-})_y$ complexes being mainly formed.

In order to identify the chemical valence states of Fe on the surface of the CTS-Fe complex, the Fe 2p spectrum of CTS-Fe was investigated (Fig. 3-6E). For the pristine CTS-Fe, two main peaks were observed at 710.5 (Fe 2p 3/2) and 724.8 eV (Fe 2p 1/2) (Lv et al., 2015). The peak of Fe 2p 3/2 was decomposed into three peaks located at 715.0 eV, 712.9 eV and 710.5 eV, implying that the valence state of iron is Fe^{3+} (Liu et al., 2016). The Fe 2p 3/2 peak is related to the satellite peak at 718.7 eV (Omran et al., 2015). Additionally, another satellite peak at 728.1 eV may also belong to Fe 2p 1/2. After the AD process, two new peaks at 709.9 and 723.8 eV were observed in the positions of Fe 2p 3/2 and Fe 2p 1/2, respectively, representing the Fe^{2+} state (Bae et al., 2018; Shaw et al., 2017). Moreover, the relative areas for the Fe^{3+} peaks decreased from 79.7% to 66.8%, while those of Fe^{2+} increased by 24.5%. These results suggest that a portion of Fe^{3+} might be reduced to Fe^{2+} in the CTS-Fe composite during AD.

(3) XRD and SEM-EDS analysis

In order to determine the morphology and chemical composition of P bound to CTS-Fe after the AD process, XRD and SEM-EDS were performed.

Seen from the XRD results, the CTS-Fe exhibited strong and sharp diffraction peaks after the AD process (Fig. 3-7), well-indexed to vivianite (JCPDS No.75-1186) and Fe_2Fe-pyrophosphate (JCPDS No. 80-2315), the main P-containing crystal phases, accounting for 30.2% and 69.8% (Wt%), respectively (Table 3-7). The SEM images of the CTS-Fe complex before and after AD are provided in Fig. 3-8. The pristine CTS-Fe had tight and uneven striatum folds on the surface (Fig. 3-8A), attributable to uneven volatilization of ammonia and water molecules on the surface of CTS-Fe composite. While widespread distribution of sheet or needle-shaped crystals and amorphous colloids were clearly observed on the CTS-Fe surface after the AD process, whose morphology (Fig. 3-8B and C) agrees with previous reports (Prot et al., 2019; Rothe et al., 2016).

To further determine the composition of crystals on the CTS-Fe surface, EDS analysis was performed after the AD process. The EDS mapping analysis focused on a specific area localized on the SEM image (Fig. 3-8D). Table 3-8 shows the main elemental compositions on the surface of CST-Fe and the recovered crystals. After AD, P was detected on the surface of CTS-Fe and crystals, with contents being about 9.4% and 8.4% (Wt %), respectively. This result again confirmed that the P has been adsorbed on the CTS-Fe surface. It is noteworthy that a small amount of Mg (2.1 Wt%) was detected in the crystals, probably contributed by the structure that allows Fe^{2+} atoms of vivianite to be replaced by other divalent cations. It has been reported that dissolved metallic Mg might appear in sewage and be incorporated into the vivianite structure (Prot et al., 2019; Wang et al., 2019). In this study, the molar ratio of (Fe, Mg) / P was 1.4, which is within the range of the vivianite ratio.

3.3.5 Mechanisms analysis

One major objective of this study is to verify the feasibility of P recovery as vivianite from WAS via AD by CTS-Fe supplementation. In this study, the sequential extraction method as well as material characterization were used to interpret the possible mechanisms and migration pathways of P. Three main aspects will be discussed in this section: (1) the mechanisms of P recovery from WAS and vivianite formation by CTS-Fe addition; (2) the effect of CTS-Fe addition on P transformation and its pathways during AD of WAS; and (3) the effect of CTS-Fe addition on properties of treated WAS.

In this experiment, characterization of the CTS-Fe material before and after AD suggests a possible mechanism of P recovery. The P 2p spectrum indicates that the P on the surface of the material after AD can be grouped into PO_4^{3-} and HPO_4^{2-}. Thus, it is inferred that P is mainly combined with CTS-Fe in these two forms. Previous studies have shown that CTS-Fe can adsorb phosphate from aqueous solution through ligand exchange and electrostatic interaction. The decreased area ratio of M–OH in the O 1s spectrum indicates that this ligand exchange occurred during AD. However, the N 1s spectrum of XPS shows that electrostatic attraction may not occur during the AD process. Therefore, it can be concluded that chemical rather than physical reactions took precedence on the surface of CST-Fe during the AD test.

SEM-EDS results show the formation of a large number of vivianite crystals on the surface of CST-Fe, which is closely related to Fe (III) on the surface of CTS-Fe. The Fe (III) on CTS-Fe can be mainly hydrolyzed to form hydrated iron oxide during AD (Chen et al., 2019). In an anaerobic environment, dissimilatory metal-reducing bacteria (DMRB) can reduce Fe (III) to Fe (II) and then combine with ortho-P to form vivianite crystals (O'Loughlin et al., 2013). The specific equations related are as follows:

$$Fe^{3+} + 3H_2O \rightarrow Fe(OH)_3 + 3H^+ \tag{3-2}$$

$$Fe(OH)_3 + H^+ + e^- \rightarrow Fe(OH)_2 + H_2O \tag{3-3}$$

$$3Fe^{2+} + 2PO_4^{3-} + 8H_2O \rightarrow Fe_3(PO_4)_2 \cdot 8H_2O \tag{3-4}$$

According to a previous report, the rate and extent of Fe (III) reduction largely depends on the Fe (III) sources (Lovley, 1991). (Cheng et al., 2015) found that incomplete reduction of Fe (III) may also occur under anaerobic conditions, even if the electron donors (mainly sludge organics) for Fe (III) reduction in the system are sufficient. In this study, the presence of Fe (III) on CST-Fe was noticed after AD. This phenomenon may be related to the Fe (III) on the surface of the CTS-Fe combined with P through ligand exchange, which can be explained in the following equations:

$$R - Fe = OH + HPO_4^{2-} \leftrightarrow R - Fe = HPO_4 + 2OH^- \tag{3-5}$$

$$R - Fe \equiv OH + PO_4^{3-} \leftrightarrow R - Fe \equiv PO_4 + 3OH^- \tag{3-6}$$

Under anaerobic conditions, phosphate accumulating organisms (PAOs) can degrade long-chain poly-P to short-chain poly-P, pyro-P and ortho-P. In these processes, most of the pyro-P and ortho-P can be leaked to the surrounding EPS matrix (Li et al., 2015a), then phosphate is subsequently released via cell lysis during AD of WAS. In this study, a slight decrease in TP (in solid + liquid) while a remarkable increase of TP in the liquid phase was noticed in the control after AD (Fig. 3-4A and Table 3-5, Rc), suggesting the effective conversion of P in the solid sludge into phosphate in the liquid phase via AD. Compared with the control, significant P removal from the solid and liquid phases were detected in the CTS-Fe added reactors, in which NAIP decreased considerably after AD. It has been reported that the concentration of phosphate in liquid digestate during AD of WAS is closely related to the degree of Fe (III) reduction (Cao et al., 2019; Cheng et al., 2015). In addition, these researchers claimed that the enhanced reduction of Fe (III) to Fe (II) in WAS during AD was mainly contributed by bioreduction process. Therefore, the significant decrease of NAIP in the sludge with CTS-Fe addition may also be attributed to the reduction of Fe (III)-P compounds in the sludge to highly soluble Fe (II)-P compounds with phosphate being released into the liquid digestate, which then can directly interact with CTS-Fe to form an amorphous coordination compound or vivianite crystals, or co-precipitate with each other and/or co-existing metals again on the surface of CST-Fe during the AD process.

Besides phosphate, PAOs may release Mg ions. EDS detected a minor amount of Mg on the surface of CTS-Fe. Theoretically, struvite can also be formed in the test systems; however, XRD did not find this phenomenon. It has been demonstrated that addition of external Fe to anaerobic digesters can hinder struvite formation and that vivianite is preferably formed because it is less soluble than struvite (Mamais et al., 1994; Wang et al., 2019). Moreover, the formation of struvite crystals requires strict pH control at 8.0-10.5 and a suitable molar ratio of Mg to P (Mg:P > 1) (Li et al., 2019a; Zhang et al., 2012). While in this study the pH and molar ratio of Mg:P were lower than 8.0 and 0.4, respectively. Therefore, the Mg detected on CTS-Fe may be attributed to the substitution of Fe^{2+} in the vivianite structure. As mentioned above, the added CTS-Fe can enhance the release of P from sludge in the solid phase and effectively recover P from the liquid phase.

In addition, higher methane production was achieved in the CST-Fe added reactors in this study, probably due to the promotion effect of Fe (III) on the hydrolysis phase of AD as seen from the evolution of VFAs. During the first 6 days, the pH in the control reactor dropped from 7.2 to 6.7 (Fig. 3-3B), owing to the accumulation of VFAs during AD of WAS. In contrast, no similar pH drop was observed in the CTS-Fe added reactors. This is similar to the finding by

(Cheng et al., 2015) who proposed that most of the VFAs produced from AD were probably used as electron donors for Fe (III) reduction, thereby alleviating VFA accumulation and preventing the pH from decreasing. More specifically, methane production in this study was not affected by Fe (III) reduction due to the presence of excess electron donors in the WAS. As a result, the pH slightly increased over the whole AD process in the presence of CTS-Fe, most probably due to the neutralization of H^+ from the free amine groups in the CTS and OH^- released by ligand exchange. In summary, the possible mechanisms involved in the CTS-Fe reactors in this study are illustrated in Fig. 3-9.

3.4 Summary

This study presents Fe (III)-loaded chitosan (CTS-Fe) composite was used to remove and recover P from WAS during AD process. The results demonstrate that P could be effectively recovered as vivianite from AD of WAS through CTS-Fe supplementation, which could also enhance methane production simultaneously by 11.9% - 32.2%. After AD process, the P concentration in the solid and liquid phases were found to decrease with the increase in CTS-Fe dosage, while P bioavailability in the solid sludge was improved. Characterization indicated that in the AD system, Fe (III) on the surface of CTS-Fe was reduced and combined with P to form vivianite crystals through chemical precipitation. However, the unavailability of some Fe (III) on the CTS-Fe surface caused the incomplete reduction of Fe (III) to Fe (II). In this study, P was proposed to be recovered by ligand exchange between phosphate and iron hydrolysates, and CTS-Fe as electron acceptor may minimize the accumulation of VFAs and enhance the AD process of WAS.

Table 3-1 Main characteristics of waste activated sludge (WAS), digested sludge (DS) and mixture sludge used in this study.

Parameters	Unit	WAS	DS	Mixture (WAS+DS)
Total solids (TS)	%	2.87 ± 0.01	1.05 ± 0.05	2.31 ± 0.01
Volatile solids (VS)	%	2.09 ± 0.01	0.76 ± 0.04	1.79 ± 0.01
Total phosphorus (liquid phase)	mg/L	ND	ND	371.81 ± 1.97
Total phosphorus (solid phase)	mg/g-TS	ND	ND	30.94 ± 0.98
pH	-	6.58 ± 0.02	7.03 ± 0.02	6.75 ± 0.01

ND, not determined.
All data were expressed as mean ± SD of triplicate tests.

Table 3-2 The conditions for the analytical characterization of CTS-Fe composites.

Analytical methods	**Conditions**
SEM-EDS	Acc.V: 15.0 KV; Probe: 4.0 um; Mag: 50-2000X+; WD: 17 mm
XRD	CuKα radiation (0.15406 nm); Scan: 10°-80°; Scan speed: 8° Deg/min; Step width: 0.02°
FTIR	Wavenumber range: 400-4000 cm^{-1}
XPS	Binding energy range: 0-1350 eV; Elements: C, N, O, Fe, P

Table 3-3 The relevant parameters obtained by fitting the modified Gompertz model to the experimental data.

Reactor	**CST-Fe addition (g/L)**	**Cumulative CH_4 yield from AD test (mL/g-VS)**	**Kinetic parameters**			
			P_{max} **(mL/g-VS)**	R_{max} **(mL/g-VS·d)**	λ **(d)**	R^2
Rc	0	187.5	207.2	12.84	8.65	0.994
R1	5	209.9	212.8	14.48	5.44	0.997
R2	10	236.6	241.7	16.08	5.45	0.997
R3	20	247.9	257.8	17.05	5.19	0.998

Table 3-4 Total solids (TS) and volatile solids (VS) reduction in the different reactors after 30 days' experiments.

	Raw	**Rc**	**R1**	**R2**	**R3**
TS (%)	2.31	1.80	1.75	1.70	1.65
VS (%)	1.79	1.30	1.28	1.24	1.19
VS reduction (%)	-	27.4	28.5	30.7	33.5

Table 3-5 Phosphorus distribution in the sludge after AD for 30 days.

	Solid (mg)				**Liquid (mg)**			**Total (mg)**
	OP	**NAIP**	**AP**	**Subtotal**	**Ortho-P**	**OP**	**Subtotal**	**(solid+liquid)**
Raw	3.34	39.73	13.99	57.06	28.25	0.81	29.06	86.12
Rc	2.54	30.72	10.86	44.12	40.06	0.48	40.54	84.66
R1	2.42	25.47	7.02	34.91	14.42	0.22	14.64	49.55
R2	2.60	22.32	5.56	30.48	7.47	0.19	7.66	38.14
R3	2.55	19.51	4.84	26.90	1.19	0.19	1.38	28.28

Note: Mass balance was analyzed based on triplicate tests.

Table 3-6 The fitting parameters of XPS spectra to CTS-Fe before and after the AD process.

Elements	**Pristine CTS-Fe**		**CTS-Fe after digestion**		**Assignments**
	B.E. (eV)	**A.C. (%)**	**B.E. (eV)**	**A.C. (%)**	
O 1s	530.1	9.8	530.8	19.1	M–O
	531.5	15.4	531.7	10.0	M–OH
	532.8	74.8	532.9	70.9	–C–O–/H_2O
N 1s	399.5	96.7	399.4	81.9	$–NH_2$ / –NH–
	401.3	3.3	401.0	18.1	$–NH_3^+$
Fe 2p 3/2	710.5, 712.9, 715.0	54.0	711.3, 712.9, 715.1	51.4	Fe^{3+}
	–	–	709.9	19.3	Fe^{2+}
Fe 2p 3/2 (Shake-up)	718.7	6.8	718.6	3.7	Satellite peak
Fe 2p1/2	724.4	25.7	725.0	15.4	Fe^{3+}
	–	–	723.9	5.1	Fe^{2+}
Fe 2p1/2 (Shake-up)	728.1	13.5	727.8	5.1	Satellite peak
P 2p	–	–	132.9	48.7	PO_4^{3-}
	–	–	133.7	51.3	HPO_4^{2-}

Table 3-7 Simple quantitative analysis (semi-quantitative) of the crystal components sample.

Phase ID	**JCPDS ID**	**Int%**	**RIR**	**Wt%**
Vivianite-$Fe_3(PO_4)_2(H_2O)_8$	75-1186	35.0	2.20	30.2
Diiron (III) iron diphosphate-$Fe_2Fe(P_2O_7)_2$	80-2315	67.8	1.85	69.8

Reference intensity ratio (RIR) are from ICSD database pattern I/Icor values.

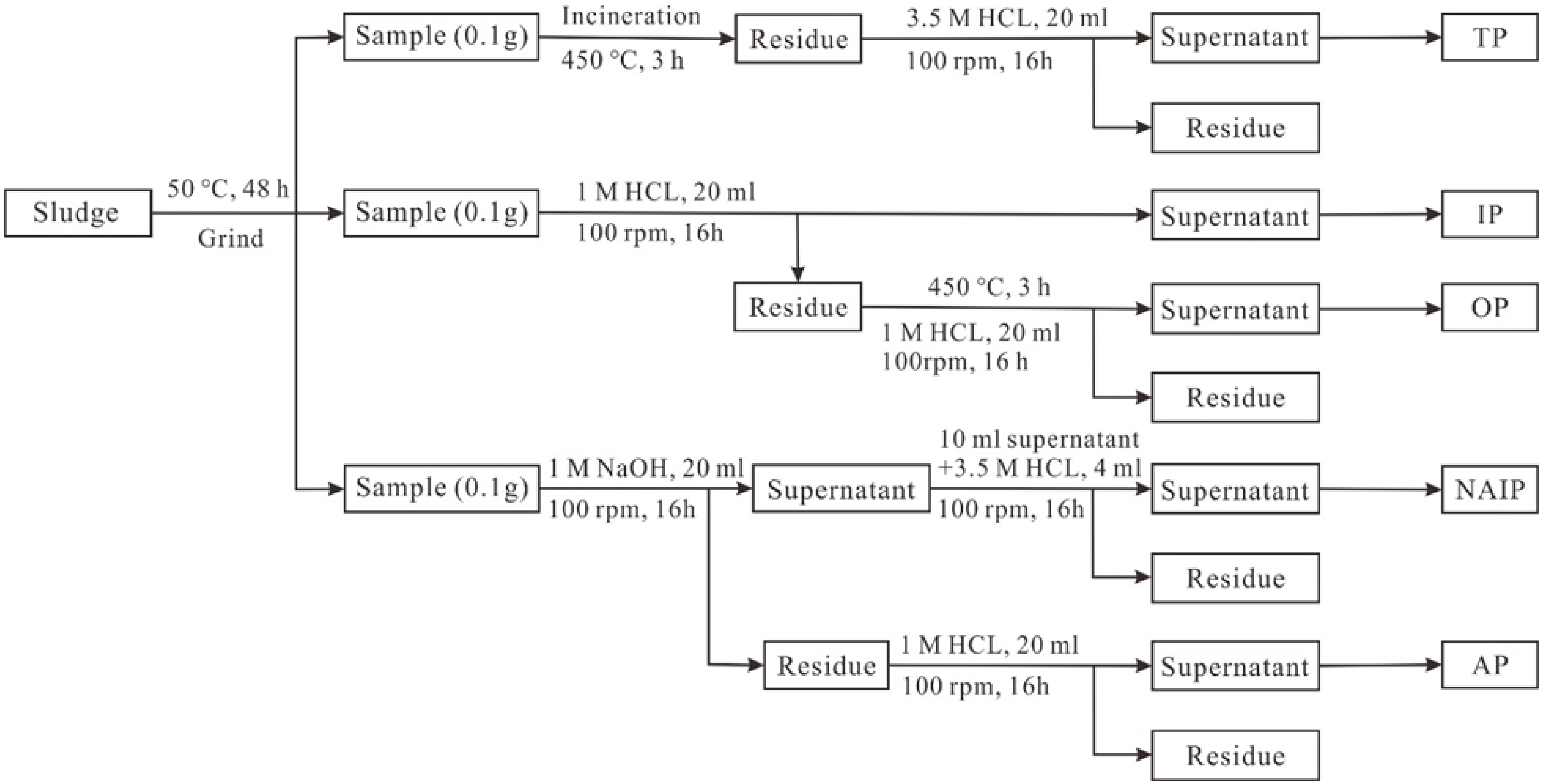

Fig. 3-1 The schematic diagram of the SMT protocol (García-Albacete et al., 2012).

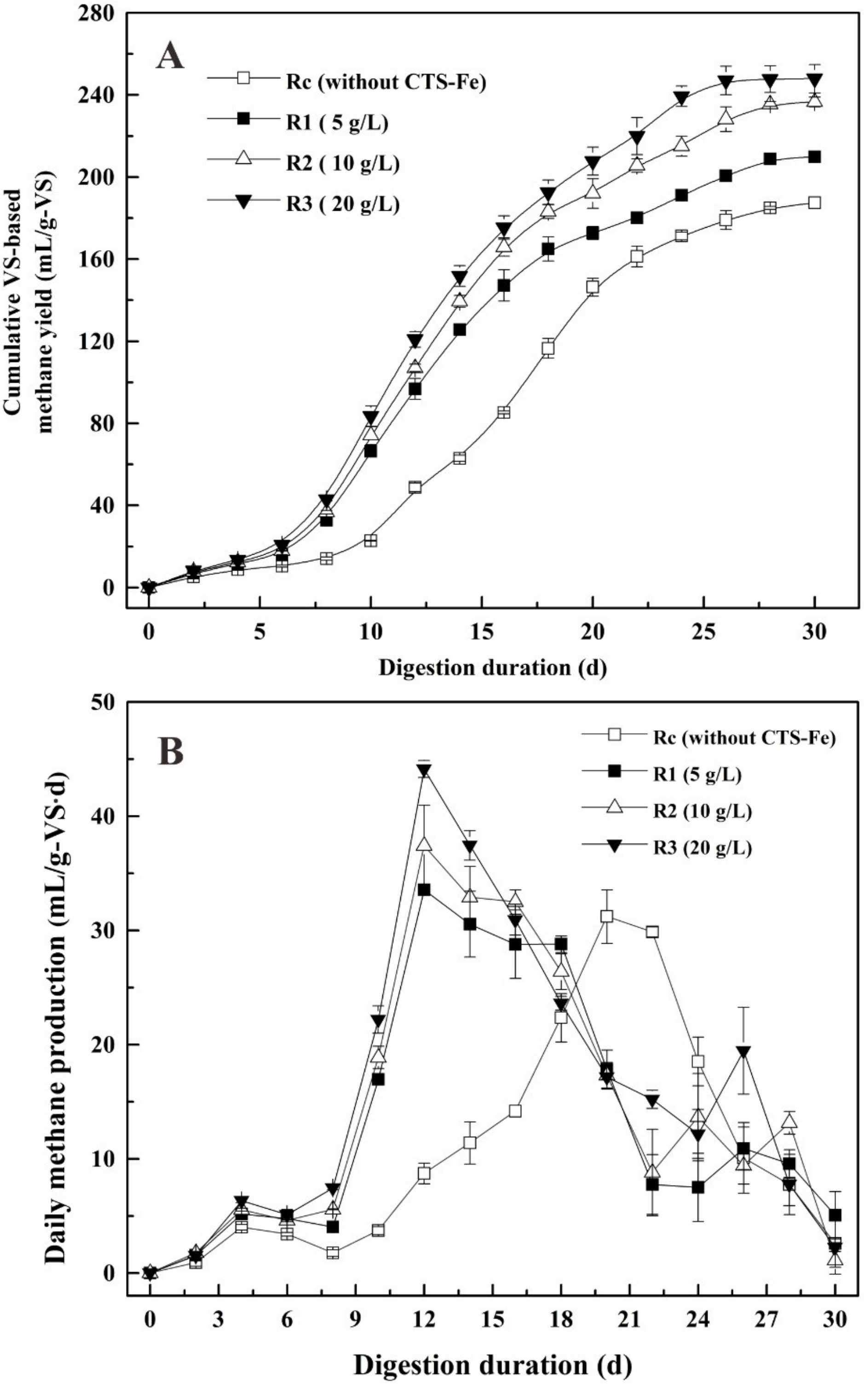

Fig. 3-2 Cumulative methane yield (A) and daily methane production (B) from WAS under different dosages of CTS-Fe.

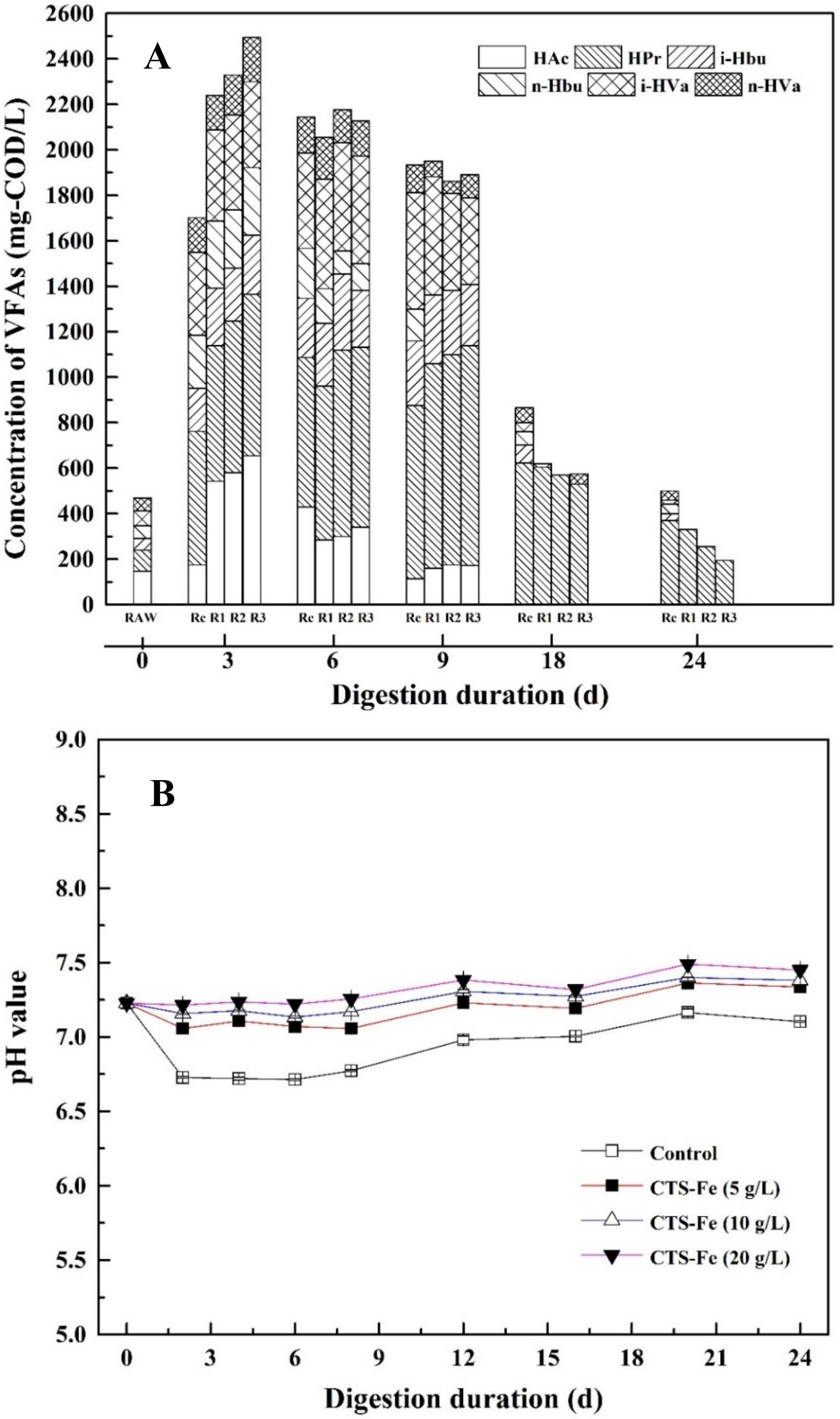

Fig. 3-3 The changes of VFAs composition (A) and pH (B) during the AD process.

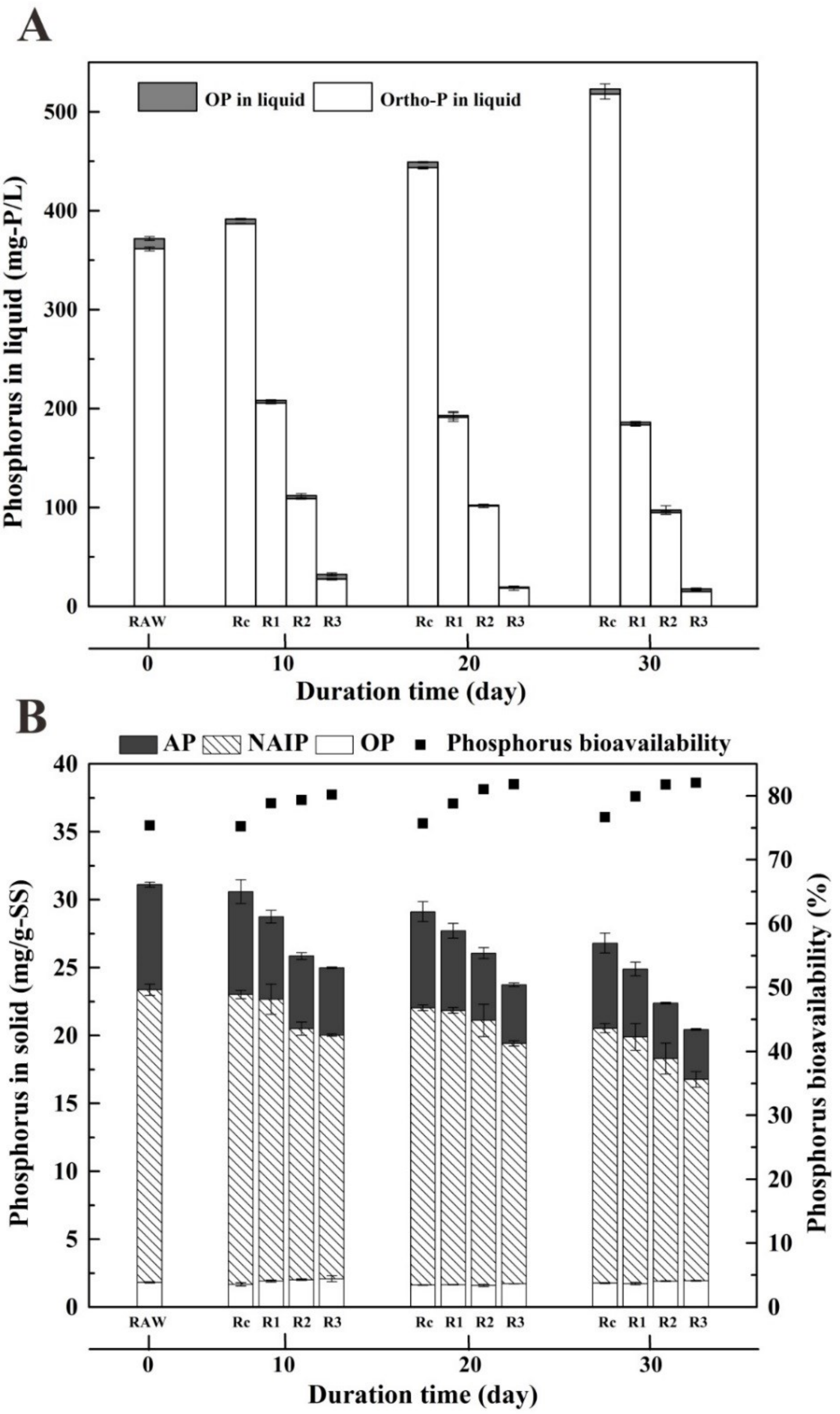

Fig. 3-4 Variation of P distribution in liquid-phase (A) and solid-phase (B) during AD of WAS.

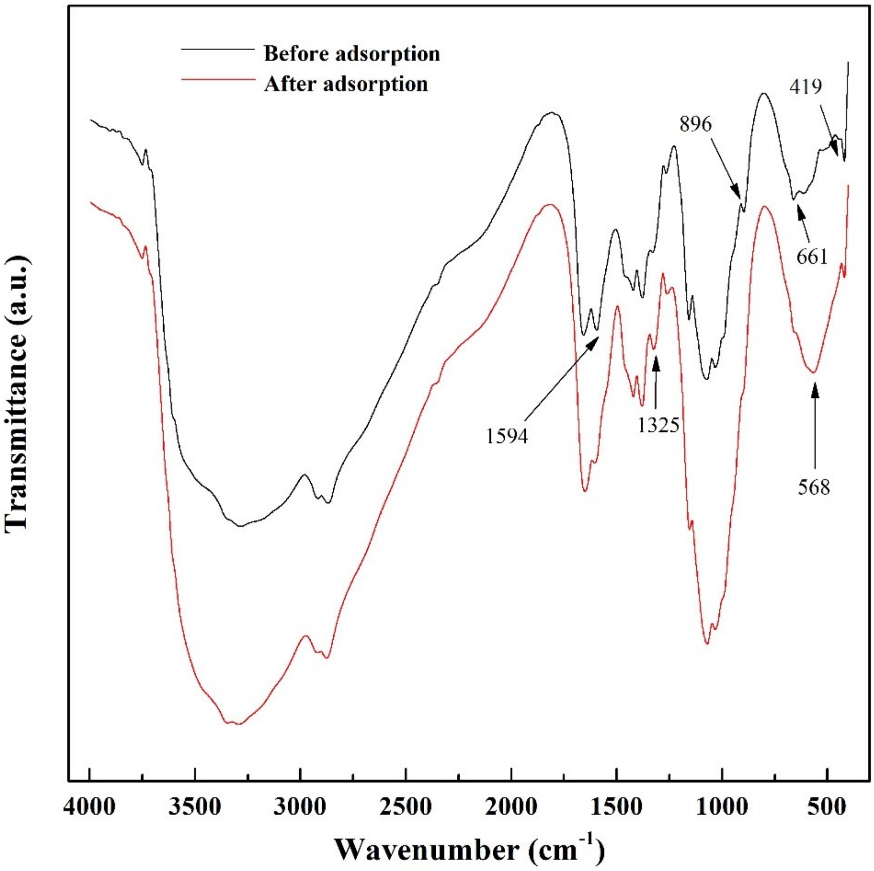

Fig. 3-5 FTIR spectra of the pristine CTS-Fe (red line) and after the AD process (black line).

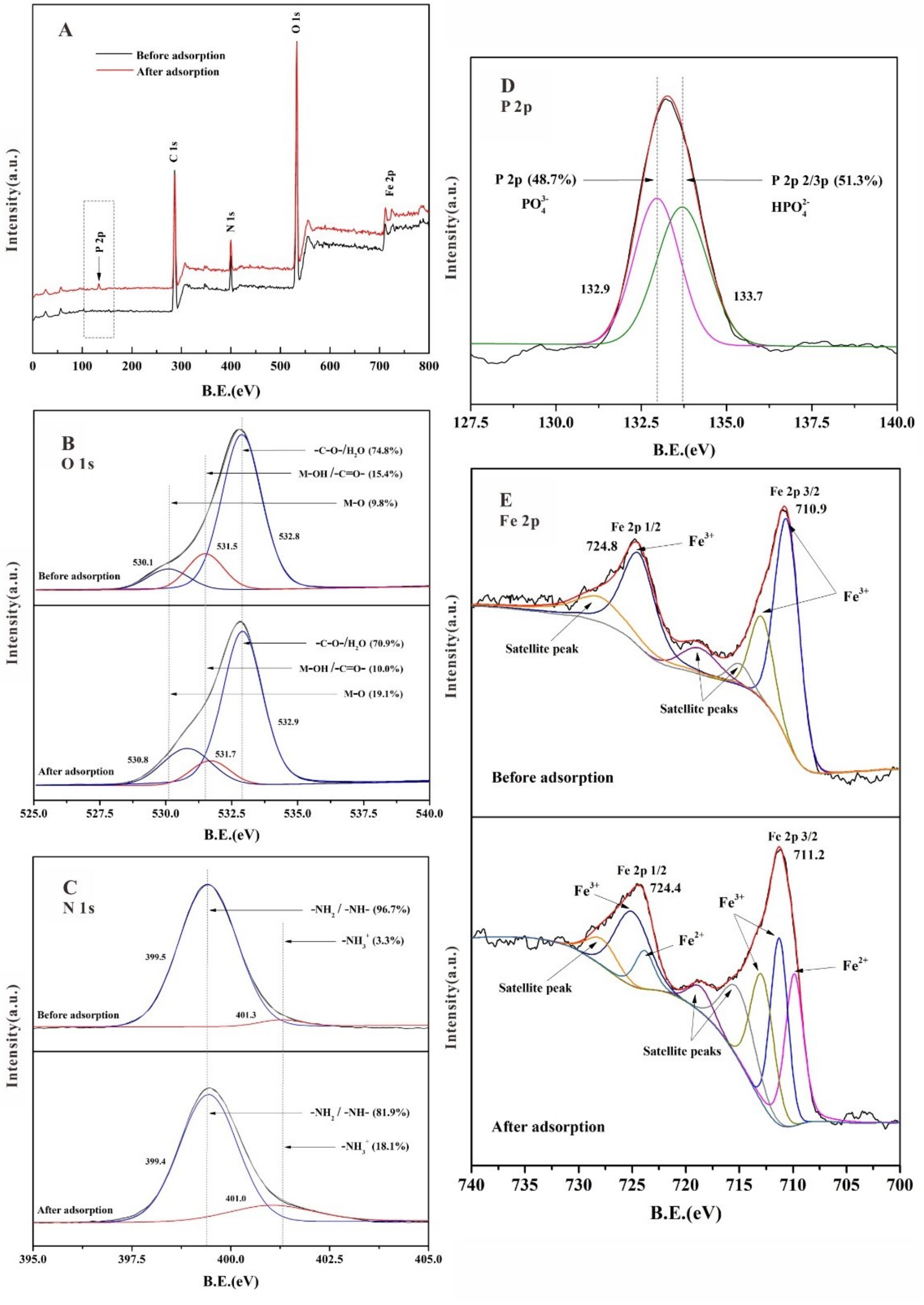

Fig. 3-6 XPS spectra of wide scan (A), O 1s (B), N 1s (C), P 2p (D), and Fe 2p (E) for the CTS-Fe before and after the AD process.

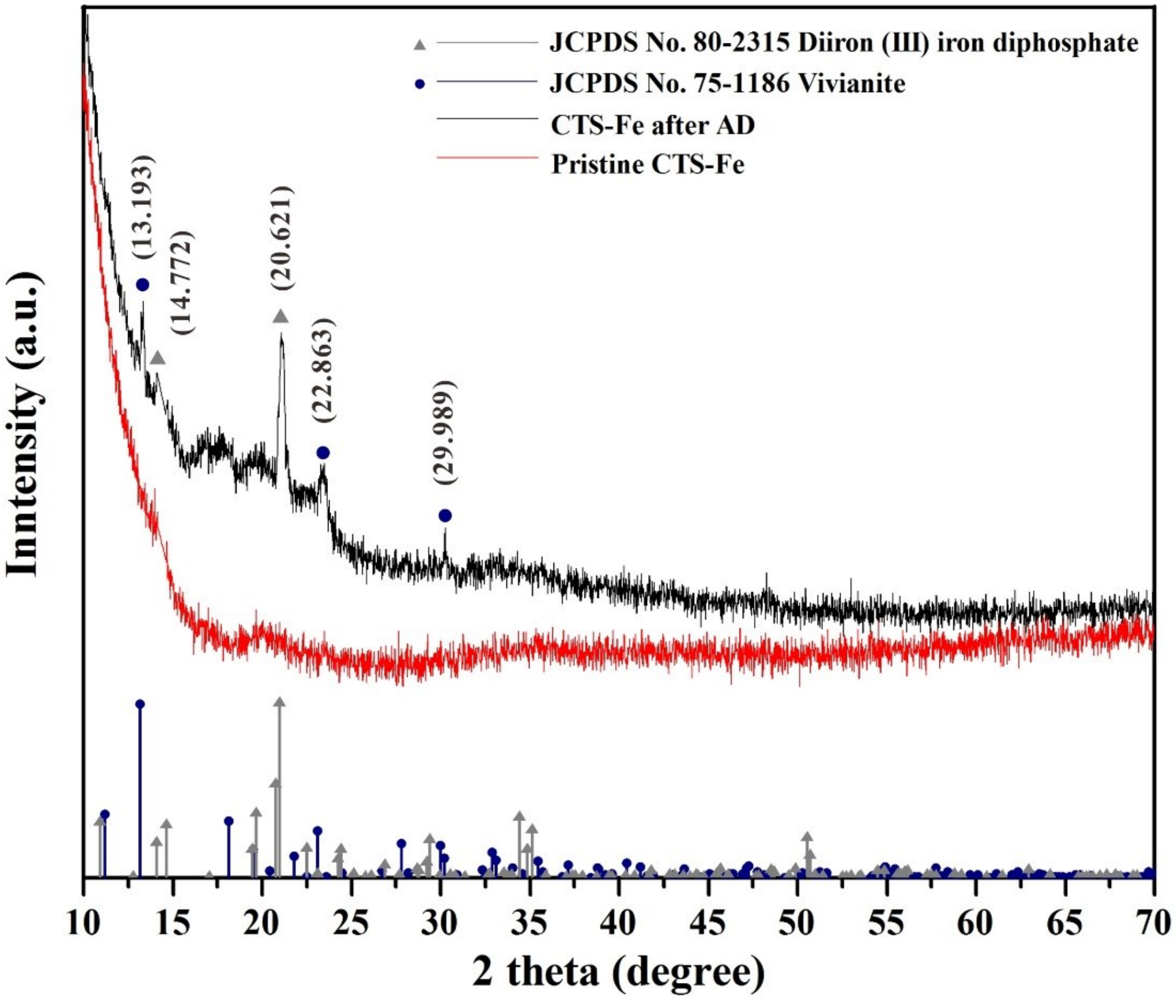

Fig. 3-7 XRD spectra of CTS-Fe before and after the AD process.

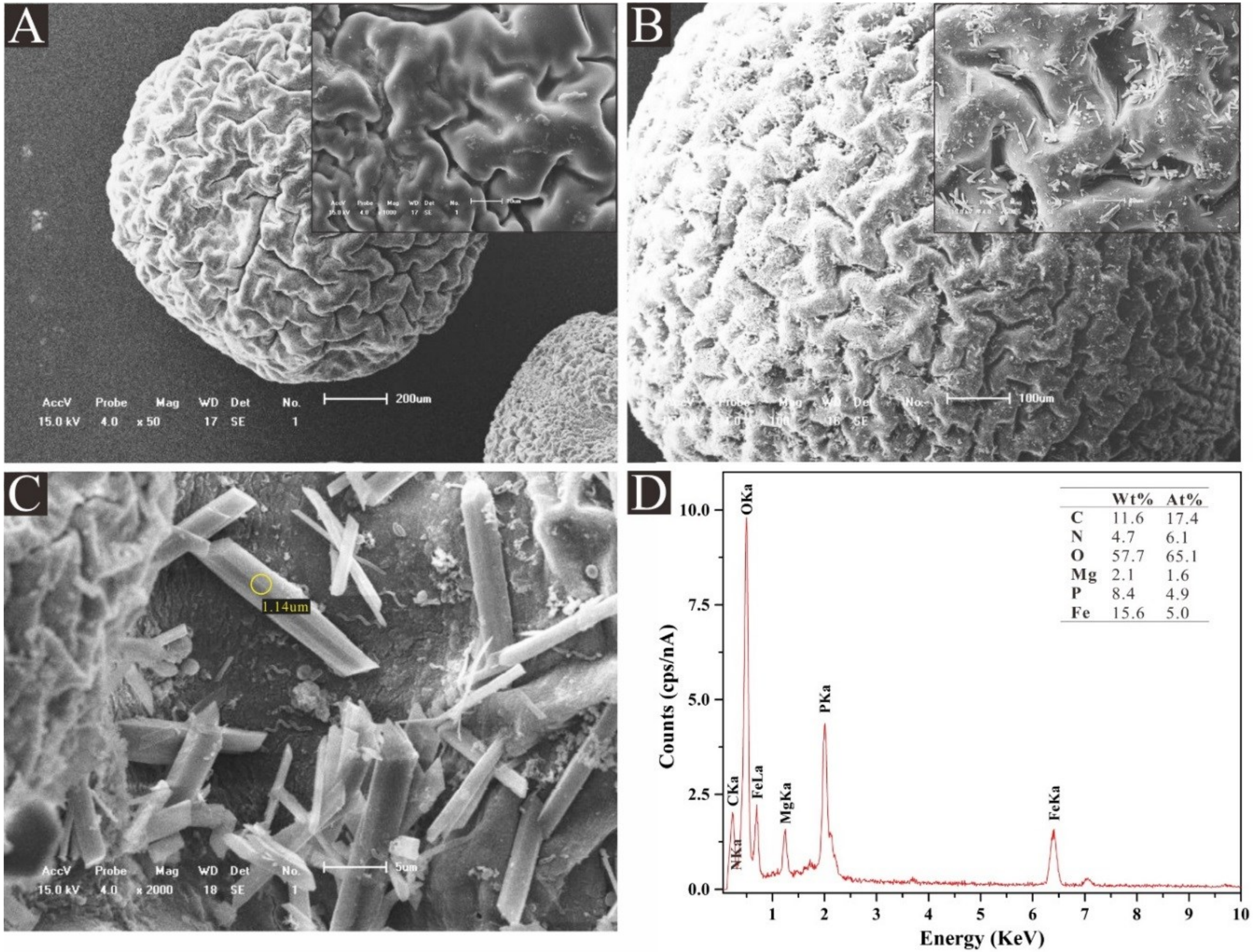

Fig. 3-8 SEM images of CTS-Fe surface before (A) and after (B, C) the AD process, and EDS pattern of the crystals formed (D).

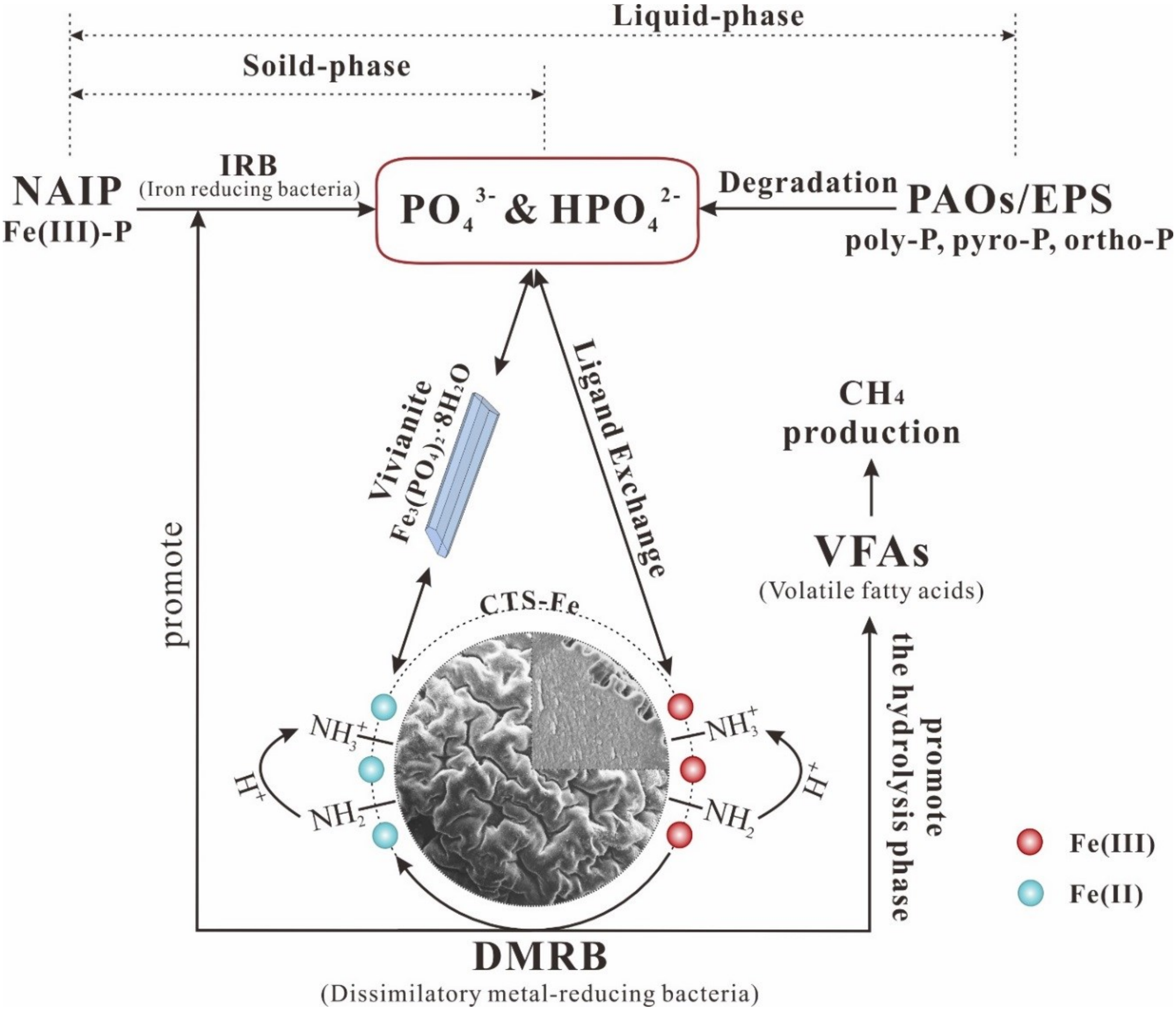

Fig. 3-9 Scheme for the mechanisms involved in the CTS-Fe supplemented AD process.

Chapter 4 Mechanisms analysis of enhanced AD of WAS by Chitosan-Fe addition

4.1 Introduction

As mentioned in Chapter 3, it was confirmed that CTS-Fe has great potential for enhancing methane production from WAS during AD process. Additionally, previous studies have indicated that addition of Fe to WAS could improve the AD performance through different pathways. The major pathway of promotion is concentrated in the hydrolysis and methanogenesis steps of AD. Fe oxides could enrich Fe (III)-reducing microorganisms, which accelerate the decomposition of complex matters via the DIR and significantly promote methane production (Baek et al., 2014; Kim et al., 2014; Tan et al., 2015). Furthermore, Fe (III) oxides may act as conductive materials that connected to the electron transfer between organic-oxidizing bacteria and methanogens, thereby promoting methanogenesis process via DIET (Lu et al., 2019; Wang et al., 2018c; Zhuang et al., 2015). However, several earlier reports have proposed the opposite result that the inhibition of methane production by the addition of Fe (III) in the AD system (Lovley & Klug, 1983; Zhang et al., 2009b). Although the effect of Fe on methane generation during AD process is controversial, previous research in this work has confirmed that CTS-Fe could effectively promote methane production during AD of WAS. However, the information on the potential mechanism was still limited.

This work investigated the potential mechanisms for the enhance methane production due to CTS-Fe addition, which was carried out by examing the influences of CTS-Fe on the hydrolysis and methanogenesis steps involved in AD of WAS. Furthermore, the archaeal and bacterial communities were also analyzed in this work.

4.2 Materials and methods

4.2.1 Material synthesis and preparation

The CTS-Fe composite material used in the experiment is the same as that in Chapter 3. For the detailed synthesis process, please refer to section 3.2.1.

WAS and digested sludge used as the substrate and inoculant sludge in this study were collected from a domestic WWTP in Ibaraki (Japan) and stored at 4°C before digestion. To acclimatize the digested sludge for use in batch experiment, the digested sludge was operated in a batch AD reactor at 35.0 ± 2.0 °C for one month.

4.2.2 Influence of CTS-Fe on the whole AD process

Batch AD experiments were carried out in 100 mL glass serum bottles. The mixture sludge was contained WAS and the inoculums in a ratio of 9:1 (v/v) with a total volume of 80 mL.

The main characteristics (mean ± standard deviation) of the mixture is shown in Table 4-1. To assess the effects of different CTS-Fe dosage on the AD of WAS, four sets of batch experiments were set up: 5, 10, 20 g/L CTS-Fe added and a CTS-Fe free digester (i.e., control). Before anaerobic experiments, the initial pH of the mixture was adjusted to 7.4 using 1 M HCl or NaOH. All bottles were sealed with rubber stoppers. Next, nitrogen gas was flushed into the bottles for 3 min to remove any oxygen and then incubated at 35 ± 2°C for 28 days. After AD process, the digestate was collected to determine the related parameters.

4.2.3 Influence of CTS-Fe on hydrolysis and methanogenesis

(1) Hydrolysis step

To investigate the effect of CTS-Fe on the hydrolysis and methanogenesis steps involved in the AD process, a higher dosage of CTS-Fe (10 and 20 g/L) were used for testing. To eliminate the influence of methanogens on hydrolysis the methanogenesis inhibitor sodium 2-bromoethanesulfonic (2-BES) (5 mM) was added into the digesters. The influence of hydrolysis of WAS was studied by examining the hydrolysis efficiency of soluble organic matters in the sludge, and the relative activity of extracellular hydrolases were measured on day 6.

(2) Methanogenesis step

It is well known that the conversion of acetic acid (HAc) and H_2 / CO_2 into methane under the action of acetoclastic and hydrogenotrophic methanogens are the main two methane generation pathways.

To identify the effect of CTS-Fe on acetoclastic methanogens, synthetic VFAs were used instead of WAS as the substrate for methane to generate methane. The concentration of HAc was dominated in synthetic VFA accounting for 49% of the total VFAs (1477.7 mg-C/L). The inoculum was added to synthetic VFAs with a final volume 80 ml, and CTS-Fe was added at dose of 0, 10 and 20 g/L. In the study of the effect of CTS-Fe on hydrogenotrophic methanogens, hydrogen and carbon dioxide in a ratio of 4:1 (v/v, 200 kpa) added as the substrate for the hydrogenotrophic test, and CTS-Fe was added at dosage of 10 g/L.

4.2.4 Analytical methods

(1) General indices

The determinations relating to sludge samples (total solids (TS), volatile solids (VS) and pH), biogas products (CH_4, H_2 and CO_2) and volatile fatty acids (VFAs) using the same methods as described previously (Chapter 3, section 3.2).

Soluble total organic carbon (STOC) was determined by a total carbon analyzer (TOC-VCSN, ASI-V autosampler, Shimadzu, Japan). Soluble polysaccharides and protein in the EPS were quantified with the phenol-sulfuric acid method and Lowry's method, respectively. The concentrations of Fe^{2+} and Fe^{3+} were measured with 1,10-phenanthroline following the standard method (APHA, 2012) using a UV-visible spectrophotometer (UV-1800, Shimadzu, Japan).

(2) Enzymes assays

To evaluate the effect of CTS-Fe on hydrogenotrophic methanogenesis, the activities of coenzyme F_{420} was examined in the experiments. Extraction of coenzyme F_{420} was assayed according to the description by (Dong et al., 2019) with a modification as follows. Digestion mixture (20 mL) was centrifuged (6000 rpm/min, 15 min, 4°C), and washed for three times by NaCl buffer (0.9%). The pellet was then suspended in 30 ml deionized water and the cells disrupted by heating in a boiling water bath for 30 min and centrifuged to remove supernatant. Afterward, the pellet was mixed with ethanol which is 3-folds volume of pellet, and centrifuged to remove pellet. Finally, the supernatant was adjusted pH to 13.5 and measured by a UV-visible spectrophotometer at 420 nm. To indicate the effect of CTS-Fe on hydrolysis efficiency during AD, the activities of four main extracellular hydrolases, ALP, ACP, α-glucosidase and protease were determined according to the literatures (Yuan et al., 2017), the detail determination information was shown in Table 4-2.

(3) Microbial community analysis

To analyze microbial communities 16S rDNA gene sequencing was performed. Total DNA was extracted from sludge samples (day 28) using a FastDNA® SPIN Kit (Qiagen, CA, USA), the purity and concentration were detected by using NanoPhotometer spectrophotometer and Qubit 2.0 Fluorometer. Fragments of 16S rDNA were amplified with polymerase chain reaction (PCR) using the bacterial primers set to 338F (5′-ACTCCTACGGGAGGCAGCA-3′)/ 806R (5′-GGACTACHVGGGTWTCTAAT-3′), and the archaeal primers set to Arch349F (5′-GYGCASCAGKCGMGAAW-3′)/ Arch806R (5-GGACTACVSGGGTATCTAAT-3′). The sequencing was performed using Illumina Hiseq platform.

4.2.5 Calculations and kinetics

To better understand the effect of CTS-Fe addition on methane generation under different conditions, the experiment data from the batch test were fitted to the modified Gompertz equation (as seen in section 3.2.4 for details (Eq. 3-1)).

Coenzyme F_{420} concentration was calculated by Eqs. (4-1).

$$C_{F420} = \frac{A_{420} \times f}{\varepsilon \times L \times V} \tag{4-1}$$

where C_{F420} is the content of coenzyme F_{420} per unit mass of sludge (μmol/g-VS); A_{420} is the absorbance at 420 nm; f is the dilution factor for sample; L is the cuvette thickness (cm); ε is the extinction coefficient of coenzyme F_{420} at pH 13.5 (ε = 54.3, L/(cm·μmol); and V is the VS of sludge (g/L).

4.2.6 Statistical analysis

All experiments and sample analysis were conducted in triplicate. The data presented in the results and discussion are average values. For data analysis, one-way analysis of variance (ANOVA) was applied to analyze statistical difference in the experimental data using Microsoft Office Excel 2016. Origin 9.0 was used to fit the kinetic model.

4.3 Results and discussion

4.3.1 Influence of CTS-Fe on AD of WAS

The effects of CTS-Fe addition on cumulative methane yield and daily methane production from WAS are illustrated in Figs. 4-1A and B, respectively. After 28 days, the accumulative methane yields in CTS-Fe added (5.0-20.0 g/L) reactor reached 201.2, 212.7 and 225.6 mL/g-VS, respectively (Fig. 4-1A). The methane production of the CTS-Fe added reactor was increased by 8.0-21.1% compared with the control reactor (186.3 mL/g-VS). As shown in Fig. 4-1B, compared with that in Rc (36.0 mL/g-VS·d) on day 8, a higher daily methane production peak (46.1 mL/g-VS·d) was detected on day 10 in the CTS-Fe addition reactor (20 g/L).

The modified Gompertz model was used to fit the data to make clear the effect of CTS-Fe on methane production from WAS of AD (Table 4-3A). The correlation coefficients (R^2 = 0.997-0.999) suggest the good fitness of the Gompertz models to the experimental data, and the predicted results were almost consistent with the experimental results. Compared to the control reactor, the reactors with CTS-Fe addition showed higher methane production potential (P_{max}, 8% - 23% increase) and faster methane production rate (R_{max}, 13% - 34% increase) under the CTS-Fe addition, and these results agree with the results in Chapter 3. However, the lag time for methane production was extended by 2.8-fold when 20 g/L of CTS-Fe was supplemented. This may be due to the inoculation of the digested sludge in this chapter, thereby enhancing the activity of methanogens. In accordance with the methane production results, CTS-Fe enhanced the organic matter reduction rate, as shown in Table 4-4, the VS reductions in the CTS-Fe reactors were increased by about 1.09-1.19 times that in the control (28.0%). These results indicated that CTS-Fe can significantly enhance the methane production from WAS of AD. Moreover, the release of Fe^{2+} indicated that DIR process had occurred in this work, and the concentration of Fe^{2+} in CTS-Fe added reactors were significantly higher than those in control reactor at end of the experiment (Fig. 4-1C).

4.3.2 Effect of CTS-Fe on the hydrolysis process

The organic matters in WAS are mainly embedded in microbial cells or immobilized in EPS, and the structure and integrity of sludge generally determined by EPS (Shi et al., 2017). Proteins and polysaccharides are the major components of EPS, and the decomposition of these two constituents were used to assess the hydrolysis of WAS.

To eliminate the influence of methanogens on hydrolysis, the methanogenesis inhibitor sodium 2-bromoethanesulfonate (2-BES) was added to the experiment. As shown in Fig. 4-2A, the addition of CTS-Fe has effectively promoted the degradation of proteins and polysaccharides during the hydrolysis process. After six days of digestion, the concentration of soluble proteins and polysaccharides in the reactor with CTS-Fe added (20 g/L) were reduced by 423.8 and 114.6 mg/L, respectively, which was more than 1.5 times as high as the control group (264.3 and 83.6 mg/L, respectively).

In addition, the activities of four main extracellular hydrolases in this study, ALP, ACP, α-glucosidase and protease, were determined to indicate the hydrolysis efficiency during AD. Among them, protease and α-glucosidase are respectively responsible for converting proteins and polysaccharides into amino acids and monosaccharides in the hydrolysis reaction, which could be further converted into VFA, and finally used by methanogens to produce methane. The activity of these enzymes was measured on the sixth day (Fig. 4-2B), which is consistent with the degradation of organic matters. Compared with the control group, the activities of protease and α-glucosidase in the reactor with CTS-Fe added (20 g/L) were increased by 24.2% and 39.7%, respectively. And the hydrolase activity increased with the increase of CTS-Fe dosage.

As for VFAs (Fig. 4-2C), the total VFAs concentration in CTS-Fe added group (20 g/L, 1955.2 mg-C/L) was 18.5% higher than that of the control group (1650.2 mg-C/L). Notably, the concentrations of Acetic and Propionic in the CTS-Fe group were both higher than those in the control group. It is speculated that the addition of CTS-Fe can also improve acidification during the AD process, thereby increasing the production of VFAs. STOC in the supernatant represented the soluble organics. It can be seen from Fig. 4-2D that STOC in the CTS-Fe reactors were significantly higher by 19.4% - 30.9% compared with the control at day six. These results indicated that CTS-Fe enhances the hydrolysis process of WAS without the involvement of methanogens.

4.3.3 Effect of CTS-Fe on the methanogenesis process

(1) VFA as substrate

Conventionally, as the two main types of methane producers, acetoclastic and hydrogenotrophic methanogens could respectively lead acetate and H_2 / CO_2 converted to methane (Xu et al., 2010). Wherein the metabolism of acetate could produce nearly 70% of methane during the AD process. In this study, VFA synthetic wastewater was used to investigate the effects of CTS-Fe on acetoclastic methanogenesis.

During 28 days digestion, an inhibitory effect on methane production from acetoclastic metabolism by CTS-Fe addition was shown in Fig. 4-3A. In detail, the accumulation of methane in the control group reached equilibrium on the 16th day and maintained at 234.1 mL/g-COD until the end of the experiment. Corresponding to the variation of VFA (Fig. 4-3B), no VFA was detected in the control group after 16 days. However, the methane generation in the reactor with CTS-Fe did not reach equilibrium until around 28 days (220.8-229.2 mL/g-COD) and lower than the reactor without CTS-Fe. According to the model fitting results (Table 4-3B) the methane production rate and the lag time for methane production in the CTS-Fe groups were reduced by 42% - 62% and extended by nearly doubled, respectively, compared to those in the control group. These results mean that CTS-Fe had a slight inhibitory effect on the acetoclastic methanogenesis.

(2) H_2 / CO_2 as substrate

Hydrogen and carbon dioxide (80%: 20%, v/v) added as the substrate for methanogens to investigate the effect of CTS-Fe on the hydrogenotrophic test. The results showed that the CTS-Fe also had an inhibitory effect on hydrogenotrophic methanogenesis. The consumption of hydrogen in the control reactor was faster than that in the CTS-Fe supplemented reactor (10 g/L), and the accumulation of methane after 5 days of digestion was 26.2% higher than that in CTS-Fe group (Fig. 4-4A and B). Coenzyme F_{420} is a critical enzyme during the reduction of CO_2 to CH_4, which was used to identify the efficiency of hydrogenotrophic methanogenesis (Liu et al., 2017; Reynolds & Colleran, 1987). From Fig. 4-4C the coenzyme F_{420} contents both in control and CTS-Fe addition groups were increased by at the end of digestion. However, the coenzyme F_{420} contents in the control reactor was 34.9% higher than CTS-Fe supplemented, which means that CTS-Fe inhibited the activity of coenzyme F_{420}, hence limiting the process of hydrogenotrophic methanogenesis.

4.3.4 Microbial community analysis

(1) Bacterial community

The changes in the abundance of bacterial community composition in each reactor were analyzed in this study. The Proteobacteria (28.3%), Bacteroidetes (26.3%), and Firmicutes (12.0%) were the major bacterial phyla of the raw mixture sludge, which are common hydrolytic and acidogenetic bacteria (Fig. 4-5A). After AD process, the bacterial community composition changed, the scale of Proteobacteria decreased significantly, with the other abundance of bacterial phyla increased. Additionally, the major bacterial phyla in the CTS-Fe supplementation reactors were higher than those in the control reactor.

Notably, the abundance of Firmicutes was enhanced with the increase of CTS-Fe dosage. As previously reported, most members of the Firmicutes phylum plays a crucial role in the hydrolysis and acidification during the AD process, which can produce extracellular enzymes and then relate to the degradation of organic compounds and the constitution of VFAs (Li et al., 2015b). As shown in Figure 4-5B, within the Firmicutes phylum, the class Clostridia abundance in the 20 g/L CTS-Fe added reactor (13.8%), 1.8 folds higher than that observed in the control reactor (7.9%). Zhao et al. (2018a) reported that the predominance of Clostridia was associated with a high-rate of hydrolysis. It means that CTS-Fe added could improve the hydrolysis efficiency of WAS, which is consistent with the conclusion in section 4.3.2. Furthermore, Bacteroidia and Anaerolineae are the major class within the Bacteroidetes and Chloroflex phylum, respectively. It was observed that the abundance of these classes in the reactor with CTS-Fe was higher than that of the control reactor. Similar to the class Clostridia, members of this class were responsible for hydrolysis and degrade organic matters played a significant role in sludge reduction (Tan et al., 2010; Xia et al., 2016). Therefore, the analysis of bacterial phyla demonstrated that the CTS-Fe addition might promote the enrichment of hydrolytic bacteria in the AD reactors, further enhanced the hydrolysis of organic matter resulting in improved methane production.

(2) Archaeal community

Analyzed archaeal sequences of the raw sludge were mostly affiliated with the phylum Euryarchaeota (78.1%), and Crenarchaeota (21.9%).

As shown in Fig. 4-5A, Methanosarcinales (59.5%), Methanomicrobiales (13.5%), Methanobacteriales (2.8%), and Methanomassiliicoccales (2.3%) were the major archaeal orders in the phylum Euryarchaeota, which was related to the acetoclastic and hydrogenotrophic methanogenesis. Vanwonterghem et al. (2016) reported that Methanomethyliale in phylum Crenarchaeotas is inferred to be capable of methylotrophic methanogenesis. Similar to the changes observed in bacterial community composition, the archaeal community composition was changed significantly after digestion. The abundance of order Methanomethyliale was decreased by around 10 times both in all reactors, while the abundance of Methanosarcinales was crucially increased to over 90% (92.2%-93.9%). The order Methanosarcinales (with the predomination of the genera *Methanosarcina* and *Methanosaeta*) is acetate-utilizing representative within Methanogenic archaea (Ziganshin et al., 2016). This trend revealed that acetoclastic methanogenesis was the dominant methane generation process during the present AD. Additionally, the changes in abundances of order Methanomicrobiales after digestion was noticeable. Methanomicrobiales has been validly published to the genera *Methanolinea* (Imachi et al., 2008), *Methanosphaerula* (Cadillo-Quiroz et al., 2009), and *Methanoregula* (Yashiro et al., 2011), which were highly affiliated with the hydrogenotrophic methanogenesis (Browne et al., 2017). It was observed that a lower abundance of Methanomicrobiales was detected in the reactors after digestion (1.1%-3.7%) than that in the inoculum. This occurrence revealed that the methanogenesis drove by hydrogenotrophic was significantly weaker than acetoclastic in present study. It is worthwhile to note that *Methanolinea* abundance in the control group (1.7%) was 0.2% - 1.3% higher than that in the CTS-Fe groups with the increase of the CTS-Fe dosage, indicating inhibition of the hydrogenotrophic pathway of methanogenesis by CTS-Fe supplementation. A similar result was observed in the genus *Methanoculleus*, which abundance in 20 g/L CTS-Fe added reactor was 7.5 times lower than that in the reactor without CTS-Fe supplementation. *Methanoculleus* is also a major contributor to methane generation and that the hydrogenotrophic pathway predominated during methanogenesis, which assimilated carbon from acetate and catabolized acetate-derived H_2 and CO_2 (Barret et al., 2013; Lu et al., 2019). This observation further verifies the conclusions in section 4.3.3.

4.3.5 The mechanisms underlying AD response to CTS-Fe addition

To reveal the underlying mechanism of this study, the hydrolysis and methanogenesis steps involved in AD were further analyzed in combination with the microbial bacterial community changes. As described in 4.3.1, the results from the whole AD process confirmed that CTS-Fe significantly promoted AD of WAS. Compared with the control reactor, the methane production increased by 8.0% - 21.1%, and the VS reduction rate increased by 1.09-1.19 times within the CTS-Fe reactors.

In previous studies, the potential mechanisms of Fe enhancing AD of WAS were reported as follows: (1) promote the activities of hydrolases; (2) enrich the microorganisms that reduce Fe (III), and stimulate the decomposition of complex organics via DIR process; (3) accelerate DIET process. The results of the hydrolysis experiment in this work showed that CTS-Fe significantly enhanced the activities of the hydrolases, corresponding to the degradation rate of protein and polysaccharide has also been improved. Furthermore, the bacterial community results demonstrated that the bacterial associated with hydrolysis included class Anaerolineae and Bacteroidia, their relative abundance in the CTS-Fe reactors were higher than those of the control reactor.

It is worth noting that Clostridia and Synergistia belonged to IRB were significantly enriched in the microbial communities with CTS-Fe addition, and the higher amount of release of Fe^{2+} in CTS-Fe added reactors (Fig. 4-1C) (Peng et al., 2018). These results indicated that the potential mechanisms of CTS-Fe promoted the hydrolysis process was mainly contributed to be via DIR, which is in agreement with previous studies. Previous reports pointed out that Fe (III) oxide can act as electron acceptor to oxidize organic matters in the process of DIR (Kato et al., 2010). Most IRB could transfer electrons from metabolizing organic matters to insoluble Fe (III) oxides, thereby with the reduction of Fe (III) to Fe (II) (Baek et al., 2015; Zhao et al., 2016). In other words, due to the enrichment of IRB in the process of DIR, electron transfer in oxidized organic matter and insoluble Fe (III) oxide could accelerate the destruction of cell walls (Peng et al., 2018).

In section 4.3.3, the methanogenesis process was significantly inhibited with the presence of CTS-Fe. It is well known that both the hydrogenotrophic and acetoclastic methanogenesis ultimately produce methane through the reduction of $CH_3 \cdot S \cdot CoM$ (Zhao et al., 2018b). However, Fe (III) as an electron acceptor would compete with $CH_3 \cdot S \cdot CoM$ for electrons, thereby limiting methanogenesis. Previously reported that H_2 and organic matter can be used as an electron donor for microbial Fe (III) reduction (Li et al., 2017). The lack of organic matters in the hydrogenotrophic experiment makes hydrogen as the main electron donor for the DIR process, accordingly limiting the process of reducing CO_2 to CH_4, which could explain why inequality between H_2 / CO_2 consumption and methane production was observed in CTS-Fe reactors (see section 4.3.3). Besides, the lower coenzyme F_{420} activity in the CTS-Fe reactor also proved this result.

Methanosaeta was the dominant genus within Methanosarcinales order, which is the most active methanogens utilizing acetate to form CH_4. Other studies have shown that this genus also has the ability to reduce carbon dioxide into methane through DIET with syntrophic bacteria (Cruz Viggi et al., 2014; Rotaru et al., 2014; Zhao et al., 2017b), based on the following reaction:

$$CO_2 + 8H^+ + 8e^- \rightarrow CH_4 + 2H_2O \qquad (4\text{-}3)$$

After supplementation with CTS-Fe, the abundance of *Methanosaeta* was slightly higher than that in the control reactor (see Section 4.3.4 above). Thus, it was speculate the CTS-Fe has the potential to stimulate DIET. However, this mechanism is unlikely responsible for the positive effect observed in this study, caused by hydrogenotrophic was not the main route of methanogenesis in the present study.

4.4 Summary

This work systematically illuminated the potential mechanisms for the enhancement of

WAS digestion by CTS-Fe supplementation. Microbial communities confirmed that IRB enriched in the CTS-Fe added reactors, indicating that CTS-Fe had the ability to accelerate the hydrolysis process through the DIR providing abundant substrates for methanogenesis. However, the methanogenesis tests showed that CTS-Fe as an electron acceptor would compete for electrons with methanogens, thereby inhibiting acetoclastic and hydrogenotrophic methanogenesis. The microorganisms involved in hydrogenotrophic methanogenesis were decreased in the CTS-Fe added reactors also proved this result. On the other hand, DIET was not the major pathway of promoting methanogenesis, due to hydrogenotrophic was weaker than acetoclastic in present study. The mechanisms revealed herein provide theoretical support for the CTS-Fe used in practical AD applications.

Table 4-1 Main characteristics of mixture sludge used in this work.

Parameters	Unit	Mixture sludge
Total solids (TS)	%	2.29 ± 0.01
Volatile solids (VS)	%	1.77 ± 0.02
Soluble total organic carbon (STOC)	mg/L	1295.42 ± 9.26
Soluble proteins	mg/L	612.60 ± 5.12
Soluble polysaccharides	mg/L	142.05 ± 2.54
Volatile fatty acids (VFAs)	mg-C/L	602.86 ± 15.27

ND, not determined.

All data were expressed as mean ± SD of triplicate tests.

Table 4-2 Detection conditions for hydrolase activities measurement in this study.

Enzyme	Substrate	Reaction system	wavelength
Alkaline phosphatase (ALP)	0.1% *p*-nitrophenyl phosphate disodium salt (pnpP)	2 ml 0.2 M Na_2CO_3-$NaHCO_3$ buffer, pH 9.6 1 ml substrate 1 ml sample 55℃, 30 min, 2 ml 1 M NaOH termination.	410 nm
Acid phosphatase (ACP)	0.1% *p*-nitrophenyl phosphate disodium salt (pnpP)	2 ml 0.2 M HAc-NaAc buffer, pH 4.8 1 ml substrate 1 ml sample 55℃, 30 min, 2 ml 1M NaOH termination.	410 nm
α-Glycosidase	0.1% *p*-nitrophenyl-a-D-glucopyranoside (pnpG)	2ml 0.2 M $NaHPO_4$-NaH_2PO_3 buffer, pH 7.5 1 ml substrate 1 ml sample 55℃, 30 min, 4 ml 0.4M Na_2CO_3 termination.	410 nm
Protease	10 mg/ml Casein	a. 1ml substrate+1 ml sample, 55℃, 10 min, 2 ml 0.4 M TCA termination, filter. b. 1 ml filtrate+5 ml 0.4M Na_2CO_3+1 ml Folin-phenol, 40℃, 20 min	640 nm

Table 4-3 The relevant parameters obtained by fitting the modified Gompertz model to the various experimental data.

A: The test of the whole AD process

CST-Fe addition	**Cumulative CH_4 yield from AD test**	**Kinetic parameters**			
(g/L)	**(mL/g-VS)**	P_{max} **(mL/g-VS)**	R_{max} **(mL/g-VS·d)**	λ **(d)**	R^2
0	186.3	186.4	15.11	1.43	0.998
5	201.2	201.8	17.10	1.99	0.999
10	212.7	216.7	17.66	2.69	0.997
20	225.6	229.9	20.18	3.96	0.997

B: The test of methanogenesis process (VFA as substrate)

(g/L)	**(mL/g-COD)**	**(mL/g-COD)**	**(mL/g-COD·d)**	**(d)**	
0	234.1	236.5	32.02	1.65	0.998
10	229.2	236.9	18.57	2.83	0.996
20	220.8	256.4	12.11	3.37	0.996

Table 4-4 Total solids (TS) and volatile solids (VS) reduction in the different reactors after 28 days' experiments.

	Raw	**Rc**	**R1**	**R2**	**R3**
TS (%)	2.29	1.80	1.69	1.72	1.67
VS (%)	1.77	1.28	1.23	1.19	1.18
VS reduction (%)	-	28.0	30.6	32.7	33.2

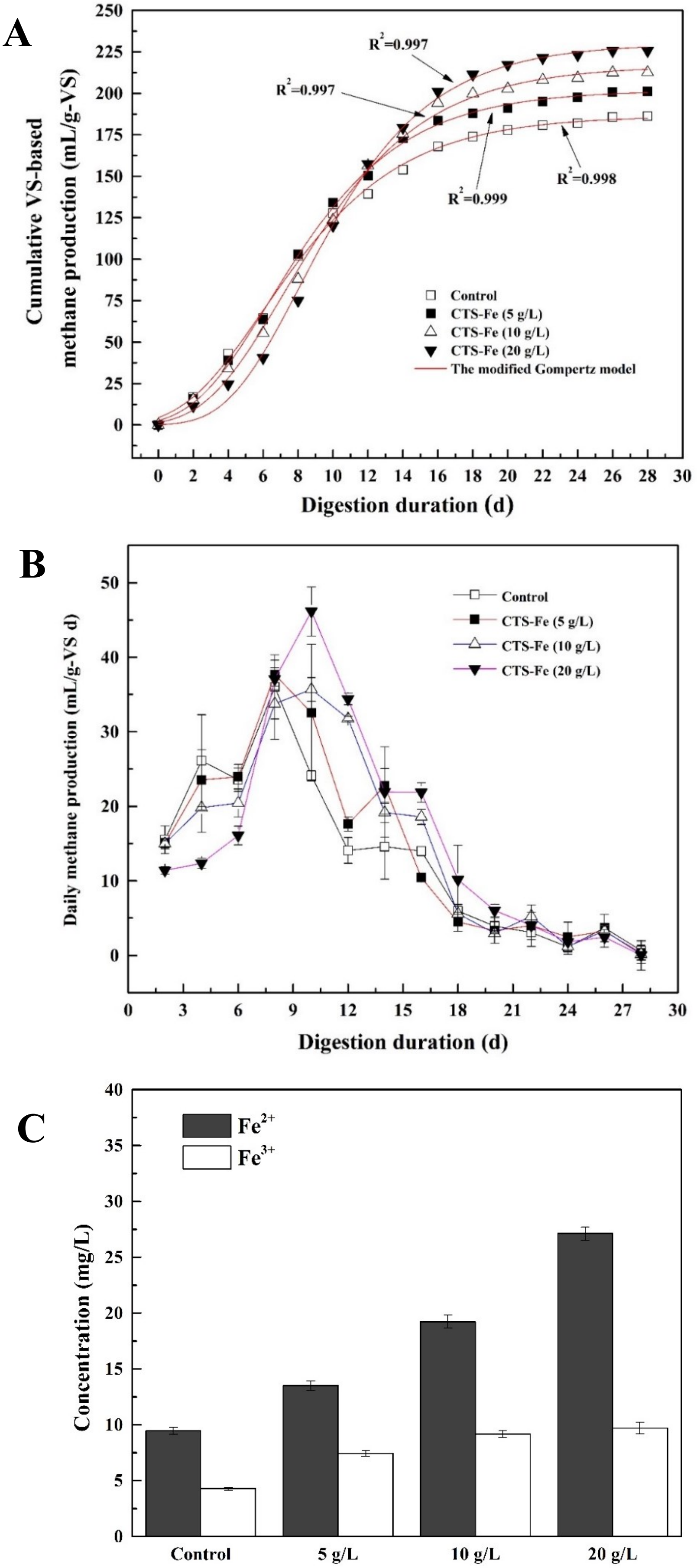

Fig. 4-1 Cumulative methane yield (A), daily methane production (B) and concentration of Fe^{2+} / Fe^{3+} from WAS under different dosages of CTS-Fe.

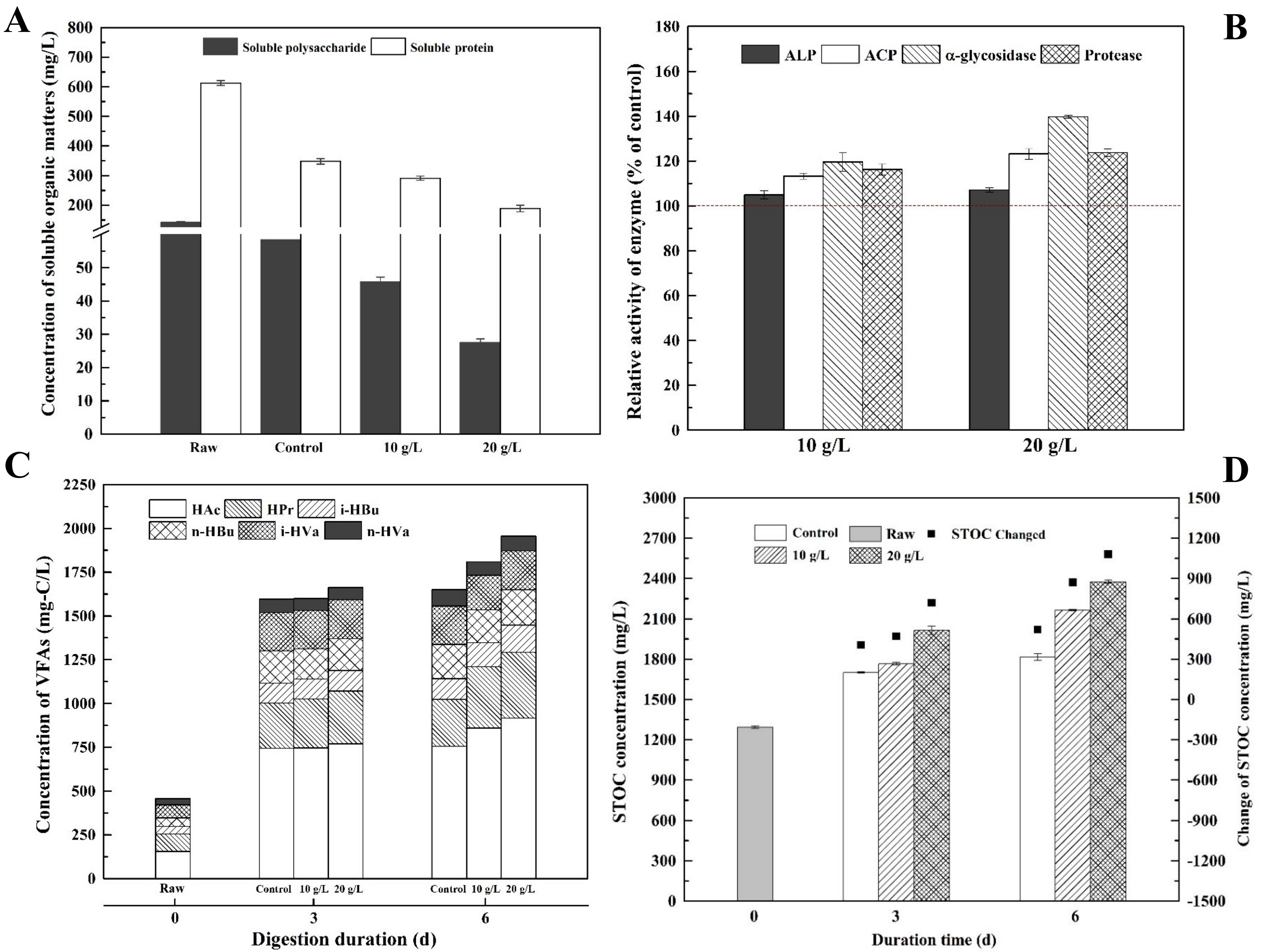

Fig. 4-2 Variation of soluble proteins and polysaccharides (A), hydrolase (B), cumulative VFAs (C) and soluble TOC (D) in the sludge before and after AD for 6 days with the addition of methanogen inhibitor.

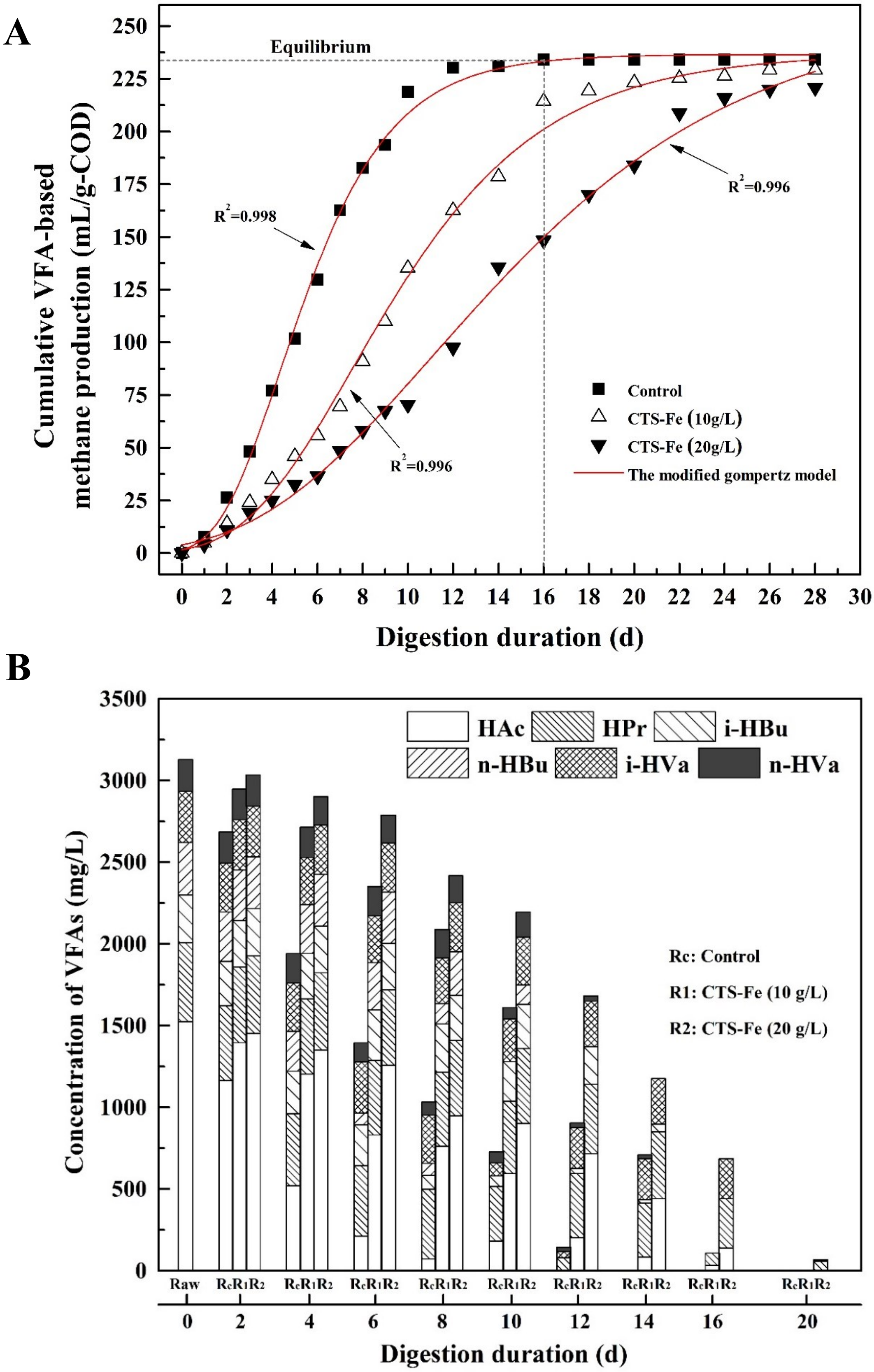

Fig. 4-3 Methane yield (A) and the changes of VFAs compositions (B) during the acetoclastic methanogenesis process.

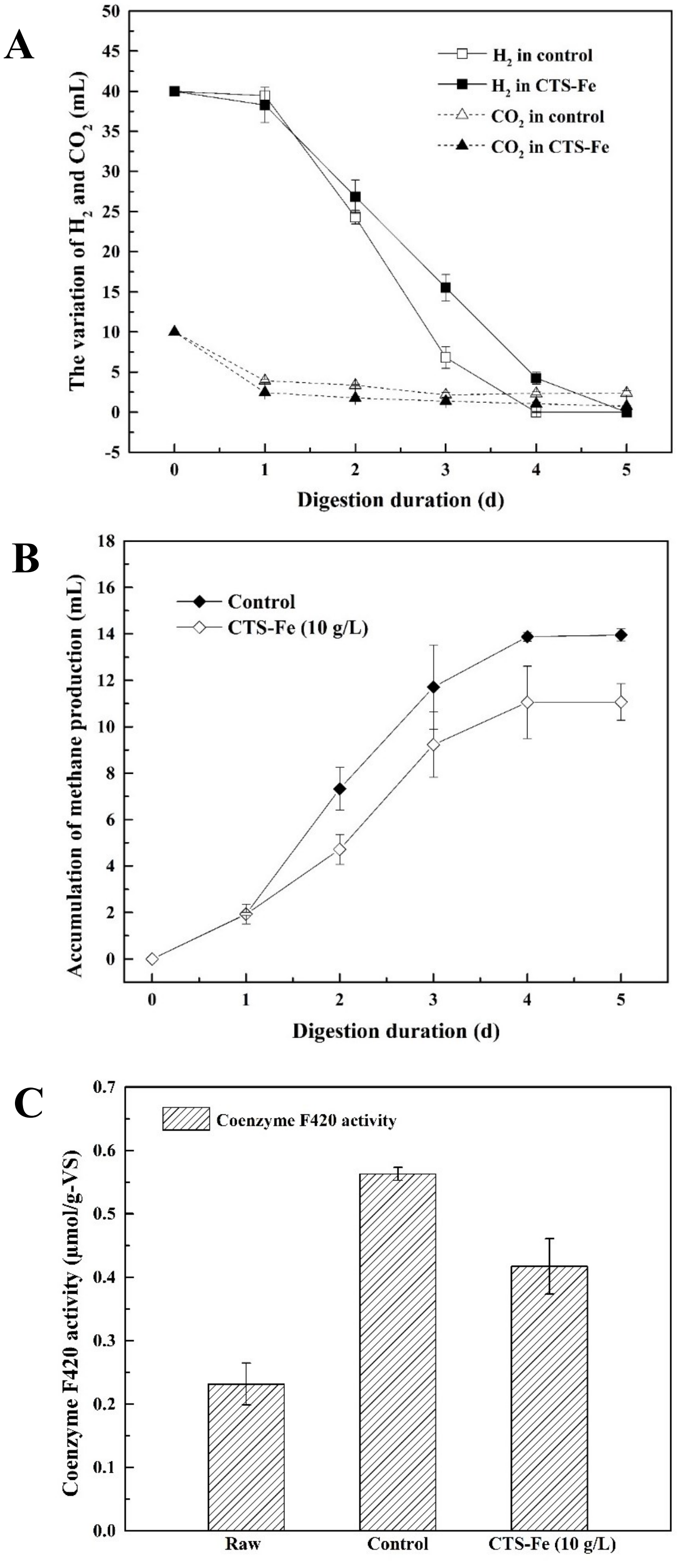

Fig. 4-4 Variation of H_2 / CO_2 (A), Methane yield (B) and the activity of coenzyme F_{420} (C) during the hydrogenotrophic methanogenesis process.

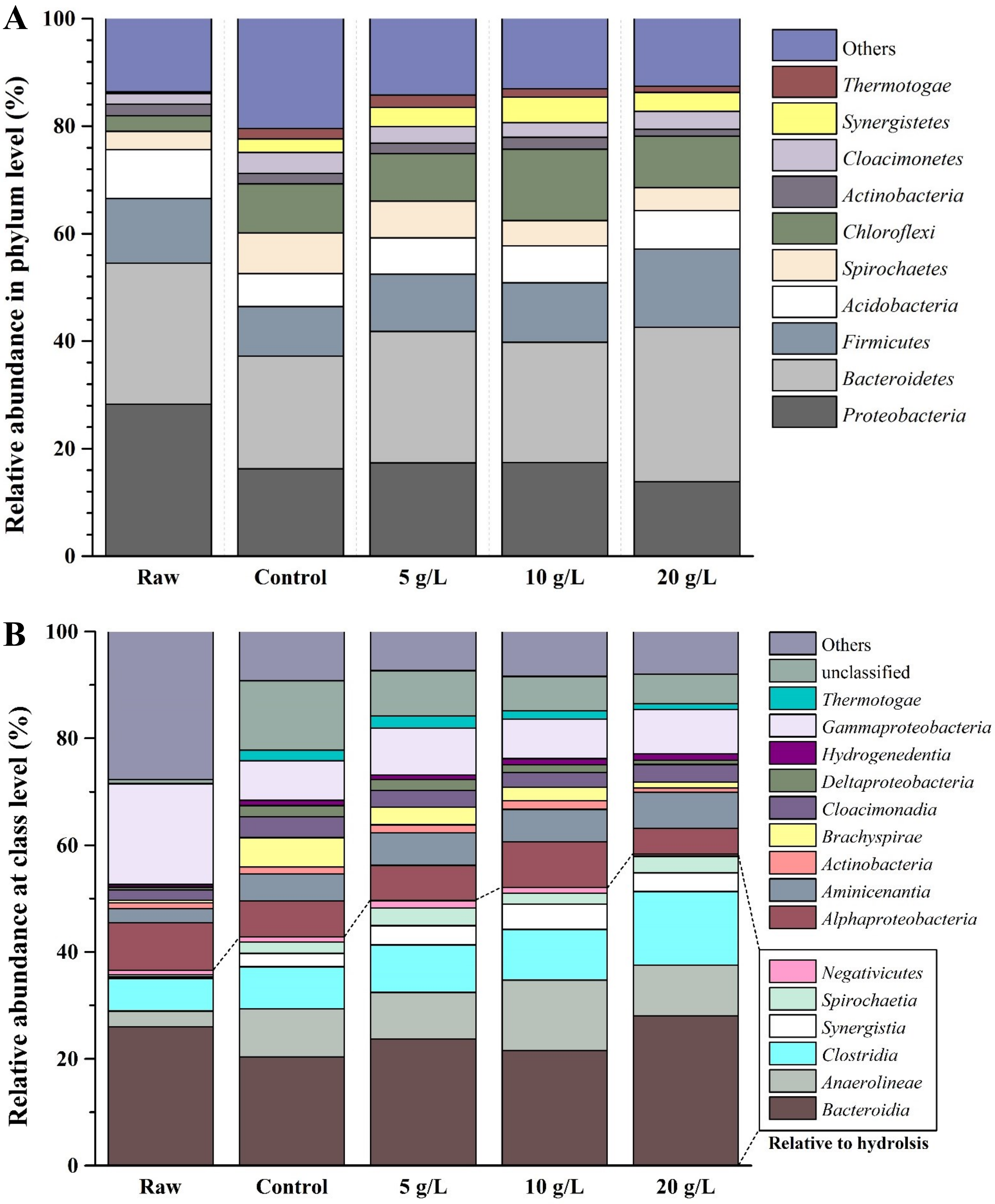

Fig. 4-5 The relative abundance of bacterial community at phylum (A) and class (B) levels in the sludge samples.

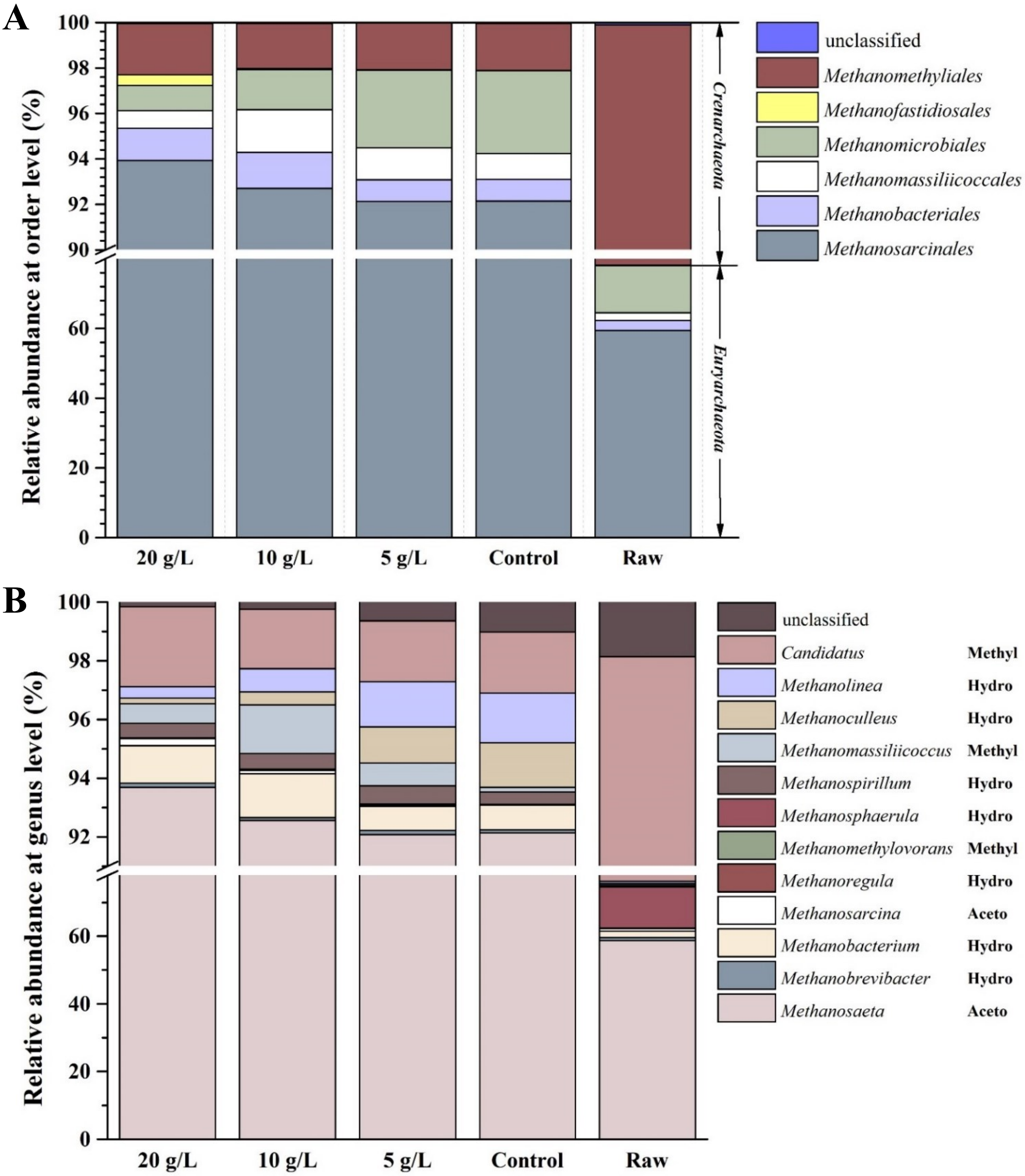

Fig. 4-6 The relative abundance of archaeal community at order (A) and genus (B) levels in the sludge samples. Abbreviations: Aceto = Acetotrophic; Methyl = Methylotrophic; Hydro = Hydrogenotrophic.

Chapter 5 Conclusions and future research

5.1 Conclusions

This study verified the feasibility of CTS-Fe used for simultaneous P removal/recovery and enhanced methane production from AD of WAS, and provided theoretical support for the application of CTS-Fe in practical AD systems. The main conclusions can be summarized as follows:

(1) CTS-Fe had better adsorption capacity in a wide pH range. Kinetic, isotherm, and thermodynamic studies demonstrated that the phosphate adsorption process was spontaneous and endothermic. FTIR and XPS analysis indicated that the main mechanisms involved in adsorption are ligand exchange and electrostatic attraction processes.

(2) CTS-Fe addition could significantly improve the AD of WAS, achieving increased methane production by 8.0% - 21.1%, and increased VS reduction rate by 110% - 120% in the CTS-Fe added digester compared with the control.

(3) P could be successfully recovered as vivianite from WAS with CTS-Fe addition. Characterization analysis demonstrated that ligand exchange and chemical precipitation are the dominant mechanisms for P removal/recovery from WAS. 95% of P can be removed/recovered from liquid digestate in the CTS-Fe added AD reactor.

(4) CTS-Fe enhanced the reduction of Fe (III)-P compounds in the sludge with phosphate released into the liquid phase. P fractionation results indicate that 2.4 times higher NAIP reduction occurred in the solid phase of sludge at 20 g/L of CTS-Fe (6.72 mg/g-SS) when compared to the control (2.77 mg/g-SS).

(5) The analysis of microbial community confirmed that CTS-Fe had the ability to stimulate the hydrolysis process through the DIR process, providing abundant substrates for methanogens, thereby enhanced methane production.

5.2 Future research

To make full use of CTS-Fe composite during AD system, future research should be followed up in several aspects: (1) to explore the effect of CTS-Fe composite on the P recovery and methane generation during the thermophilic AD; (2) to explore the feasibility of P recovery and enhanced methanogenesis in AD with CTS-Fe after regeneration; and (3) to explore the effective methods to extract P from P-loaded CTS-Fe.

References

Amer, M.W., Awwad, A.M. 2018. Removal of As(V) from aqueous solution by adsorption onto nanocrystalline kaolinite: Equilibrium and thermodynamic aspects of adsorption. Environ. Nanotechnol. Monit. Manag. 9, 37-41.

APHA, 2012. Standard Methods for the Examination of Water and Wastewater. 22nd ed. American Public Health Association/American Water Work Association/Water Environment Federation, Washington D.C., USA.

Bae, S., Sihn, Y., Kyung, D., Yoon, S., Eom, T., Kaplan, U., Kim, H., Schäfer, T., Han, S., Lee, W. 2018. Molecular identification of Cr (VI) removal mechanism on vivianite surface. Environ. Sci. Technol. 52(18), 10647-10656.

Baek, G., Kim, J., Cho, K., Bae, H., Lee, C. 2015. The biostimulation of anaerobic digestion with (semi) conductive ferric oxides: their potential for enhanced biomethanation. Appl. Microbiol. Biotechnol. 99(23), 10355-10366.

Baek, G., Kim, J., Lee, C. 2014. Influence of ferric oxyhydroxide addition on biomethanation of waste activated sludge in a continuous reactor. Bioresour. Technol. 166, 596-601.

Barbosa, H.F., Attjioui, M., Leitão, A., Moerschbacher, B.M., Cavalheiro, É.T. 2019. Characterization, solubility and biological activity of amphihilic biopolymeric Schiff bases synthesized using chitosans. Carbohydr. Polym. 220, 1-11.

Barret, M., Gagnon, N., Kalmokoff, M.L., Topp, E., Verastegui, Y., Brooks, S.P., Matias, F., Neufeld, J.D., Talbot, G. 2013. Identification of Methanoculleus spp. as active methanogens during anoxic incubations of swine manure storage tank samples. Appl. Environ. Microbiol. 79(2), 424-433.

Ben Ghorbal, G., Tricoteaux, A., Thuault, A., Louis, G., Chicot, D. 2017. Comparison of conventional Knoop and Vickers hardness of ceramic materials. J. Eur. Ceram. Soc. 37(6), 2531-2535.

Blöcher, C., Niewersch, C., Melin, T. 2012. Phosphorus recovery from sewage sludge with a hybrid process of low pressure wet oxidation and nanofiltration. Water Res. 46(6), 2009-2019.

Bottini, A., Rizzo, L. 2012. Phosphorus recovery from urban wastewater treatment plant sludge liquor by ion exchange. Sep. Sci. Technol. 47(4), 613-620.

Bozorgpour, F., Ramandi, H.F., Jafari, P., Samadi, S., Yazd, S.S., Aliabadi, M. 2016. Removal of nitrate and phosphate using chitosan/Al_2O_3/Fe_3O_4 composite nanofibrous adsorbent: Comparison with chitosan/Al_2O_3/Fe_3O_4 beads. Int. J. Biol. Macromol. 93(Pt A), 557-

565.

Browne, P., Tamaki, H., Kyrpides, N., Woyke, T., Goodwin, L., Imachi, H., Bräuer, S., Yavitt, J.B., Liu, W.-T., Zinder, S. 2017. Genomic composition and dynamics among Methanomicrobiales predict adaptation to contrasting environments. ISME J. 11(1), 87-99.

Cadillo-Quiroz, H., Yavitt, J.B., Zinder, S.H. 2009. Methanosphaerula palustris gen. nov., sp. nov., a hydrogenotrophic methanogen isolated from a minerotrophic fen peatland. Int. J. Syst. Evol. Microbiol. 59(5), 928-935.

Cao, J., Wu, Y., Zhao, J., Jin, S., Aleem, M., Zhang, Q., Fang, F., Xue, Z., Luo, J. 2019. Phosphorus recovery as vivianite from waste activated sludge via optimizing iron source and pH value during anaerobic fermentation. Bioresour. Technol. 293, 122088.

Campbell, H. W. 2000. Sludge management–future issues and trends. Water Sci. Technol. 41(8), 1-8.

Chatterjee, S., Woo, S.H. 2009. The removal of nitrate from aqueous solutions by chitosan hydrogel beads. J. Hazard. Mater. 164(2), 1012-1018.

Chen, Y., Lin, H., Shen, N., Yan, W., Wang, J., Wang, G. 2019. Phosphorus release and recovery from Fe-enhanced primary sedimentation sludge via alkaline fermentation. Bioresour. Technol. 278, 266-271.

Cheng, X., Chen, B., Cui, Y., Sun, D., Wang, X. 2015. Iron (III) reduction-induced phosphate precipitation during anaerobic digestion of waste activated sludge. Sep. Purif. Technol. 143, 6-11.

Cheng, X., Wang, J., Chen, B., Wang, Y., Liu, J., Liu, L. 2017. Effectiveness of phosphate removal during anaerobic digestion of waste activated sludge by dosing iron (III). J. Environ. Manage. 193, 32-39.

Chitrakar, R., Tezuka, S., Sonoda, A., Sakane, K., Ooi, K., Hirotsu, T. 2006. Selective adsorption of phosphate from seawater and wastewater by amorphous zirconium hydroxide. J. Colloid Interface Sci. 297(2), 426-433.

Cordell, D., Drangert, J.-O., White, S. 2009. The story of phosphorus: global food security and food for thought. Glob. Environ. Change. 19(2), 292-305.

Cornell, R.M., Schwertmann, U. 2003. The iron oxides: structure, properties, reactions, occurrences and uses. John Wiley & Sons.

Cruz Viggi, C., Rossetti, S., Fazi, S., Paiano, P., Majone, M., Aulenta, F. 2014. Magnetite particles triggering a faster and more robust syntrophic pathway of methanogenic propionate degradation. Environ. Sci. Technol. 48(13), 7536-7543.

Cui, G., Liu, M., Chen, Y., Zhang, W., Zhao, J. 2016. Synthesis of a ferric hydroxide-coated cellulose nanofiber hybrid for effective removal of phosphate from wastewater. Carbohydr. Polym. 154, 40-47.

Dantas, T.N.D.C., Neto, A.A.D., Moura, M.C.P.D.A., Neto, E.L.B., Telemaco, E.D.P. 2001. Chromium Adsorption by Chitosan Impregnated with Microemulsion. Langmuir, 17(14), 4256-4260.

de Godoi, F.C., Rodriguez-Castellon, E., Guibal, E., Beppu, M.M. 2013. An XPS study of chromate and vanadate sorption mechanism by chitosan membrane containing copper nanoparticles. Chem. Eng. J. 234, 423-429.

Demarchi, C.A., Campos, M., Rodrigues, C.A. 2013. Adsorption of textile dye Reactive Red 120 by the chitosan–Fe (III)-crosslinked: Batch and fixed-bed studies. J. Environ. Chem. Eng. 1(4), 1350-1358.

Deng, H., Chen, Y., Cao, Y., Chen, W. 2016. Enhanced phosphate and fluoride removal from aqueous solution by ferric-modified chromium (III)-fibrous protein. J. Taiwan Inst. Chem. Eng. 68, 323-331.

Deublein, D., Steinhauser, A. 2011. Biogas from waste and renewable resources: an introduction. John Wiley & Sons.

Ding, D., Zhao, Y., Yang, S., Shi, W., Zhang, Z., Lei, Z., Yang, Y. 2013. Adsorption of cesium from aqueous solution using agricultural residue--walnut shell: equilibrium, kinetic and thermodynamic modeling studies. Water Res. 47(7), 2563.

Dong, B., Xia, Z., Sun, J., Dai, X., Chen, X., Ni, B.J. 2019. The inhibitory impacts of nano-graphene oxide on methane production from waste activated sludge in anaerobic digestion. Sci. Total Environ. 646, 1376-1384.

dos Santos, H.H., Demarchi, C.A., Rodrigues, C.A., Greneche, J.M., Nedelko, N., Ślawska-Waniewska, A. 2011. Adsorption of As(III) on chitosan-Fe-crosslinked complex (Ch-Fe). Chemosphere, 82(2), 278-283.

Egle, L., Rechberger, H., Krampe, J., Zessner, M. 2016. Phosphorus recovery from municipal wastewater: An integrated comparative technological, environmental and economic assessment of P recovery technologies. Sci. Total Environ. 571, 522-542.

Fagundes, T., Bernardi, E.L., Rodrigues, C.A. 2001. Phosphate adsorption on chitosan-FeIII-crosslinking: Batch and column studies. J. Liq. Chromatogr. Relat. Technol. 24(8), 1189-1198.

Feng, B., Peng, J., Guo, W., Zhang, W., Ai, G., Wang, H. 2017. The effect of changes in pH on the depression of talc by chitosan and the associated mechanisms. Powder Technol. 325.

Filipkowska, U., Jóźwiak, T., Szymczyk, P. 2014. Application of cross-linked chitosan for phosphate removal from aqueous solutions. Prog. Chem. Appl. Chitin Deriv. XIX(1), 5-14.

Fonts, I., Azuara, M., Gea, G., Murillo, M. 2009. Study of the pyrolysis liquids obtained from different sewage sludge. J. Anal. Appl. Pyrolysis. 85(1-2), 184-191.

García-Albacete, M., Martín, A., Cartagena, M.C. 2012. Fractionation of phosphorus biowastes: characterisation and environmental risk. Waste Manage. 32(6), 1061-1068.

Giusti, L. 2009. A review of waste management practices and their impact on human health. Waste Manage. 29(8), 2227-2239.

Hamdi, N., Srasra, E. 2012. Removal of phosphate ions from aqueous solution using Tunisian clays minerals and synthetic zeolite. Journal of Environmental Sciences, 24(4), 617-623.

Hao, X., Wang, C., van Loosdrecht, M.C., Hu, Y. 2013. Looking beyond struvite for P-recovery, J. Am. Chem. Soc.

Hao, X., Wei, J., van Loosdrecht, M.C., Cao, D. 2017. Analysing the mechanisms of sludge digestion enhanced by iron. Water Res. 117, 58-67.

Hataf, N., Ghadir, P., Ranjbar, N. 2018. Investigation of soil stabilization using chitosan biopolymer. J. Clean. Prod. 170, 1493-1500.

He, Y., Lin, H., Dong, Y., Wang, L. 2017. Preferable adsorption of phosphate using lanthanum-incorporated porous zeolite: Characteristics and mechanism. Appl. Surf. Sci., 426.

He, Z.W., Liu, W.-Z., Wang, L., Tang, C.C., Guo, Z.C., Yang, C.X., Wang, A.J. 2016. Clarification of phosphorus fractions and phosphorus release enhancement mechanism related to pH during waste activated sludge treatment. Bioresour. Technol., 222, 217-225.

Hu, Q., Chen, N., Feng, C., Hu, W. 2015. Nitrate adsorption from aqueous solution using granular chitosan-Fe^{3+} complex. Appl. Surf. Sci., 347, 1-9.

Huang, R., Tang, Y. 2015. Speciation dynamics of phosphorus during (hydro) thermal treatments of sewage sludge. Environ. Sci. Technol. 49(24), 14466-14474.

Hui, B., Zhang, Y., Ye, L. 2014. Preparation of PVA hydrogel beads and adsorption mechanism for advanced phosphate removal. Chem. Eng. J. 235, 207-214.

Imachi, H., Sakai, S., Sekiguchi, Y., Hanada, S., Kamagata, Y., Ohashi, A., Harada, H. 2008. Methanolinea tarda gen. nov., sp. nov., a methane-producing archaeon isolated from a methanogenic digester sludge. Int. J. Syst. Evol. Microbiol. 58(1), 294-301.

Jain, M., Garg, V.K., Kadirvelu, K. 2010. Adsorption of hexavalent chromium from aqueous medium onto carbonaceous adsorbents prepared from waste biomass. J. Environ.

Manage. 91(4), 949-957.

Jing, S.B., Yamaguchi, T. 2006. Removal of Phosphate from Dilute Phosphate Solution by an Iron Chitosan Complex to Be Used as an Oral Sorbent. Bull.chem.soc.jpn, 65(7), 1866-1870.

Joshi, P., Manocha, S. 2017. Kinetic and thermodynamic studies of the adsorption of copper ions on hydroxyapatite nanoparticles. Mater. Today. 4(9), 10455-10459.

Kato, S., Nakamura, R., Kai, F., Watanabe, K., Hashimoto, K. 2010. Respiratory interactions of soil bacteria with (semi) conductive iron oxide minerals. Environ. Microbiol. 12(12), 3114-3123.

Kemacheevakul, P., Polprasert, C., Shimizu, Y. 2011. Phosphorus recovery from human urine and anaerobically treated wastewater through pH adjustment and chemical precipitation. Environmental technology, 32(7), 693-698.

Kim, S.J., Park, S.J., Cha, I.T., Min, D., Kim, J.S., Chung, W.H., Chae, J.C., Jeon, C.O., Rhee, S.K. 2014. Metabolic versatility of toluene degrading, iron reducing bacteria in tidal flat sediment, characterized by stable isotope probing based metagenomic analysis. Environ. Microbiol. 16(1), 189-204.

Kizito, S., Luo, H., Wu, S., Ajmal, Z., Lv, T., Dong, R. 2017. Phosphate recovery from liquid fraction of anaerobic digestate using four slow pyrolyzed biochars: Dynamics of adsorption, desorption and regeneration. J. Environ. Manage. 201, 260-267.

Kumar, I.A., Viswanathan, N. 2017. Development of multivalent metal ions imprinted chitosan biocomposites for phosphate sorption. Int. J. Biol. Macromol. 104, 1539-1547.

Lai, L., Xie, Q., Chi, L., Gu, W., Wu, D. 2016. Adsorption of phosphate from water by easily separable Fe3O4@SiO2 core/shell magnetic nanoparticles functionalized with hydrous lanthanum oxide. J. Colloid Interface Sci. 465, 76-82.

Lay, J.-J., Lee, Y.-J., Noike, T. 1999. Feasibility of biological hydrogen production from organic fraction of municipal solid waste. Water Res. 33(11), 2579-2586.

Li, B., Huang, H.M., Boiarkina, I., Yu, W., Huang, Y.F., Wang, G.Q., Young, B.R. 2019a. Phosphorus recovery through struvite crystallisation: Recent developments in the understanding of operational factors. J. Environ. Manage. 248, 109254.

Li, G., Gao, S., Zhang, G., Zhang, X. 2014. Enhanced adsorption of phosphate from aqueous solution by nanostructured iron (III) - copper (II) binary oxides. Chem. Eng. J. 235, 124-131.

Li, L., He, J., Wang, M., Xin, X., Xu, J., Zhang, J. 2018. Efficient volatile fatty acids production from waste activated sludge after ferrate pretreatment with alkaline environment and the responding microbial community shift. ACS Sustain. Chem. Eng. 6(12), 16819-16827.

Li, L., Pang, H., He, J., Zhang, J. 2019b. Characterization of phosphorus species distribution in waste activated sludge after anaerobic digestion and chemical precipitation with Fe^{3+} and Mg^{2+}. Chem. Eng. J. 373, 1279-1285.

Li, L., Qu, Z., Jia, R., Wang, B., Wang, Y., Qu, D. 2017. Excessive input of phosphorus significantly affects microbial Fe (III) reduction in flooded paddy soils by changing the abundances and community structures of Clostridium and Geobacteraceae. Sci. Total Environ. 607, 982-991.

Li, W.-W., Zhang, H.-L., Sheng, G.-P., Yu, H.-Q. 2015a. Roles of extracellular polymeric substances in enhanced biological phosphorus removal process. Water Res. 86, 85-95.

Li, Y., Zhang, Y., Meng, X., Yu, Z., Quan, X. 2015b. Fe^0 enhanced acetification of propionate and granulation of sludge in acidogenic reactor. Appl. Microbiol. Biotechnol. 99(14), 6083-6089.

Lin, R., Cheng, J., Zhang, J., Zhou, J., Cen, K., Murphy, J.D. 2017a. Boosting biomethane yield and production rate with graphene: The potential of direct interspecies electron transfer in anaerobic digestion. Bioresour. Technol. 239, 345-352.

Lin, L., Li, R. H., Li, Y., Xu, J., Li, X. Y. 2017b. Recovery of organic carbon and phosphorus from wastewater by Fe-enhanced primary sedimentation and sludge fermentation. Process Biochem. 54, 135-139.

Liu, H., Sun, X., Yin, C., Hu, C. 2008. Removal of phosphate by mesoporous ZrO_2. J. Hazard. Mater. 151(2), 616-622.

Liu, Q., Xu, M., Li, F., Wu, T., Li, Y. 2016. Rapid and effective removal of Cr(VI) from aqueous solutions using the $FeCl_3/NaBH_4$ system. Chem. Eng. J. 296, 340-348.

Liu, W., Zhang, J., Zhang, C., Wang, Y., Li, Y. 2010. Adsorptive removal of Cr (VI) by Fe-modified activated carbon prepared from Trapa natans husk. Chem. Eng. J. 162(2), 677-684.

Liu, X., Zhang, L. 2015. Removal of phosphate anions using the modified chitosan beads: Adsorption kinetic, isotherm and mechanism studies. Powder Technol. 277, 112-119.

Liu, Y., Zhu, Y., Jia, H., Yong, X., Zhang, L., Zhou, J., Cao, Z., Kruse, A., Wei, P. 2017. Effects of different biofilm carriers on biogas production during anaerobic digestion of corn straw. Bioresour. Technol. 244, 445-451.

Lovley, D.R. 1991. Dissimilatory Fe (III) and Mn (IV) reduction. Microbiol. Mol. Biol. Rev. 55(2), 259-287.

Lovley, D.R., Klug, M.J. 1983. Sulfate reducers can outcompete methanogens at freshwater sulfate concentrations. Appl. Environ. Microbiol. 45(1), 187-192.

Lu, T., Zhang, J., Wei, Y., Shen, P. 2019. Effects of ferric oxide on the microbial community and functioning during anaerobic digestion of swine manure. Bioresour. Technol. 287, 121393.

Luo, J., Zhang, Q., Wu, L., Feng, Q., Fang, F., Xue, Z., Li, C., Cao, J. 2018. Improving anaerobic fermentation of waste activated sludge using iron activated persulfate treatment. Bioresour. Technol. 268, 68-76.

Lv, H., Zhao, H., Cao, T., Qian, L., Wang, Y., Zhao, G. 2015. Efficient degradation of high concentration azo-dye wastewater by heterogeneous Fenton process with iron-based metal-organic framework. J. Mol. Catal. A Chem. 400, 81-89.

Lyu, H., Tang, J., Huang, Y., Gai, L., Zeng, E.Y., Liber, K., Gong, Y. 2017. Removal of hexavalent chromium from aqueous solutions by a novel biochar supported nanoscale iron sulfide composite. Chem. Eng. J.

Magdy, Y.H., Altaher, H. 2018. Kinetic Analysis of the Adsorption of Dyes From High Strength Wastewater on Cement Kiln Dust. J. Environ. Chem. Eng.

Mahaninia, M.H., Wilson, L.D. 2015. Cross-linked chitosan beads for phosphate removal from aqueous solution. J. Appl. Polym. Sci. 133(5).

Mahaninia, M.H., Wilson, L.D. 2017. Phosphate uptake studies of cross-linked chitosan bead materials. J. Colloid Interface Sci. 485, 201-212.

Mamais, D., Pitt, P.A., Cheng, Y.W., Loiacono, J., Jenkins, D. 1994. Determination of ferric chloride dose to control struvite precipitation in anaerobic sludge digesters. Water Environ. Res. 66(7), 912-918.

Manap, N.R.A., Shamsudin, R., Maghpor, M.N., Hamid, M.A.A., Jalar, A. 2018. Adsorption isotherm and kinetic study of gas-solid system of formaldehyde on oil palm mesocarp biochar: Pyrolysis effect. J. Environ. Chem. Eng.

Meng, X., Zhang, Y., Li, Q., Quan, X. 2013. Adding Fe0 powder to enhance the anaerobic conversion of propionate to acetate. Biochem. Eng. J. 73, 80-85.

MLIT, 2019. (Ministry of land, infrastructure, transportation and tourism). https://www.mlit.go.jp/mizukokudo/sewerage/crd_sewerage_tk_000124.html.

MOE (Ministry of the Environment, Japan), 2020. http://www.env.go.jp/press/107628.html. (Accessed on 23 January 2020).

Monea, M.C., Löhr, D.K., Meyer, C., Preyl, V., Xiao, J., Steinmetz, H., Schönberger, H., Drenkova-Tuhtan, A. 2020. Comparing the leaching behavior of phosphorus, aluminum and iron from post-precipitated tertiary sludge and anaerobically digested sewage sludge aiming at phosphorus recovery. J. Clean. Prod. 247, 119129.

Nanta, P., Kasemwong, K., Skolpap, W. 2018. Isotherm and kinetic modeling on superparamagnetic nanoparticles adsorption of polysaccharide. J. Environ. Chem. Eng. 6(1), 794-802.

Ntohogian, S., Gavriliadou, V., Christodoulou, E., Nanaki, S., Lykidou, S., Naidis, P., Mischopoulou, L., Barmpalexis, P., Nikolaidis, N., Bikiaris, D. 2018. Chitosan nanoparticles with encapsulated natural and uf-purified annatto and saffron for the preparation of uv protective cosmetic emulsions. Molecules, 23(9), 2107.

O'Loughlin, E.J., Boyanov, M.I., Flynn, T.M., Gorski, C.A., Hofmann, S.M., McCormick, M.L., Scherer, M.M., Kemner, K.M. 2013. Effects of bound phosphate on the bioreduction of lepidocrocite (γ-FeOOH) and maghemite (γ-Fe_2O_3) and formation of secondary minerals. Environ. Sci. Technol. 47(16), 9157-9166.

Omran, M., Fabritius, T., Elmahdy, A.M., Abdel-Khalek, N.A., El-Aref, M., Elmanawi, A.E.-H. 2015. XPS and FTIR spectroscopic study on microwave treated high phosphorus iron ore. Appl. Surf. Sci. 345, 127-140.

Orhon, D., Artan, N. 1994. Modelling of Activated Sludge Systems, Technologic Publ. Co., Lancester, USA.

Pastor, L., Mangin, D., Ferrer, J., Seco, A. 2010. Struvite formation from the supernatants of an anaerobic digestion pilot plant. Bioresour. Technol. 101(1), 118-125.

Peng, H., Zhang, Y., Tan, D., Zhao, Z., Zhao, H., Quan, X. 2018. Roles of magnetite and granular activated carbon in improvement of anaerobic sludge digestion. Bioresour. Technol. 249, 666-672.

Prot, T., Nguyen, V., Wilfert, P., Dugulan, A., Goubitz, K., De Ridder, D., Korving, L., Rem, P., Bouderbala, A., Witkamp, G.J. 2019. Magnetic separation and characterization of vivianite from digested sewage sludge. Sep. Purif. Technol., 224, 564-579.

Qu, J., Hu, Q., Shen, K., Zhang, K., Li, Y., Li, H., Zhang, Q., Wang, J., Quan, W. 2011. The preparation and characterization of chitosan rods modified with Fe^{3+} by a chelation mechanism. Carbohydr. Res. 346(6), 822-827.

Rahaman, M.S., Mavinic, D.S., Meikleham, A., Ellis, N. 2014. Modeling phosphorus removal and recovery from anaerobic digester supernatant through struvite crystallization in a fluidized bed reactor. Water Res. 51, 1-10.

Rajeswari, A., Amalraj, A., Pius, A. 2015. Removal of phosphate using chitosan-polymer composites. J. Environ. Chem. Eng. 3(4, Part A), 2331-2341.

Ren, Y., Wei, X., Zhang, M. 2008. Adsorption character for removal Cu(II) by magnetic Cu(II) ion imprinted composite adsorbent. J. Hazard. Mater. 158(1), 14-22.

Reynolds, P., Colleran, E. 1987. Evaluation and improvement of methods for coenzyme F_{420} analysis in anaerobic sludges. J. Microbiol. Methods. 7(2-3), 115-130.

Rotaru, A.-E., Shrestha, P.M., Liu, F., Markovaite, B., Chen, S., Nevin, K.P., Lovley, D.R. 2014. Direct interspecies electron transfer between Geobacter metallireducens and Methanosarcina barkeri. Appl. Environ. Microbiol. 80(15), 4599-4605.

Rothe, M., Kleeberg, A., Hupfer, M. 2016. The occurrence, identification and environmental relevance of vivianite in waterlogged soils and aquatic sediments. Earth Sci. Rev. 158, 51-64.

Rulkens, W., Bien, J. 2004. Recovery of energy from sludge–comparison of the various options. Water Sci. Technol. 50(9), 213-221.

Schneider, J.-M., Bigerelle, M., Iost, A. 1999. Statistical analysis of the Vickers hardness. Mater. Sci. Eng. A. 262(1), 256-263.

Shaw, S., Alla, S., Meena, S., Mandal, R., Prasad, N. 2017. Stabilization of temperature during magnetic hyperthermia by Ce substituted magnetite nanoparticles. J. Magn. Magn. Mater. 434, 181-186.

Shen, C., Shen, Y., Wen, Y., Wang, H., Liu, W. 2011. Fast and highly efficient removal of dyes under alkaline conditions using magnetic chitosan-Fe (III) hydrogel. Water Res. 45(16), 5200-5210.

Sowmya, A., Meenakshi, S. 2014. Effective removal of nitrate and phosphate anions from aqueous solutions using functionalised chitosan beads. Desalination Water Treat. 52(13-15), 2583-2593.

Spinelli, V.A., Laranjeira, M.C.M., Fávere, V.T. 2004. Preparation and characterization of quaternary chitosan salt: adsorption equilibrium of chromium(VI) ion. React Funct. Polym. 61(3), 347-352.

Tan, J., Wang, J., Xue, J., Liu, S.-Y., Peng, S.-C., Ma, D., Chen, T.-H., Yue, Z. 2015. Methane production and microbial community analysis in the goethite facilitated anaerobic reactors using algal biomass. Fuel, 145, 196-201.

Tan, R., Miyanaga, K., Toyama, K., Uy, D., Tanji, Y. 2010. Changes in composition and microbial communities in excess sludge after heat-alkaline treatment and acclimation. Biochem. Eng. J. 52(2-3), 151-159.

Tofik, A., Taddesse, A.M., Tesfahun, K., Girma, G. 2016. Fe–Al binary oxide nanosorbent: synthesis, characterization and phosphate sorption property. J. Environ. Chem. Eng.

4(2), 2458-2468.

Tyagi, V.K., Lo, S.-L. 2013. Sludge: a waste or renewable source for energy and resources recovery? Renew. Sust. Energ. Rev. 25, 708-728.

Vanwonterghem, I., Evans, P.N., Parks, D.H., Jensen, P.D., Woodcroft, B.J., Hugenholtz, P., Tyson, G.W. 2016. Methylotrophic methanogenesis discovered in the archaeal phylum Verstraetearchaeota. Nat. Microbiol. 1(12), 1-9.

Vázquez, I., Rodríguez-Iglesias, J., Marañón, E., Castrillón, L., Álvarez, M. 2007. Removal of residual phenols from coke wastewater by adsorption. J. Hazard. Mater. 147(1), 395-400.

Wan, D., Liu, H., Liu, R., Qu, J., Li, S., Zhang, J. 2012. Adsorption of nitrate and nitrite from aqueous solution onto calcined (Mg–Al) hydrotalcite of different Mg/Al ratio. Chem. Eng. J. 195-196, 241-247.

Wang, D., Duan, Y., Yang, Q., Liu, Y., Ni, B.J., Wang, Q., Zeng, G., Li, X., Yuan, Z. 2018a. Free ammonia enhances dark fermentative hydrogen production from waste activated sludge. Water Res. 133, 272-281.

Wang, G., Li, Q., Gao, X., Wang, X.C. 2018b. Synergetic promotion of syntrophic methane production from anaerobic digestion of complex organic wastes by biochar: performance and associated mechanisms. Bioresour. Technol. 250, 812–820.

Wang, M., Zhao, Z., Niu, J., Zhang, Y. 2018c. Potential of crystalline and amorphous ferric oxides for biostimulation of anaerobic digestion. ACS Sustain. Chem. Eng. 7(1), 697-708.

Wang, R., Wilfert, P., Dugulan, I., Goubitz, K., Korving, L., Witkamp, G.-J., van Loosdrecht, M.C. 2019. Fe (III) reduction and vivianite formation in activated sludge. Sep. Purif. Technol. 220, 126-135.

Weber, W.J., Morris, J.C. 1964. Adsorption in Heterogeneous Aqueous Systems. Journal, 56(4), 447-456.

Wilfert, P., Dugulan, A., Goubitz, K., Korving, L., Witkamp, G., Van Loosdrecht, M. 2018. Vivianite as the main phosphate mineral in digested sewage sludge and its role for phosphate recovery. Water Res. 144, 312-321.

Wong, P.Y., Cheng, K.Y., Kaksonen, A.H., Sutton, D.C., Ginige, M.P. 2013. A novel post denitrification configuration for phosphorus recovery using polyphosphate accumulating organisms. Water Res. 47(17), 6488-6495.

Wu, F.-C., Tseng, R.-L., Juang, R.-S. 2009. Characteristics of Elovich equation used for the analysis of adsorption kinetics in dye-chitosan systems. Chem. Eng. J. 150(2), 366-373.

Wu, Y., Luo, J., Zhang, Q., Aleem, M., Fang, F., Xue, Z., Cao, J. 2019. Potentials and challenges of phosphorus recovery as vivianite from wastewater: A review. Chemosphere.

Xia, Y., Wang, Y., Wang, Y., Chin, F.Y., Zhang, T. 2016. Cellular adhesiveness and cellulolytic capacity in Anaerolineae revealed by omics-based genome interpretation. Biotechnol. Biofuels. 9(1), 1-13.

Xie, J., Li, C., Chi, L., Wu, D. 2013. Chitosan modified zeolite as a versatile adsorbent for the removal of different pollutants from water. Fuel, 103, 480-485.

Xie, Y., Yi, Y., Qin, Y., Wang, L., Liu, G., Wu, Y., Diao, Z., Zhou, T., Xu, M. 2016. Perchlorate degradation in aqueous solution using chitosan-stabilized zero-valent iron nanoparticles. Sep. Purif. Technol. 171, 164-173.

Xu, K., Liu, H., Chen, J. 2010. Effect of classic methanogenic inhibitors on the quantity and diversity of archaeal community and the reductive homoacetogenic activity during the process of anaerobic sludge digestion. Bioresour. Technol. 101(8), 2600-2607.

Xu, Y., Hu, H., Liu, J., Luo, J., Qian, G., Wang, A. 2015. pH dependent phosphorus release from waste activated sludge: contributions of phosphorus speciation. Chem. Eng. J. 267, 260-265.

Yang, H., Liu, J., Hu, P., Zou, L., Li, Y.-Y. 2019. Carbon source and phosphorus recovery from iron-enhanced primary sludge via anaerobic fermentation and sulfate reduction: Performance and future application. Bioresour. Technol. 294, 122174.

Yang, Y., Zhang, Y., Li, Z., Zhao, Z., Quan, X., Zhao, Z. 2017. Adding granular activated carbon into anaerobic sludge digestion to promote methane production and sludge decomposition. J. Clean. Prod. 149, 1101-1108.

Yashiro, Y., Sakai, S., Ehara, M., Miyazaki, M., Yamaguchi, T., Imachi, H. 2011. Methanoregula formicica sp. nov., a methane-producing archaeon isolated from methanogenic sludge. Int. J. Syst. Evol. Microbiol. 61(1), 53-59.

Yoon, S.-Y., Lee, C.-G., Park, J.-A., Kim, J.-H., Kim, S.-B., Lee, S.-H., Choi, J.-W. 2014. Kinetic, equilibrium and thermodynamic studies for phosphate adsorption to magnetic iron oxide nanoparticles. Chem. Eng. J. 236, 341-347.

Yu, Y., Lei, Z., Yuan, T., Jiang, Y., Chen, N., Feng, C., Shimizu, k., Zhang, Z. 2017. Simultaneous phosphorus and nitrogen recovery from anaerobically digested sludge using a hybrid system coupling hydrothermal pretreatment with MAP precipitation. Bioresour. Technol. 243, 634-640.

Yuan, T., Huang, W., Lei, Z., Zhao, Z., Zhang, Z. 2017. Effects of different alkalis on hydrolysis of swine manure during dry anaerobic digestion and resultant nutrients availability. Int.

Biodeterior. Biodegradation. 123, 138-145.

Zhang, D.-m., Chen, Y.-x., Jilani, G., Wu, W.-x., Liu, W.-l., Han, Z.-y. 2012. Optimization of struvite crystallization protocol for pretreating the swine wastewater and its impact on subsequent anaerobic biodegradation of pollutants. Bioresour. Technol., 116, 386-395.

Zhang, G., Liu, H., Liu, R., Qu, J. 2009a. Removal of phosphate from water by a Fe–Mn binary oxide adsorbent. J. Colloid Interface Sci. 335(2), 168-174.

Zhang, J., Chen, N., Tang, Z., Yu, Y., Hu, Q., Feng, C. 2015. A study of the mechanism of fluoride adsorption from aqueous solutions onto Fe-impregnated chitosan. Phys. Chem. Chem. Phys. 17(18), 12041.

Zhang, L., Keller, J., Yuan, Z. 2009b. Inhibition of sulfate-reducing and methanogenic activities of anaerobic sewer biofilms by ferric iron dosing. Water Res. 43(17), 4123-4132.

Zhang, Y., Feng, Y., Yu, Q., Xu, Z., Quan, X. 2014. Enhanced high-solids anaerobic digestion of waste activated sludge by the addition of scrap iron. Bioresour. Technol., 159, 297-304.

Zhao, J., Gui, L., Wang, Q., Liu, Y., Wang, D., Ni, B.-J., Li, X., Xu, R., Zeng, G., Yang, Q. 2017a. Aged refuse enhances anaerobic digestion of waste activated sludge. Water Res. 123, 724-733.

Zhao, Z., Li, Y., Quan, X., Zhang, Y. 2017b. Towards engineering application: Potential mechanism for enhancing anaerobic digestion of complex organic waste with different types of conductive materials. Water Res. 115, 266-277.

Zhao, Z., Li, Y., Quan, X., Zhang, Y. 2018a. Improving the co-digestion performance of waste activated sludge and wheat straw through ratio optimization and ferroferric oxide supplementation. Bioresour. Technol. 267, 591-598.

Zhao, Z., Zhang, Y., Li, Y., Dang, Y., Zhu, T., Quan, X., 2017c. Potentially shifting from interspecies hydrogen transfer to direct interspecies electron transfer for syntrophic metabolism to resist acidic impact with conductive carbon cloth. Chem. Eng. J. 313, 10–18.

Zhao, Z., Zhang, Y., Li, Y., Quan, X., Zhao, Z. 2018b. Comparing the mechanisms of ZVI and Fe_3O_4 for promoting waste-activated sludge digestion. Water Res. 144, 126-133.

Zhao, Z., Zhang, Y., Quan, X., Zhao, H. 2016. Evaluation on direct interspecies electron transfer in anaerobic sludge digestion of microbial electrolysis cell. Bioresour. Technol. 200, 235-244.

Zhou, K., Wu, B., Su, L., Xin, W., Chai, X. 2018. Enhanced phosphate removal using nanostructured hydrated ferric-zirconium binary oxide confined in a polymeric anion exchanger. Chem. Eng. J.

Zhuang, L., Tang, J., Wang, Y., Hu, M., Zhou, S. 2015. Conductive iron oxide minerals accelerate syntrophic cooperation in methanogenic benzoate degradation. J. Hazard. Mater. 293, 37-45.

Ziganshin, A.M., Ziganshina, E.E., Kleinsteuber, S., Nikolausz, M. 2016. Comparative analysis of methanogenic communities in different laboratory-scale anaerobic digesters. Archaea, 2016.

Acknowledgements

First of all I would like to say thank you from the bottom of my heart to my supervisors, dear Professor Zhengya Zhang for giving me the opportunity to study for a doctoral degree in Japan. I would like to thank him for the instructive advice, inspiring guidance and encouragement he has provided throughout my research. Also, my most sincere gratefulness should be given to Professor Zhongfang Lei, who cared so much about my research. I have benefited a lot from her erudition, patience, work attitude, dedication and meticulous instruction.

Specially, I would like to express my gratitude to Professor Chuanping Feng and Professor Nan Chen (China University of Geosciences (Beijing)), for their provided great help for the improvement of my dissertation and future study.

Secondly, special thanks should go to my thesis committee members, Professor Zhengya Zhang, Professor Zhongfang Lei, Professor Shimizu Kazuya and Professor Helmut Yabar for their patient reading and listening, valuable and useful comments on my thesis.

Thirdly, I want to say thank you to all the members of our laboratory. Thanks for your help in the colorful years when we study and work together. Whenever, I have a question, we can communicate together.

Finally, I would like to express my gratitude to my parents. They are always standing by me to give support and make me feel strong.

Achievements

[1] **Zhang, B.**, Chen, N., Feng, C., Zhang, Z. (2018). Adsorption for phosphate by crosslinked/non-crosslinked-chitosan-Fe (III) complex sorbents: characteristic and mechanism. Chem. Eng. J. 353, 361-372 (IF=10.652).

[2] **Zhang, B.**, Zhao, Z., Chen, N., Feng, C., Lei, Z., Zhang, Z. (2020). Insight into efficient phosphorus removal/recovery from enhanced methane production of waste activated sludge with chitosan-Fe supplementation. Water Res. 187, 116427 (IF=9.130).